IMAGING THROUGH SCATTERING MEDIA VIA TIME-DOMAIN INFORMATION ENCODING AND DECODING

A Dissertation

by

XINGCHEN ZHAO

Submitted to the Graduate and Professional School of
Texas A&M University
in partial fulfillment of the requirements for the degree of

DOCTOR OF PHILOSOPHY

Chair of Committee,	Marlan O. Scully
Committee Members,	Alexei Sokolov
	Aleksei Zheltikov
	Phillip Hemmer
Head of Department,	Grigory Rogachev

December 2021

Major Subject: Physics

ABSTRACT

Optical imaging through scattering media is a long-standing challenge with important applications ranging from observations through the turbulent atmosphere to imaging inside living tissues. Low-order aberrations due to random fluctuations of refractive index can be overcome by adaptive optics and turbulence-free ghost imaging; while the problem becomes intractable for optically opaque media in which strong light scattering scrambles the spatial information conveyed by light fields. Inspired by the heterodyne detection of the beat signal of two lasers, we propose a computational imaging scheme based on time-domain information encoding and fast-Fourier-transform-based information decoding that can realize non-invasive imaging through scattering media. The feasibility of the original idea is tested by a preliminary experiment that realizes imaging through scattering media by extracting the beat frequency of two lasers. The technique is further improved by replacing the beat signal of two lasers with an intensity-modulated laser. Using cross-spectrum detection of the modulation frequency and raster-scan measurement, we demonstrate that the image of an object can be reconstructed not only through both static and dynamic diffusers but also under extremely noisy environments, i.e., the light intensity is much lower than detector noise. To overcome the speed limit due to raster scan, the computational imaging mechanism is further improved to realize full-field imaging via space-time encoded pattern (STEP) illumination. We show that the images of objects can be reconstructed from a 1D time series of light intensity measured by a single-pixel photodetector. As a proof of concept, we experimentally demonstrate our technique with ground glass diffusers and slices of chicken breast as the scattering media. Various aspects of this technique, including resolution, penetration depth, imaging speed, and algorithm complexity, are discussed.

DEDICATION

To my wife Huaqing Wang and my son Caden W. Zhao.

ACKNOWLEDGMENTS

I hereby thank my family, my advisor, and my colleagues for their support and help during my Ph.D. study.

I sincerely thank my advisor Marlan O. Scully for his kind support of my study and research in the field of experimental quantum optics. I also would like to thank my committee members: Alexei Sokolov, Aleksei Zheltikov, and Phillip Hemmer for their guidance of my research. I also learned a lot and get much help from my colleagues: Zhenhuan Yi, Tao Peng, Yujie Shen, Fu Li, Zehua Han, M. Suhail Zubairy, Narangerel Altangerel, Barnabas Kim, and Navid Rajil. Thanks also go to my friends and the faculty and staff at the Department of Physics and Astronomy for giving me a wonderful and rewarding time at Texas A&M University.

I would like to thank my wife Huaqing for her endless understanding and encouragement, and my son Caden for making my life so sweet.

CONTRIBUTORS AND FUNDING SOURCES

Contributors

This work was supervised by a dissertation committee consisting of Professor Marlan O. Scully, Alexei Sokolov and Aleksei Zheltikov of the Department of Physics and Astronomy and Professor Phillip Hemmer of the Department of Electrical & Computer Engineering.

All work for the dissertation was completed by the student, in collaboration with Tao Peng and Zhenhuan Yi of the Department of Physics and Astronomy.

Funding Sources

Graduate study was supported by Herman F. Heep and Minnie Belle Heep Texas A&M University Endowed Fund held/administered by the Texas A&M Foundation and Robert A. Welch Foundation Graduate Fellowship.

NOMENCLATURE

CW	Continuous-wave
GOI	Optical image intensifier
SHG	Second-harmonic generation
OCT	Optical coherence tomography
MFP	Mean free path
TMFP	Transport mean free path
CCD	Charge-coupled device
SNR	Signal-to-noise ratio
FFT	Fast Fourier transform
SLM	Spatial light modulator
OPC	Optical phase conjugation
DOPC	Digital optical phase conjugation
TM	Transmission matrix
$A * B$	Convolution of A and B
$A \star B$	Cross-correlation of A and B
DMD	Digital micromirror device
VBW	Video bandwidth
FWHM	Full width at half maximum
GGD	Ground glass diffuser
SD	Stationary diffuser
DD	Dynamic diffuser
STEP	Space-time encoded pattern

TABLE OF CONTENTS

Page

LIST OF FIGURES

LIST OF TABLES

TABLE Page

1. INTRODUCTION

As one may experience in a foggy morning, the visibility is reduced, making it hard to see an object that could be seen without fog. Optical imaging is a prime means of investigating the structure of matter in both microscopic and macroscopic scales, which benefits from a wide range of light-matter interactions. The propagation of light field in a classical imaging system immersed in a refractive-index homogeneous medium is well understood. The point-to-point mapping between the object plane and the image plane guarantees the formation of a clear image of the object. However, the classical imaging system fails to produce clear images when light propagates through inhomogeneous media, because the distortion of wavefront scrambles the original point-to-point relationship, resulting in a random pattern on the image plane (see Fig. 1.1).

Optical observation through inhomogeneous media remains one of the most challenging problems in optics since the nonuniform microstructure in the media degrades the resolution and the signal-to-noise ratio (SNR) of the observation [1, 2, 3, 4, 5, 6]. Optical turbulence is a result of spatial and temporal fluctuations of fluid properties such as index of refraction and velocity [7]. Turbulence can perturb the wavefront generated by every single point source and thus smear the classical optical image of an object, which is harmful to distant imaging and sensitive observation. The problem is addressed in a "turbulence-free" imaging scheme, in which second-order optical coherence is measured via two spatially separated photodetectors to produce the image of an object. The turbulence-free image can be obtained when the two different yet indistinguishable two-photon amplitudes overlap and experience almost the same turbulence. In this case, the phase variations due to turbulence cancel each other, making the observation immune to turbulence [7, 8].

The problem becomes intractable when light travels through highly disordered media, such as turbid fluids and biological tissues [2, 4, 6]. Such media are usually considered as optically opaque, in which the amplitudes of incident fields are dramatically attenuated, and the wave vectors are mixed up after passing through the media. The direction of photon propagation can even be randomized if the thickness of the medium and is larger than the transport mean free path (TMFP).

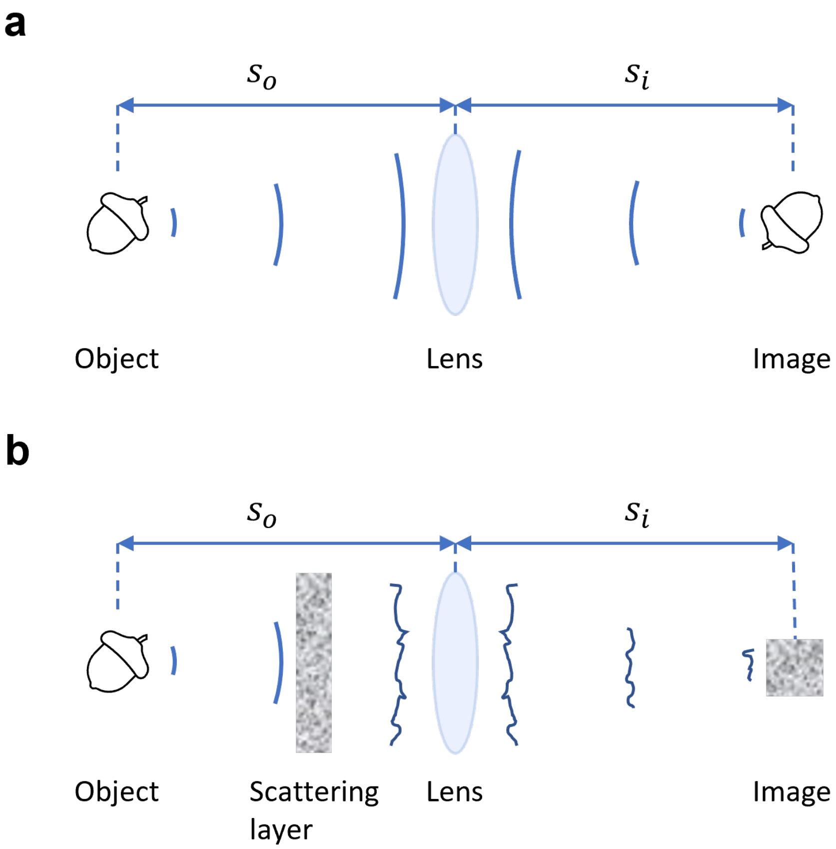

Figure 1.1: Schematic of an classical imaging system without/with scattering media. **a**. For a imaging system without scattering media, any radiation starting from a point on the object plane will impinge at a unique point on the image plane. The point-to-point relationship is a result of constructive–destructive interference. **b**. When a scattering medium blocks the direct view of the object, the field from any point source on the object is scattered. The scattering changes the propagation direction of the field and introduces random phases, which destroys the original point-to-point relationship. Therefore, the image becomes a random pattern.

As a result, the spatial information conveyed by light field is scrambled by strong light scattering, leading to the degradation of spatial resolution and reduction of imaging depth.

In this dissertation, I present an experiment that inspires a new idea to investigating the problem of imaging through scattering media and a number of experiments that implement the idea to realize the vision of looking through scattering media. In Chapter 2, some basic concepts of imaging and scattering media are introduced, and a general theoretical description of the optical imaging and scattering media is given. Chapter 3 presents the experimental results of high-order coherence functions and spectral distributions of the laser as well as a theoretical analysis based on the Scully-Lamb quantum theory of the laser. This experiment has inspired the later experiments on imaging through scattering media. In Chapter 4, we propose a theoretical model of imaging objects behind turbid media using an intensity-modulated continuous-wave (CW) laser and cross-spectrum detection. Non-invasive imaging through both stationary and dynamic ground glass diffusers is demonstrated experimentally with this method. In Chapter 5, a full-field imaging method using space-time encoded pattern (STEP) illumination patterns is proposed and non-invasive single-pixel imaging through ground glass diffusers and slices of chicken breast is demonstrated experimentally. For the remainder of this chapter, some of the current modalities of imaging through scattering media will be introduced.

1.1 Imaging modalities that reject scattered light

Over the past three decades, many innovative techniques to overcome this practical, yet fundamental, problem have been proposed. One approach is based on rejecting the scattered light fields and using only the unscattered components. The idea is implemented by a variety of modern techniques.

Spatial filtering is the most straightforward implementation which introduces some spatial light filters, such as pinholes and collimating grids, to a conventional imaging system [9, 10]. It exploits the fact that scattered light usually deviates from its initial propagation direction and are scattered to higher spatial frequencies. Unfortunately, the imaging depth of this technique is very shallow because of the exponential decay of ballistic photons, and the resolution is limited by the scattered photons of which the trajectories are parallel to the incident direction. Confocal imaging can greatly reduce the negative effects of scattered light by scanning image pixels sequentially [11, 12, 13]. However, it also suffers from a shallow imaging depth due to the scattering of incident light before focus. The imaging depth can be increased when a confocal system is combined with multi-photon microscopy, which measures the fluorescence signal of multi-photon absorption in fluorescent samples [14, 15, 16, 17]. In this case, sources with longer wavelengths are usually used as excitation radiation, which is less scattered in many media, and only fluorescence signal is collected.

Time-gating offers another way to extract the ballistic light based on its propagation time in transmission imaging systems, since ballistic photons always travel along the shortest path between light source and detector. The temporal discrimination to separate ballistic photons is usually faster than 1 ps. Such a detection speed has not been available in electronic detectors. As a consequence, incoherent time-gating techniques that employ streak cameras [18, 19, 20], fast photodiodes, and gated optical image intensifiers (GOIs) [21, 22] will inevitably collect snake photons and the resolution is reduced accordingly. On the other hand, the fast temporal discrimination can be achieved using some nonlinear optical correlation techniques, in which ultra-fast lasers are used, and the time gate has the same duration as the pulsed lasers. The general scheme has three steps: 1. splitting the incident laser pulse into probe and reference beam; 2. let the probe beam pass through the sample; 3. combining the two beams again in some nonlinear medium and measuring the expected nonlinear effects to retrieve ballistic signals. Nonlinear optical time-gating has been implemented with various nonlinear phenomena such as second-harmonic generation (SHG) [23, 24, 25], stimulated Raman scattering [26, 27], parametric amplification [28, 29, 30, 31], and optical Kerr effect [32, 33, 34, 35, 36], in which the ballistic signals are either sampled according to their relative delays in time, or amplified when they are temporally or spatially overlapped with the reference beam and trigger the nonlinear amplification mechanism. However, it should be noted that the requirement of using high-power lasers in nonlinear optical time-gating makes it unfriendly to biomedical samples. Furthermore, images are typically obtained in a raster-scan manner with long integration time for each step, so the image acquisition time is usually unreasonably long.

The discrimination between ballistic and scattered light can also be achieved by coherence-gated imaging techniques. Similar to time gating, a coherent source is split into a probe beam and a reference beam in coherence-gated techniques. The ballistic component in the probe beam can be identified since it remains coherence with the reference beam, while the scattered component becomes incoherent after the scattering process. Coherence-gated imaging has been well developed, and some have been commercialized. The most widely used coherence-gating technique is optical coherence tomography (OCT), for which the investigation began in the 1980s, and was first named by Huang et al in 1991 [37]. Although there are many different implementations of coherence-gated imaging, they mainly fall into two categories: single-pixel scanning and whole-field imaging. Furthermore, most coherence-gated techniques employ heterodyne detection to measure weak ballistic signals. For single-pixel scanning, heterodyne detection is usually performed in the time domain since there is no spatial information at each step of the scan. On the other hand, whole-field imaging, which can explore all the pixels in parallel, usually exploits space-domain heterodyne detection to acquire the ballistic signals.

The earliest OCT was implemented by a single-pixel scanning approach. A typical OCT system is consist of a low coherent source and a Michelson interferometer with a sample at the probe arm [38], as shown in Fig. 1.2. The source field can be expressed by $E_i = \mathcal{E}\left(k,\omega\right)e^{i(kz-\omega t)}$, where $\mathcal{E}\left(k,\omega\right)$ is the amplitude of field, k is the wave number, and ω is the angular frequency. The sample is modeled to be multiple reflection layers immersed in a turbid medium. For the sake of simplicity, we assume a 50/50 beam splitter is used, and the reflections in the sample occur at N discrete layers, which can be expressed as

$$r_S\left(z_S\right) = \sum_{n=1}^{N} r_{Sn}\delta\left(z_S - z_{Sn}\right) \tag{1.1}$$

where z_S is the path length in the sample arm, and r_{Sn} is the reflectivity of the layer at location z_{Sn}. All the path lengths are measured from the beam splitter. The electric field returning from the

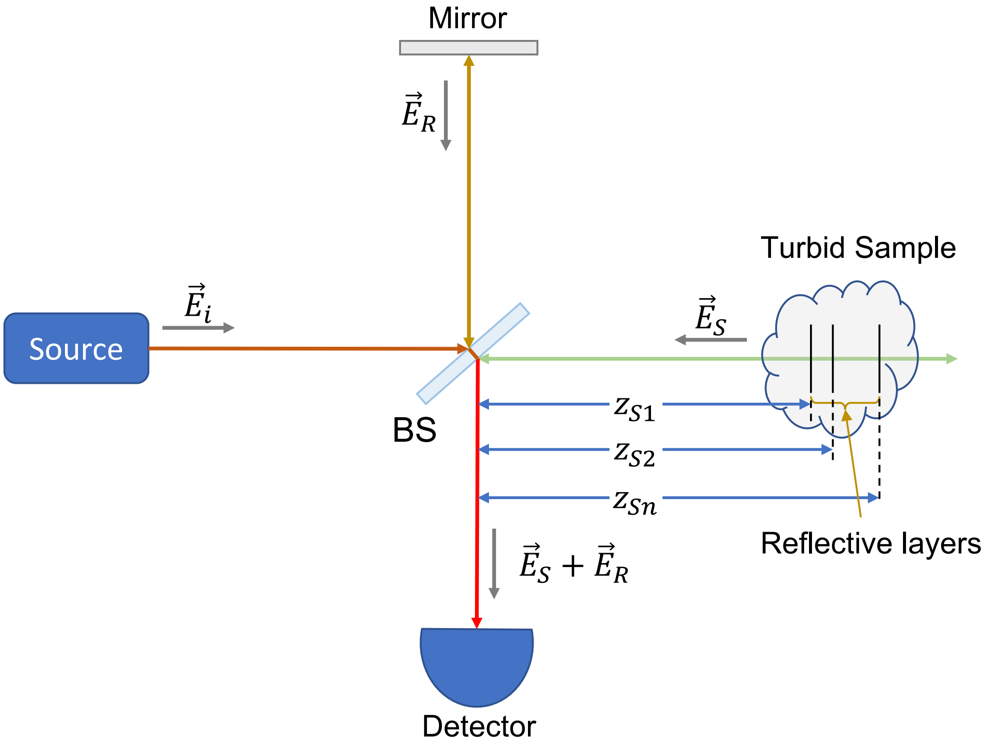

Figure 1.2: Schematic of a Michelson interferometer used in OCT. The incident light beam is split into a reference (reflected) and a probe (transmitted) beam by the beamsplitter (BS). After reflecting back from the sample, the probe beam and reference beam are combined to produce interference, and the spatial information of the internal structure of the sample can be deduced. Adapted from Page 71 of Ref. [38].

reference reflector is given by

$$E_R = \frac{E_i}{\sqrt{2}} r_R e^{i2kz_R} \tag{1.2}$$

and the electric field returning from the sample can be written as

$$\begin{aligned} E_S &= \frac{E_i}{\sqrt{2}} \int_{-\infty}^{\infty} r_S\left(z_S\right) e^{i2kz_S} dz_S && (1.3) \\ &= \frac{E_i}{\sqrt{2}} \sum_{n=1}^{N} r_{Sn} e^{i2kz_{Sn}} && (1.4) \end{aligned}$$

The returning fields interfere at the detector after passing through the beam splitter again, which is found to be

$$
\begin{aligned}
I_D(k) &= \frac{1}{2}\left|E_R + E_S\right|^2 && (1.5)\\
&= \frac{1}{4}I(k)\left(R_R + \sum_{n=1}^{N} R_{Sn}\right) + \frac{1}{2}I(k)\sum_{n=1}^{N}\sqrt{R_R R_{Sn}}\cos\left[2k\left(z_R - z_{Sn}\right)\right]\\
&\quad + \frac{1}{2}I(k)\sum_{n\neq m=1}^{N}\sqrt{R_{Sn}R_{Sm}}\cos\left[2k\left(z_{Sn} - z_{Sm}\right)\right] && (1.6)
\end{aligned}
$$

where $I(k) = \left|\mathcal{E}(k,\omega)\right|^2$, $R_R = \left|r_R\right|^2$ and $R_{Sn} = \left|r_{Sn}\right|^2$. The first term in Eq. (1.6) is a DC component which is independent of the path length. The second term is the cross-correlation between the reflected sample beam and the reference beam, which contains the information of ballistic photons reflected by a layer at location z_{Sn}. This is the desired signal that can generate the image of certain layers inside the sample. Therefore, scanning the reference arm allows the selection of layers at different depths and produces depth-resolved images of the sample. The quality of the three-dimensional images can be greatly improved by implementing the low coherence interferometry in a confocal microscope. The last term in Eq. (1.6) represents the autocorrelation between different sample reflectors and should be eliminated to obtain high-quality images.

The principal drawback of single-pixel scanning is the long image acquisition time. A natural way to overcome this limitation is using an array of detectors, such as a CCD camera, to perform heterodyne detection in parallel and therefore speed up the acquisition rate. This enters the regime of wide-field imaging. Unfortunately, this type of parallelism rejects the use of a confocal filter, and largely increases the chance that scattered light will hit on the detector [1]. In addition, the frame rate of CCD is much lower than the sample rate of single-pixel detectors, so they are not able to perform sampling at high frequency to reduce low-frequency ($1/f$) noise [1]. As a consequence, the SNR is reduced, leading to a much lower penetration depth than that of single-pixel scanning OCT.

In contrast to wide-field OCT, holography is a wide-field technique that fully exploits the spatial heterodyne detection to provide a fast coherence-gated imaging method [39, 40]. In this case, the ballistic light will interfere with the reference beam, and the interference pattern will be recorded in the hologram. The image can be reconstructed by illuminating the hologram with a read-out beam. The wavelength of the read-out beam is different from the source such that scattered light can be eliminated by a filter. Early holography employed photographic film as the recording medium, so the image reconstruction must be completed after the film is chemically processed. Later research has developed real-time methods to perform holographic recording and image reconstruction. One approach is using a CCD camera to record the hologram and reconstructing the image computationally with the knowledge of the reference beam [41, 42, 43, 44, 45]. Digital holography provides more flexibility in image processing since it is done numerically. However, the limitation is also obvious: the scattered light background may saturate the camera and must be subtracted. Another approach is to replace the photographic film with a photorefractive crystal [46]. Light interaction with a photorefractive crystal will lead to optically induced change of refraction index and form a dynamic interference pattern throughout the material, which can be used to record a real-time hologram [47, 48, 49, 50, 51, 52]. Similar to conventional holography, the original image can be read out by a laser at different wavelength from the source, and the scattered light background can be filtered before the reconstructed image is recorded. Compared to digital holography, photorefractive holography has the potential to remove the scattered light background and enhance the dynamic range for the weak signal detection. Nevertheless, the interaction of the read-out beam with the photorefractive material introduces an additional source of noise that is detrimental to the image reconstruction [1].

1.2 Imaging modalities that exploit scattered light

The concept of separating ballistic light fundamentally rejects the majority of photons that could potentially contribute to image an object hidden behind turbid media. This is the main reason that all imaging modalities based on extracting ballistic light suffer from a low SNR and shallow penetration depth. Early experiment using holographic imaging [53] had demonstrated that scattering by stationary media does not erase the spatial information carried by light fields [54]; while the apparent random speckle pattern formed by scattered light is essentially deterministic, and the optical information can be retrieved. The possibility of reconstructing images from scattered light stimulates a lot of efforts in solving this “inverse problem”.

The first demonstration of coherent control of scattered light is dating back to 2007, when Vellekoop and Mosk realized focusing light through a scattering layer in their seminal paper [55]. They constructed a feedback mechanism with a spatial light modulator (SLM) and a CCD camera, which can modify thousands of local phases of the incident wavefront according to the measured intensity speckle at the target plane. The incident wavefront is iteratively optimized at every pixel of the SLM such that the wavefront of scattered light can produce constructive interference at the target location and form a well-defined focus. This work marks the invention of wavefront shaping, which plays an important role in manipulating the light field in complex media [4]. Recent developments in wavefront shaping are all based on this feedback paradigm [56, 57, 58, 59, 60, 61, 62] with more options on the phase control algorithms [63].

Although wavefront shaping has allowed high controllability of light fields in turbid media, the control is highly dependent on the specific medium used in one measurement. Working on a new medium requires the restart of the optimization process with an unknown initial state, making it very difficult to achieve real-time manipulation with electronic feedback and computer-controlled SLM [64]. Optical phase conjugation (OPC) is a technique that can reverse the propagation direction of the light field and keep the wavefront unchanged [65]. When the conjugated field propagates through the scattering medium in the reverse direction, the scattering process is reversed in time, and the incident wavefront is recovered. The idea of phase conjugation can be illustrated by comparing the properties of the light field reflected by a regular mirror with a phase conjugate reflector, as shown in Fig 1.3. Assume the incident light is a plane wave given by

$$E\left(x,y,z;\omega\right)=\mathcal{E}\left(x,y,z\right)e^{ikz}e^{-i\omega t} \tag{1.7}$$

where $\mathcal{E}\left(x,y,z\right)$ is the real amplitude function of the field. After passing through a scattering medium, the transmitted field can be written as

$$E_T(x, y, z; \omega) = \mathcal{E}(x, y, z)\, e^{ikz+\varphi(x,y,z)} e^{-i\omega t} \tag{1.8}$$

where $\varphi(x, y, z)$ is the phase factor describing the distortion of wavefront due to scattering. If the output light is reflected by a regular plane mirror, the reflected field will be

$$E_R(x, y, z; \omega) = R\mathcal{E}(x, y, z)\, e^{-ikz+\varphi(x,y,z)} e^{-i\omega t} \tag{1.9}$$

where R is the reflectivity of the mirror. After passing through the same medium again, the output light is found to be

$$E'_R(x, y, z; \omega) = R\mathcal{E}(x, y, z)\, e^{-ikz+2\varphi(x,y,z)} e^{-i\omega t} \tag{1.10}$$

which indicates the distortion of wavefront originate from the medium is doubled in this case.

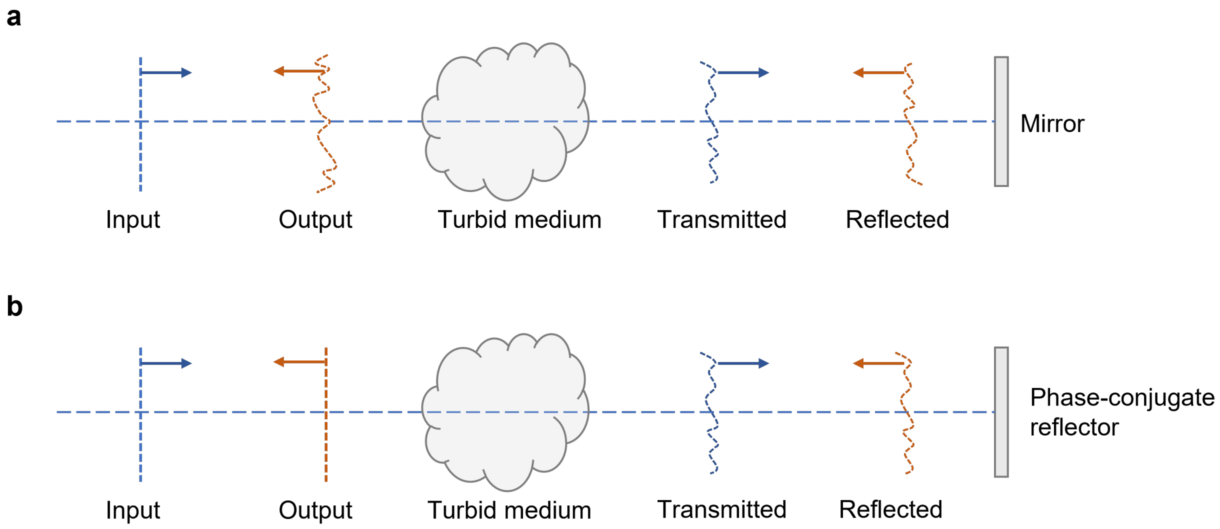

Figure 1.3: Schematic of an optical wavefront reflected by a regular mirror and a phase-conjugate reflector. **a**. A wave reflected by a regular mirror passes through again a complex media. The distortion of wavefront due to scattering is accumulated. **b**. For a phase conjugate reflector, the phase of the reflected wavefront is conjugated, and the distortion of wavefront is offset after the wavefront passes through the scattering medium again. Adapted from Page 136 of Ref. [65].

On the other hand, if the mirror is replaced by a phase conjugate reflector, the reflected field becomes

$$E_{PC}\left(x,y,z;\omega\right)=R'\mathcal{E}\left(x,y,z\right)e^{-ikz-\varphi(x,y,z)}e^{-i\omega t} \tag{1.11}$$

where R' is the reflectivity of the conjugate reflector and the field passing through again the medium becomes

$$E'_{PC}\left(x,y,z;\omega\right)=R'\mathcal{E}\left(x,y,z\right)e^{-ikz}e^{-i\omega t} \tag{1.12}$$

which shows the distortion of the wavefront due to the scattering medium can be eliminated. We call the wave described by Eq. (1.11) “phase conjugate wave".

Depending on whether the propagation direction of the phase conjugate wave is the same as the input wave, OPC can be either in a forward configuration (the same propagation direction) or a backward configuration (the opposite propagation direction). Phase conjugate is usually implemented via nonlinear optical processes, such as four-wave mixing, stimulated scattering, and stimulated emission. One can interpret OPC as being an analog to real-time holography. Under this scenario, three interacting waves are sent into a nonlinear optical material. The refraction index will be changed due to the interaction of pump waves (two of the three) and form a dynamic “diffraction pattern" (variation of refraction index). The third beam, known as the signal wave, will be diffracted by the pattern and read out the phase conjugate wave. OPC has been employed to reverse the scattering process and retrieve an image through turbid media [53, 66].

The requirements of nonlinear materials, specific wavelengths, and high-power lasers make conventional OPC unpractical in many cases. A digital version of OPC (DOPC) is enabled by the invention of SLM, which can overcome some of the drawbacks of its analog counterpart. The basic scheme is to let a signal wave and a reference beam shine on the medium and record the transmitted wave by a camera [67] (see Fig 1.4). The camera has to be matched pixel-to-pixel to a SLM located in the conjugate plane via a beam splitter. Then the pattern recorded on the camera is displayed on the SLM such that the reference beam can be diffracted on the pattern and produce phase conjugate wave emitting in the opposite direction of the signal beam. Recently, DOPC

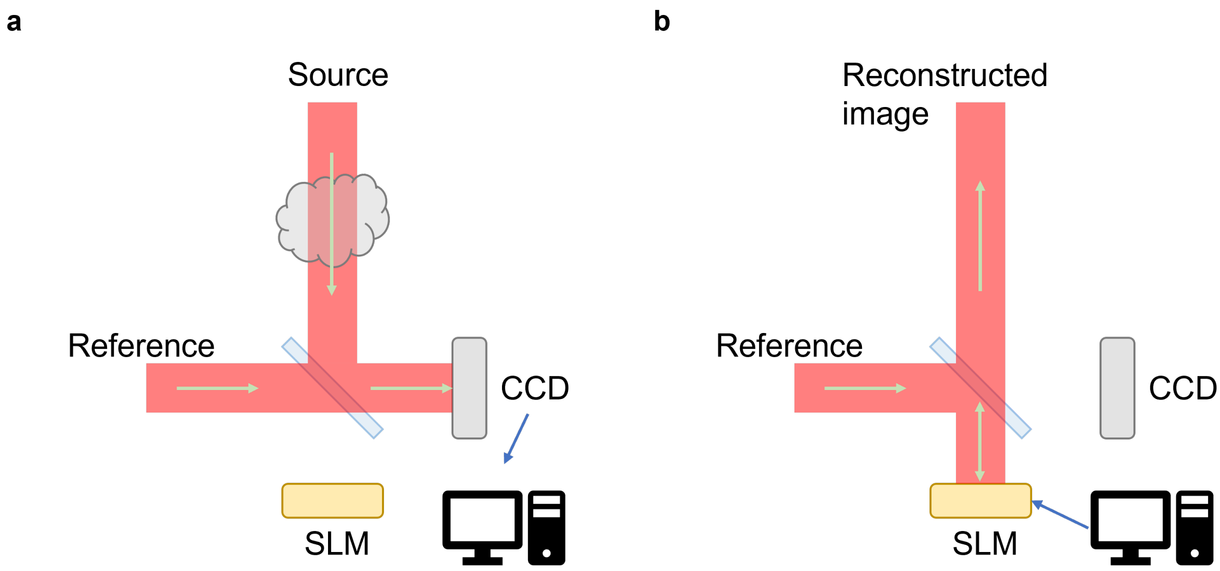

Figure 1.4: Principle of digital optical phase conjugation. **a**. The interference pattern between a reference signal and an input signal to be phase conjugated is recorded by a CCD camera. **b**. The recorded interference pattern is displayed on a SLM, on which the same reference wave is diffracted to generate phase conjugate wave. Adapted from Ref. [67].

has been successfully implemented in optical focusing and imaging through scattering layers and living tissues [67, 68, 69, 70, 71, 72, 73, 74, 75, 76].

As mentioned previously, although the field in complex media is scrambled due to multiple scattering and the transmitted field seems to be random upon phase, propagation and polarization, the process is deterministic: the input wave is precisely mapped to the output wave by the scattering matrix, a well-known concept in the transport theory of mesoscopic system [5]. A scattering matrix is comprised of reflection and transmission matrices (TM) which can be written as [5]

$$\boldsymbol{S} = \begin{pmatrix} \boldsymbol{r} & \boldsymbol{t}' \\ \boldsymbol{t} & \boldsymbol{r}' \end{pmatrix} \tag{1.13}$$

where the diagonal block matrices contain the reflection amplitudes for incoming waves from the left ($\boldsymbol{r}$) and the right ($\boldsymbol{r}'$) of the medium, respectively. The off-diagonal matrices contain the transmission amplitudes for scattering from left to right ($\boldsymbol{t}$) and from right to left ($\boldsymbol{t}'$). With the knowledge of a scattering matrix, it is possible to enable a complete description of scattering in complex media and calculate input optical information from the output fields. Particularly, one can reconstruct the incident field from the transmitted field provided the TM is fully understood.

The monochromatic TM of a scattering layer was first measured by a common-path interferometry and a full-field four-phase method [77]. Optical focusing through the opaque medium was also demonstrated. The measured TM was further used to deliver images through an opaque layer [78]. In addition, the TM method was employed to overcome the diffraction limit of a conventional imaging system [79]. A 5-fold enhancement of the resolution was achieved by exploiting the multiple scattering in turbid media. Despite all that, the measurement of the TM is challenging to perform because of the large number of degree of freedom, the small size of optical channels (up to diffraction-limited spot size), and the requirements of accessing both amplitude and phase information by means of holographic or interferometric technique. Later, a more elegant method was proposed to measure the TM of a scattering medium taking advantage of wavefront shaping and an iterative algorithm of point optimization [80]. The success of the measurement was further verified by the generation of multiple foci through the complex medium. The combination of TM and wavefront shaping also enables enhanced nonlinear imaging through scattering media [81].

Besides acquiring the full knowledge of the TM, the information of the incident optical field can be retrieved by exploiting a unique correlation property of the scattered light field: the scattered wavefront will rotate without change in shape when the incident wavefront also rotates by the same angle. This effect is known as the angular memory effect, which was first proposed in the mesoscopic transport theory of disordered medium [82] and subsequently generalized to the optical field in scattering media [82]. A physical picture of the angular memory effect is illustrated in Fig. 1.5 [6]. The incident wavefront is tilted by an angle $\Delta\theta$. When the scattering medium is thin enough, the sub-sources on the transmitted wavefront will retain the same relative phase due to the tilt, resulting in an overall tilt by the same angle. As a result, the transmitted field projected on the detection plane at distance d will be shifted by $\Delta s = \Delta\theta \cdot d$. This indicates that the speckle pattern at the detection plane is unchanged except for a small transversal shift. The effective range of the

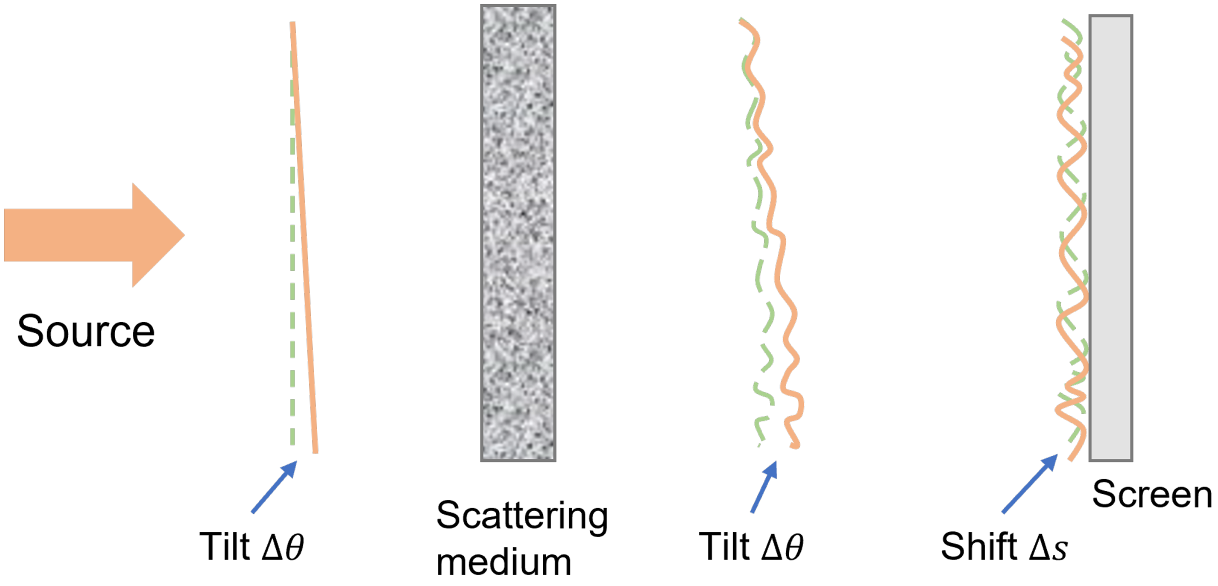

Figure 1.5: Principle of the optical angular memory effect. A tile of the incident wavefront at angle $\Delta\theta$ leads to the same tile on the scattered wavefront, but the shape of the scattered wavefront keeps unchanged. As a result, the speckle pattern at the screen shifts by a distance Δs. Adapted from Ref. [6].

angular memory effect is given by [83]

$$C\left(|\Delta\theta|, L\right) = \left(\frac{k\,|\Delta\theta|\,L}{\sinh\left(k\,|\Delta\theta|\,L\right)}\right)^2 \tag{1.14}$$

in which k is the wavenumber of the incident light, and L is the thickness of the medium. In transmission geometry, a measurable effect can only be observed for a complex medium with thickness less than a few tens of micrometers, according to Eq. (1.14), which limits the application of this configuration to thin media.

Recent studies taking advantage of the angular memory effect have enabled non-invasive imaging through scattering layers with angular scans of coherent laser [83] and single-shot measurement of incoherent sources [84, 85, 86]. The scheme is further developed to image moving objects behind scattering media [87]. All the techniques use the fact that the autocorrelation of the speckle is nearly a delta function, and the measured intensity is a convolution of the object and the speckle.

Therefore, the autocorrelation of the measured is essentially equal to the autocorrelation of the object. The image of the object can be reconstructed from the autocorrelation by some phase-retrieval algorithms [88, 89]. Memory effect has also be combined with OPC to implement optical focusing through complex media [90]. The chief advantage of these techniques is that they do not depend on the detailed knowledge of the scattering events in the media. Nevertheless, they share some common shortcomings: (i) the memory-effect range restricts this approach to thin scattering layers; (ii) the small single speckle grain requires a high-resolution camera to resolve; (iii) the iterative phase-retrieval algorithm suffers from falling into local optimal solutions.

1.3 Other imaging modalities

Many other techniques have addressed the problem of imaging through scattering media from different perspectives. One simple method exploits the fact that the input optical information is degraded in space but largely retained in time. Therefore, if one can embed a time-domain "tag" into the incident light and extracts this tag in the transmitted light, an image of objects with a high contrast of reflectivity can be obtained by scanning the object pixel by pixel. This idea has been realized by polarization modulation [91, 92, 93], in which the polarization of the source is modulated to rotate at certain frequency such as the polarization analyzer can generate a sinusoidal component of the transmitted light, and the modulation frequency is acquired by performing fast Fourier transform (FFT) to the recorded signal at every pixel. Since the reflectivity of the object is position-dependent, the spectral intensities of the modulation frequency of all the scanning points will jointly produce an image of the object. This method is also used to generate a full-field image through scattering media provided the object is self-illuminated with sinusoidally modulated intensity [94]. More recently, using a 2D optical frequency comb, real-time frequency-encoded spatiotemporal focusing and imaging through scattering media is achieved for ground glass diffusers and living tissues [95].

Similar insight has been transplanted to ultrasound-assisted optical imaging. Unlike optical waves, ultrasound waves can propagate through scattering media without obvious distortion up to 1-100 mm in depth [6]. The penetration depth can be translated to optical waves via two types of ultrasound-light interactions: the frequency shift of the optical waves due to ultrasound-induced refractive index grating and the generation of ultrasound via thermal expansion of the media due to the absorption of optical energy. The two mechanisms have led to the development of ultrasound-modulated optical tomography [96, 97] and photo-acoustic tomography [96, 98], which are intensively used in biomedical imaging. More recently, speckle-encoded ultrasound-modulated light correlation has been implemented to image fluorescent objects through dynamic scattering media [99]. However, the main disadvantage of using ultrasound is the reduced imaging resolution. For commonly used ultrasound in 1-50 MHz, the resolution is 20-1000 μm, which is far above the optical diffraction limit. Higher frequency may improve the resolution, but also suffers from great attenuation in scattering media.

2. THEORETICAL DESCRIPTION OF OPTICAL IMAGING THROUGH SCATTERING MEDIUM

In this chapter, we introduce some basic concepts of imaging and scattering media, and develop a general formulation for imaging systems with scattering media.

2.1 Electromagnetic wave in vacuum

We begin with a review of the classical electromagnetic theory of light, as most of work in this dissertation can be well understood within the frame of classical theory. The set of Maxwell equations is the foundation of classical electromagnetic theory. Heinrich Hertz conducted a series of experiments between 1886 and 1889 that conclusively proved the existence of the electromagnetic radiation predicted by Maxwell equations. These experiments also demonstrated that light is a form of electromagnetic radiation. Maxwell's equations in source-free vacuum have the form [100]

$$\nabla \times \boldsymbol{E} + \frac{\partial \boldsymbol{B}}{\partial t} = 0, \tag{2.1}$$

$$\nabla \times \boldsymbol{H} - \frac{\partial \boldsymbol{D}}{\partial t} = 0, \tag{2.2}$$

$$\nabla \cdot \boldsymbol{D} = 0, \tag{2.3}$$

$$\nabla \cdot \boldsymbol{B} = 0, \tag{2.4}$$

with the constitutive relations

$$\boldsymbol{D} = \epsilon_0 \boldsymbol{E}, \tag{2.5}$$

$$\boldsymbol{B} = \mu_0 \boldsymbol{H}, \tag{2.6}$$

where the electric (magnetic) field $\boldsymbol{E}$ ($\boldsymbol{H}$) is connected to electric displacement $\boldsymbol{D}$ (magnetic induction $\boldsymbol{H}$) by free-space electric permittivity ϵ_0 (magnetic permeability μ_0). Eq. (2.1) and (2.2) are coupled partial differential equations describing the time evolution of $\boldsymbol{E}\left(\boldsymbol{r}, t\right)$ and $\boldsymbol{B}\left(\boldsymbol{r}, t\right)$. Eq.

(2.3) and Eq. (2.4) set the initial conditions for the source-free vacuum. This can be more explicit if we take the divergence of Eq. (2.1) and (2.2):

$$\frac{\partial}{\partial t}\left(\nabla \cdot \boldsymbol{B}\right) = 0, \tag{2.7}$$

$$\frac{\partial}{\partial t}\left(\nabla \cdot \boldsymbol{D}\right) = 0, \tag{2.8}$$

which imply that the fields are divergence-free all the time if they are divergence-free at $t = 0$ as indicating by (2.3) and Eq. (2.4).

The electric and magnetic fields also obey a vector form of wave equation independently. To see this, substitute Eq. (2.2) into the curl of Eq. (2.1) and use the vector identity

$$\nabla \times \left(\nabla \times \boldsymbol{a}\right) = \nabla \left(\nabla \cdot \boldsymbol{a}\right) - \nabla^2 \boldsymbol{a} \tag{2.9}$$

as well as Eq. (2.3). The result is

$$\nabla^2 \boldsymbol{E} - \frac{1}{c^2}\frac{\partial^2 \boldsymbol{E}}{\partial t^2} = 0, \tag{2.10}$$

where $c \equiv 1/\sqrt{\epsilon_0 \mu_0}$ is the speed of light in vaccum. Similarly, substituting Eq. (2.1) into the curl of Eq. (2.2) will yield the wave equation for magnetic field

$$\nabla^2 \boldsymbol{H} - \frac{1}{c^2}\frac{\partial^2 \boldsymbol{H}}{\partial t^2} = 0. \tag{2.11}$$

As we can see, each Cartesian component of $\boldsymbol{E}\left(\boldsymbol{r}, t\right)$ and $\boldsymbol{H}\left(\boldsymbol{r}, t\right)$ satisfies a scalar wave equation of the same structure, which is given by

$$\nabla^2 u - \frac{1}{c^2}\frac{\partial^2 u}{\partial t^2} = 0, \tag{2.12}$$

where $u\left(\boldsymbol{r}, t\right)$ is an arbitrary function of space and time. Now, suppose $u\left(\boldsymbol{r}, t\right)$ can be expressed in Fourier integral representation

$$u\left(\boldsymbol{r},t\right)=\frac{1}{2\pi}\int_{-\infty}^{+\infty}u\left(\boldsymbol{r},\omega\right)e^{-i\omega t}d\omega \tag{2.13}$$

where

$$u\left(\boldsymbol{r},\omega\right)=\int_{-\infty}^{+\infty}u\left(\boldsymbol{r},t\right)e^{i\omega t}d\omega \tag{2.14}$$

is the inverse transform. Substituting Eq. (2.13) into Eq. (2.12), it is easy to find the well-known Helmholtz equation for $u\left(\boldsymbol{r},\omega\right)$

$$\nabla^2 u\left(\boldsymbol{r},\omega\right)+k^2 u\left(\boldsymbol{r},\omega\right)=0 \tag{2.15}$$

where $k=\omega/c$ is the wave number. According to Eq. (2.13), a general solution of Eq. (2.15) gives a general solution of the wave equation (Eq. (2.12)). Using Fourier representation allows us to understand the behavior of a single frequency component $U\left(\boldsymbol{r},\omega\right)$ by which the behavior of $u\left(\boldsymbol{r},t\right)$ can be determined according to Eq. (2.13). A possible solution of Eq. (2.15) is the monochromatic plane wave with a single frequency ω_0, which is given by

$$u\left(\boldsymbol{r},\omega\right)=u_k\delta\left(\omega-\omega_0\right)e^{i\boldsymbol{k}\cdot\boldsymbol{r}}, \tag{2.16}$$

where u_k is the complex amplitude associated with mode $\boldsymbol{k}$. Therefore, we have a general solution of the wave equation (Eq. (2.12))

$$u\left(\boldsymbol{r},t\right)=u_k e^{i(\boldsymbol{k}\cdot\boldsymbol{r}-\omega_0 t)}+\text{c.c.} \tag{2.17}$$

in which c.c. stands for the complex conjugate. With the convention that the real parts of complex quantities are the physical fields, we can write the electric and magnetic fields as

$$\boldsymbol{E}\left(\boldsymbol{r},t\right)=\boldsymbol{E}_k e^{i(\boldsymbol{k}\cdot\boldsymbol{r}-\omega_0 t)} \tag{2.18}$$

$$\boldsymbol{H}(\boldsymbol{r},t) = \boldsymbol{H}_k e^{i(\boldsymbol{k}\cdot\boldsymbol{r}-\omega t)} \tag{2.19}$$

where $\boldsymbol{E}_k$ and $\boldsymbol{H}_k$ are constant vectors. Due to the linear nature of Maxwell equations, any linear superposition of the plane-wave solution (Eq. (2.18) and Eq. (2.19)) is also a solution of the wave equation (Eq. (2.10) and Eq. (2.11)). The linearity also allows the decomposition of a complex radiation field into a linear superposition of elementary solutions of the wave equations.

There remains some restrictions for $\boldsymbol{E}(\boldsymbol{r},t)$ and $\boldsymbol{H}(\boldsymbol{r},t)$ to satisfy Maxwell equations. It follows from the divergence equations (Eq. (2.3) and Eq. (2.4)) that

$$\boldsymbol{k}\cdot\boldsymbol{E} = 0 \tag{2.20}$$

$$\boldsymbol{k}\cdot\boldsymbol{H} = 0 \tag{2.21}$$

which indicate both the electric and magnetic fields are perpendicular to the direction of propagation. Let us denote $\boldsymbol{k} = k\hat{\boldsymbol{k}}$ where $\hat{\boldsymbol{k}}$ is a unit vector. The curl equations further require that

$$c\boldsymbol{B}(\boldsymbol{r},t) = \hat{\boldsymbol{k}} \times \boldsymbol{E}(\boldsymbol{r},t) \tag{2.22}$$

which implies the vectors $\left(\hat{\boldsymbol{k}}, \boldsymbol{E}, \boldsymbol{B}\right)$ form a right-handed orthogonal system. It follows directly from Eq. (2.22) that

$$|\boldsymbol{E}| = c\,|\boldsymbol{B}| \tag{2.23}$$

2.2 Linear system

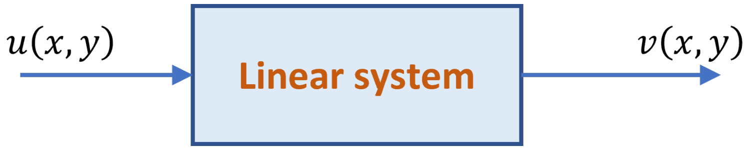

Figure 2.1: A linear system diagram. $u(x,y)$ is the input, and $v(x,y)$ is the output. Adapted from Page 7 of Ref. [101].

An optical imaging systems is often modeled as a linear system in which a given input is mapped to a unique output [101, 102]. Consider a system shown in Fig. 2.1, where $u\left(x,y\right)$ is the input signal and $v\left(x,y\right)$ is the output signal. The input-output mapping can be written as

$$v\left(x,y\right)=\hat{O}u\left(x,y\right) \tag{2.24}$$

where $\hat{O}$ is an operator denoting the operation imposed on the input by the system. The system is called linear if the following equation is obeyed for any input $u_1\left(x,y\right)$ and $u_2\left(x,y\right)$

$$\hat{O}\left[c_1u_1\left(x,y\right)+c_2u_2\left(x,y\right)\right]=c_1\hat{O}u_1\left(x,y\right)+c_2\hat{O}u_2\left(x,y\right) \tag{2.25}$$

where c_1 and c_2 are complex constants. Using the delta function, $u\left(x,y\right)$ can be expressed as

$$u\left(x,y\right)=\iint_{-\infty}^{\infty}u\left(x_1,y_1\right)\delta\left(x-x_1,y-y_1\right)dx_1dy_2 \tag{2.26}$$

It follows that the output can be written as

$$\begin{aligned}v\left(x,y\right)&=\hat{O}u\left(x,y\right)\\&=\iint_{-\infty}^{\infty}u\left(x_1,y_1\right)\hat{O}\left[\delta\left(x-x_1,y-y_1\right)\right]dx_1dy_2\\&=\iint_{-\infty}^{\infty}u\left(x_1,y_1\right)h\left(x,y;x_1,y_1\right)dx_1dy_2\end{aligned} \tag{2.27}$$

in which

$$h\left(x,y;x_1,y_1\right)\equiv\hat{O}\left[\delta\left(x-x_1,y-y_1\right)\right] \tag{2.28}$$

is the impulse response of the system characterizing the response of the system to point sources (delta function). Eq. (2.27) is known as the superposition integral, which implies that the output corresponding to a given input is determined once the impulse response is known. In the context of optics, the impulse response is usually called point-spread function.

A linear system is said to be shift-invariant (or space-invariant) if its impulse response depends only on the transversal distance $(x - x_1)$ and $(y - y_1)$. In such a system, any translation of the input results in the same translation of the output, and the impulse response can be written as

$$h(x, y; x_1, y_1) = h(x - x_1, y - y_1) \tag{2.29}$$

Substituting Eq. (2.29) back into Eq. (2.27), we have

$$\begin{aligned} v(x, y) &= \iint_{-\infty}^{\infty} u(x_1, y_1)\, h(x - x_1, y - y_1)\, dx_1 dy_2 \\ &= \iint_{-\infty}^{\infty} h(\xi, \eta)\, u(x - \xi, y - \eta)\, d\xi d\eta \end{aligned} \tag{2.30}$$

in which the second line can be reached by a change of variables $\xi = x - x_1$ and $\eta = y - y_1$. The right-hand side of Eq. (2.30) is exactly a 2D convolution of $h(x, y)$ and $u(x, y)$, which is often expressed symbolically as

$$v(x, y) = h(x, y) * u(x, y) \tag{2.31}$$

Now, if we take the Fourier transform of both sides of Eq. (2.31) and apply the convolution theorem, we end up with a simple relation between the spectra of the system output and input

$$V(f_x, f_y) = H(f_x, f_y)\, U(f_x, f_y) \tag{2.32}$$

where

$$H(f_x, f_y) = \iint_{-\infty}^{\infty} h(\xi, \eta)\, e^{-i2\pi(f_x \xi + f_y \eta)} d\xi d\eta \tag{2.33}$$

is the transfer function of the system. The transfer function provides a frequency-domain description of the effects of the system on the input. Note that the computationally expensive convolution operation in Eq. (2.31) is replaced by a simple multiplication in Eq. (2.33). The output in space-domain can then be obtained by the inverse Fourier transform of $V(f_x, f_y)$

$$v(x, y) = \iint_{-\infty}^{\infty} V(f_x, f_y)\, e^{i2\pi(x f_x + y f_y)} df_x df_y \tag{2.34}$$

Frequency-domain representation of the input-output relation with transfer function makes it very simple to deal with a shift-invariant linear system consists of shift-invariant linear sub-systems, which is usually the case in an experimental setup of optics. Let's consider such a system with two sub-systems, as shown in Fig. 2.2. The output $v_1(x, y)$ of the sub-system 1 is the input of the sub-system 2. Using Eq. (2.31), the final output (output of sub-system 2) can be obtained as

$$\begin{aligned} v_2(x, y) &= h_2(x, y) * v_1(x, y) \\ &= h_2(x, y) * [h_1(x, y) * u(x, y)] \end{aligned} \tag{2.35}$$

and the frequency-domain representation is given by

$$V_2(f_x, f_y) = H_2(f_x, f_y) H_1(f_x, f_y) U(f_x, f_y) \tag{2.36}$$

Eq. (2.36) shows that the effects of the whole system on the input u can be broken into successive operations of the sub-systems on the input u in frequency-domain, which greatly simplifies the description of complex systems.

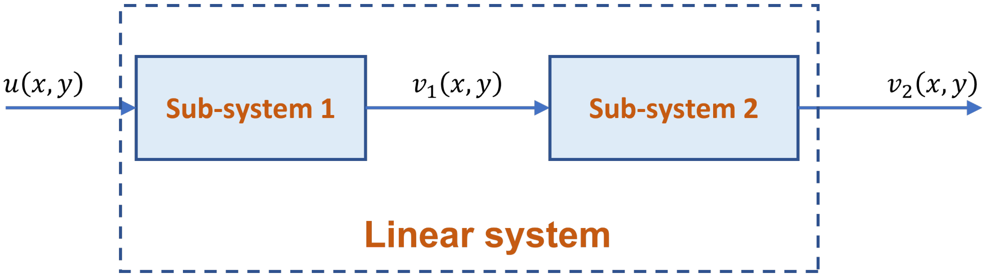

Figure 2.2: A linear system with two sub-systems.

2.3 Field propagation in optical imaging system

In this section, we are going to discuss the propagation of electromagnetic radiation in free space [103, 100]. Specifically, we are interested in determining the profile of $E(\boldsymbol{r}, t)$ on a transverse plane of $z = c$ from a given distribution of the field $E(\boldsymbol{r}_0, t_0)$ on a plane of $z_0 = 0$. We assume that the distance between the receiver plane $z = c$ and the emitter plane $z_0 = 0$ is arbitrary, and only one polarization direction is considered.

The monochromatic plane-wave solution of source-free Maxwell equations given by Eq. (2.18) cannot exist in nature because it fills all the space. However, the principle of linear superposition allows us to synthesize solutions that do not extend infinitely in any direction. Real sources can only generate these kinds of waves, which are called wave packets. Using Eq. (2.18) as basis functions, the fields of an electromagnetic wave packet have a general form of

$$\boldsymbol{E}(\boldsymbol{r}, t) = \frac{1}{(2\pi)^3} \int d^3k \boldsymbol{E}(\boldsymbol{k}) \exp\{i(\boldsymbol{k} \cdot \boldsymbol{r} - \omega t)\} \tag{2.37}$$

where $\boldsymbol{E}(\boldsymbol{k})$ is the complex amplitude of the mode $\boldsymbol{k}$ and $\omega = ck$ is the associated frequency. Similarly, $E(\boldsymbol{r}_0, t_0)$ can be written as

$$E(\boldsymbol{r}_0, t_0) = \int d^3k E(\boldsymbol{k}) u_k(\boldsymbol{r}_0, t_0) \tag{2.38}$$

where $u_k(\boldsymbol{r}_0, t_0)$ is a solution of the Helmholtz equation (Eq.(2.15)) under certain boundary conditions, and the factor of $1/(2\pi)^3$ is omitted for the sake of simplicity. In principle, we can find a field propagator (or Green's function) that propagates each mode from one point $\boldsymbol{r}_0$ on the plane $z_0 = 0$ to another point $\boldsymbol{r}$ on the receiver plane $z = c$, and the observed field is given by

$$\begin{aligned} E(\boldsymbol{r}, t) &= \int d^3k E(\boldsymbol{k}) g(\boldsymbol{k}, \boldsymbol{r} - \boldsymbol{r}_0, t - t_0) u_k(\boldsymbol{r}_0, t_0) \\ &= \int d^3k E(\boldsymbol{k}, \boldsymbol{r}_0, t_0) g(\boldsymbol{k}, \boldsymbol{r} - \boldsymbol{r}_0, t - t_0) \end{aligned} \tag{2.39}$$

where $E(\boldsymbol{k}, \boldsymbol{r}_0, t_0) = E(\boldsymbol{k}) u_k(\boldsymbol{r}_0, t_0)$. For typical optical imaging setups, the propagation of the fields from the object plane to the image plane may be decomposed into propagation in N steps.

In these cases, the field at the final receiver plane can be expressed by

$$E(\boldsymbol{r},t) = \int d^3k E(\boldsymbol{k},\boldsymbol{r}_0,t_0)\, g_1(\boldsymbol{k},\boldsymbol{r}_1-\boldsymbol{r}_0,t_1-t_0) \\ \times g_2(\boldsymbol{k},\boldsymbol{r}_2-\boldsymbol{r}_1,t_2-t_1)\times\cdots\times g_N(\boldsymbol{k},\boldsymbol{r}-\boldsymbol{r}_{N-1},t-t_{N-1}) \tag{2.40}$$

where N denotes the number of steps. For certain optical imaging setups, it is more convenient to write Eq. (2.39) as

$$E(\boldsymbol{\rho},z,t) = \int d^3k E(\boldsymbol{k};\boldsymbol{\rho}_0,z_0,t_0)\, g(\boldsymbol{k};\boldsymbol{\rho}-\boldsymbol{\rho}_0,z-z_0,t-t_0) \tag{2.41}$$

where $\boldsymbol{\rho}$ and z are the coordinates in the transverse plane and longitudinal plane, respectively.

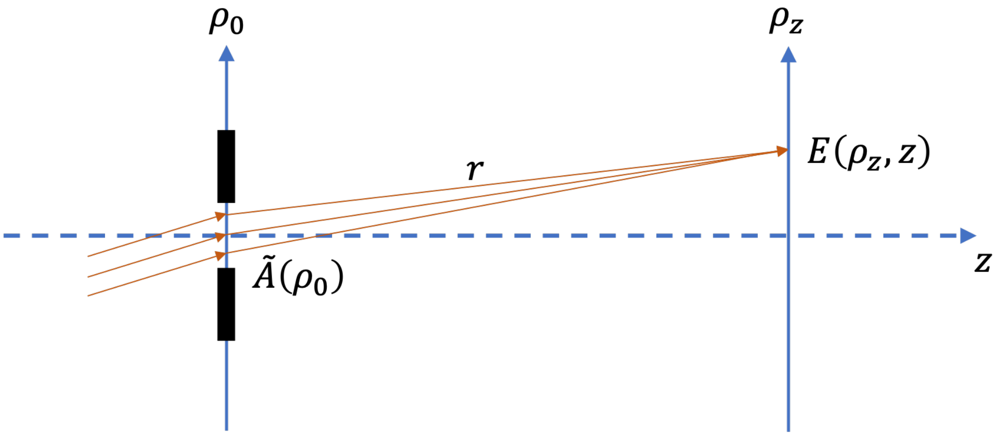

Figure 2.3: Schematic of free-space Fresnel diffraction. $\boldsymbol{\rho}_0$ is the aperture plane and $\boldsymbol{\rho}_z$ is the receiver plane. The field on each point of the $\boldsymbol{\rho}_z$ plane is a superposition of all the sub-fields propagating from the $\boldsymbol{\rho}_0$ plane. Adapted from Page 48 of Ref. [100].

To understand the concept of field propagator, let's evaluate $g(\boldsymbol{k};\boldsymbol{\rho},z,t)$ for the free-space Fresnel diffraction as an example. As shown in Fig. 2.3, the field travels freely from an aperture A of finite size in the plane $\boldsymbol{\rho}_0$ to the receiver plane $\boldsymbol{\rho}_z$. According to Huygens-Fresnel principle, $E(\boldsymbol{\rho}_z,z,t)$ is a superposition of the secondary spherical wavefront that emitted from each point on the $\boldsymbol{\rho}_0$ plane

$$E\left(\boldsymbol{\rho}_z, z, t\right) = \int d^3k E\left(\boldsymbol{k}\right) \int d\boldsymbol{\rho}_0 \tilde{A}\left(\boldsymbol{\rho}_0\right) \frac{\exp\left\{i\left(kr - \omega t\right)\right\}}{r} \tag{2.42}$$

in which we have set $z_0 = 0$ and $t_0 = 0$, and $\tilde{A}\left(\boldsymbol{\rho}_0\right)$ is the complex amplitude describing the relative distribution of the field on the plane $\boldsymbol{\rho}_0$. The integration over $\boldsymbol{\rho}_0$ is due to the superstition of the wavefront. Comparing Eq. (2.42) with Eq. (2.41), we can find the field propagator as

$$g\left(\boldsymbol{k}; \boldsymbol{\rho}_z, z, t\right) = \int d\boldsymbol{\rho}_0 \tilde{A}\left(\boldsymbol{\rho}_0\right) \frac{\exp\left\{i\left(kr - \omega t\right)\right\}}{r} \tag{2.43}$$

In the near-field paraxial approximation where $\left|\boldsymbol{\rho}_z - \boldsymbol{\rho}_0\right|^2 \ll z^2$, r can be approximated by its first-order expansion

$$r = \sqrt{z^2 + \left|\boldsymbol{\rho}_z - \boldsymbol{\rho}_0\right|^2} \approx z\left(1 + \frac{\left|\boldsymbol{\rho}_z - \boldsymbol{\rho}_0\right|^2}{2z^2}\right) \tag{2.44}$$

Therefore, $g\left(\boldsymbol{k}; \boldsymbol{\rho}_z, z, t\right)$ can be written as

$$\begin{aligned} g\left(\boldsymbol{k}; \boldsymbol{\rho}_z, z, t\right) &= \frac{e^{i\frac{\omega}{c}z - i\omega t}}{z} \int d\boldsymbol{\rho}_0 \tilde{A}\left(\boldsymbol{\rho}_0\right) e^{i\frac{\omega}{2cz}\left|\boldsymbol{\rho}_z - \boldsymbol{\rho}_0\right|^2} \\ &= \frac{e^{i\frac{\omega}{c}z - i\omega t}}{z} \int d\boldsymbol{\rho}_0 \tilde{A}\left(\boldsymbol{\rho}_0\right) G\left(\boldsymbol{\rho}_z - \boldsymbol{\rho}_0, \frac{\omega}{cz}\right) \end{aligned} \tag{2.45}$$

where we have defined the Fresnel phase factor

$$G\left(\boldsymbol{\alpha}, \beta\right) = \exp\left\{\frac{i\beta\left|\boldsymbol{\alpha}\right|^2}{2}\right\} \tag{2.46}$$

$G\left(\boldsymbol{\alpha}, \beta\right)$ has some properties that are very useful in calculating the field propagator $g\left(\boldsymbol{k}; \boldsymbol{\rho}_z, z, t\right)$. We list these properties as follows:

$$G^*\left(\boldsymbol{\alpha}, \beta\right) = G\left(\boldsymbol{\alpha}, -\beta\right) \tag{2.47}$$

$$G\left(\boldsymbol{\alpha}, \beta_1 + \beta_2\right) = G\left(\boldsymbol{\alpha}, \beta_1\right) G\left(\boldsymbol{\alpha}, \beta_2\right) \tag{2.48}$$

$$G\left(\boldsymbol{\alpha}_1+\boldsymbol{\alpha}_2,\beta\right)=G\left(\boldsymbol{\alpha}_1,\beta\right)G\left(\boldsymbol{\alpha}_2,\beta\right)e^{i\beta\boldsymbol{\alpha}_1\cdot\boldsymbol{\alpha}_2} \tag{2.49}$$

$$\int d\boldsymbol{\alpha}G\left(\boldsymbol{\alpha},\beta\right)e^{i\boldsymbol{\gamma}\cdot\boldsymbol{\alpha}}=\frac{2\pi i}{\beta}G\left(\boldsymbol{\gamma},-\frac{1}{\beta}\right) \tag{2.50}$$

Eq. (2.47) $\sim$ (2.49) are straightforward to show, and a proof of Eq. (2.50) is provided in Appendix A.

The above field propagator is calculated directly from the plane $\boldsymbol{\rho}_0$ to the plane $\boldsymbol{\rho}_z$. What if we insert a plane $\boldsymbol{\rho}_1$ in between and calculate $g\left(\boldsymbol{k};\boldsymbol{\rho}_z,z,t\right)$ in two steps? This is equivalent to two successive Fresnel diffraction over distance z_1 (from $\boldsymbol{\rho}_0$ to $\boldsymbol{\rho}_1$) and z_2 (from $\boldsymbol{\rho}_1$ to $\boldsymbol{\rho}_z$), and the result should be the same propagator as that of the direct calculation discussed previously

$$g\left(\boldsymbol{k};\boldsymbol{\rho}_z,z,t\right)=C^2\frac{e^{i\frac{\omega}{c}(z_1+z_2)-i\omega(t_1+t_2)}}{z_1z_2}\iint d\boldsymbol{\rho}_1d\boldsymbol{\rho}_0\tilde{A}\left(\boldsymbol{\rho}_0\right)G\left(\boldsymbol{\rho}_1-\boldsymbol{\rho}_0,\frac{\omega}{cz_1}\right)G\left(\boldsymbol{\rho}_z-\boldsymbol{\rho}_1,\frac{\omega}{cz_2}\right) \tag{2.51}$$

$$=C\frac{e^{i\frac{\omega}{c}z-i\omega t}}{z}\int d\boldsymbol{\rho}_0\tilde{A}\left(\boldsymbol{\rho}_0\right)G\left(\boldsymbol{\rho}_z-\boldsymbol{\rho}_0,\frac{\omega}{cz}\right) \tag{2.52}$$

where C is a normalization constant. Note that

$$\begin{aligned}
&G\left(\boldsymbol{\rho}_1-\boldsymbol{\rho}_0,\frac{\omega}{cz_1}\right)G\left(\boldsymbol{\rho}_z-\boldsymbol{\rho}_1,\frac{\omega}{cz_2}\right)\\
&=G\left(\boldsymbol{\rho}_1,\frac{\omega}{cz_1}\right)G\left(\boldsymbol{\rho}_0,\frac{\omega}{cz_1}\right)e^{-i\frac{\omega}{cz_1}\boldsymbol{\rho}_1\cdot\boldsymbol{\rho}_0}G\left(\boldsymbol{\rho}_z,\frac{\omega}{cz_2}\right)G\left(\boldsymbol{\rho}_1,\frac{\omega}{cz_2}\right)e^{-i\frac{\omega}{cz_2}\boldsymbol{\rho}\cdot\boldsymbol{\rho}_1}\\
&=G\left(\boldsymbol{\rho}_0,\frac{\omega}{cz_1}\right)G\left(\boldsymbol{\rho}_z,\frac{\omega}{cz_2}\right)G\left(\boldsymbol{\rho}_1,\frac{\omega}{c}\left(\frac{1}{z_1}+\frac{1}{z_2}\right)\right)\exp\left\{-i\frac{\omega}{c}\left(\frac{\boldsymbol{\rho}_0}{z_1}+\frac{\boldsymbol{\rho}_z}{z_2}\right)\cdot\boldsymbol{\rho}_1\right\}
\end{aligned} \tag{2.53}$$

We evaluate the integral in Eq. (2.51) as follows:

$$\begin{aligned}
&C^2\frac{e^{i\frac{\omega}{c}(z_1+z_2)}}{z_1z_2}\int d\boldsymbol{\rho}_1\int d\boldsymbol{\rho}_0\tilde{A}\left(\boldsymbol{\rho}_0\right)G\left(\boldsymbol{\rho}_1-\boldsymbol{\rho}_0,\frac{\omega}{cz_1}\right)G\left(\boldsymbol{\rho}_z-\boldsymbol{\rho}_1,\frac{\omega}{cz_2}\right)\\
&=C^2\frac{e^{i\frac{\omega}{c}(z_1+z_2)}}{z_1z_2}\int d\boldsymbol{\rho}_0\tilde{A}\left(\boldsymbol{\rho}_0\right)G\left(\boldsymbol{\rho}_0,\frac{\omega}{cz_1}\right)G\left(\boldsymbol{\rho}_z,\frac{\omega}{cz_2}\right)
\end{aligned} \tag{2.54}$$

$$\times\int d\boldsymbol{\rho}_1G\left(\boldsymbol{\rho}_1,\frac{\omega}{c}\left(\frac{1}{z_1}+\frac{1}{z_2}\right)\right)\exp\left\{-i\frac{\omega}{c}\left(\frac{\boldsymbol{\rho}_0}{z_1}+\frac{\boldsymbol{\rho}_z}{z_2}\right)\cdot\boldsymbol{\rho}_1\right\} \tag{2.55}$$

where the integration over $\boldsymbol{\rho}_1$ is evaluated to be

$$\begin{aligned}
&\int d\boldsymbol{\rho}_1 G\left(\boldsymbol{\rho}_1, \frac{\omega}{c}\left(\frac{1}{z_1}+\frac{1}{z_2}\right)\right)\exp\left\{-i\frac{\omega}{c}\left(\frac{\boldsymbol{\rho}_0}{z_1}+\frac{\boldsymbol{\rho}_z}{z_2}\right)\cdot\boldsymbol{\rho}_1\right\}\\
=&i\frac{2\pi}{\frac{\omega}{c}\left(\frac{1}{z_1}+\frac{1}{z_2}\right)}G\left(\frac{\omega}{c}\left|\frac{\boldsymbol{\rho}_0}{z_1}+\frac{\boldsymbol{\rho}_z}{z_2}\right|, -\frac{1}{\frac{\omega}{c}\left(\frac{1}{z_1}+\frac{1}{z_2}\right)}\right)\\
=&\frac{i2\pi c}{\omega}\frac{z_1 z_2}{z_1+z_2}G\left(\boldsymbol{\rho}_0, -\frac{\omega}{c}\frac{z_2}{z_1\left(z_1+z_2\right)}\right)G\left(\boldsymbol{\rho}_z, -\frac{\omega}{c}\frac{z_1}{z_2\left(z_1+z_2\right)}\right)\exp\left\{-i\frac{\omega}{c}\frac{\boldsymbol{\rho}_0\cdot\boldsymbol{\rho}_z}{z_1+z_2}\right\} \quad (2.56)
\end{aligned}$$

On substituting Eq. (2.56) back into Eq. (2.54) and using the relations

$$G\left(\boldsymbol{\rho}_0, \frac{\omega}{cz_1}\right)G\left(\boldsymbol{\rho}_0, -\frac{\omega}{c}\frac{z_2}{z_1\left(z_1+z_2\right)}\right) = G\left(\boldsymbol{\rho}_0, \frac{\omega}{c\left(z_1+z_2\right)}\right) \tag{2.57}$$

$$G\left(\boldsymbol{\rho}_z, \frac{\omega}{cz_2}\right)G\left(\boldsymbol{\rho}_z, -\frac{\omega}{c}\frac{z_1}{z_2\left(z_1+z_2\right)}\right) = G\left(\boldsymbol{\rho}_z, \frac{\omega}{c\left(z_1+z_2\right)}\right) \tag{2.58}$$

we obtain

$$\begin{aligned}
g\left(\boldsymbol{k};\boldsymbol{\rho}_z,z,t\right) &= C^2\frac{i2\pi c}{\omega}\frac{e^{i\frac{\omega}{c}\left(z_1+z_2\right)-i\omega\left(t_1+t_2\right)}}{z_1+z_2}\int d\boldsymbol{\rho}_0\tilde{A}\left(\boldsymbol{\rho}_0\right)G\left(\boldsymbol{\rho}_0, \frac{\omega}{c\left(z_1+z_2\right)}\right)\\
&\quad\times G\left(\boldsymbol{\rho}_z, \frac{\omega}{c\left(z_1+z_2\right)}\right)\exp\left\{-i\frac{\omega}{c}\frac{\boldsymbol{\rho}_0\cdot\boldsymbol{\rho}_z}{z_1+z_2}\right\} \quad (2.59)\\
&= C^2\frac{i2\pi c}{\omega}\frac{e^{i\frac{\omega}{c}\left(z_1+z_2\right)-i\omega\left(t_1+t_2\right)}}{z_1+z_2}\int d\boldsymbol{\rho}_0\tilde{A}\left(\boldsymbol{\rho}_0\right)G\left(\boldsymbol{\rho}_z-\boldsymbol{\rho}_0, \frac{\omega}{c\left(z_1+z_2\right)}\right)\\
&= C^2\frac{i2\pi c}{\omega}\frac{e^{i\frac{\omega}{c}z-i\omega t}}{z}\int d\boldsymbol{\rho}_0\tilde{A}\left(\boldsymbol{\rho}_0\right)G\left(\boldsymbol{\rho}_z-\boldsymbol{\rho}_0, \frac{\omega}{cz}\right) \quad (2.60)
\end{aligned}$$

which results from the two-step propagation. Comparing Eq. (2.60) with the result of one-step propagation (Eq. (2.52)), we can find the normalization constant $C = -i\omega/2\pi c$. Therefore, the normalized field propagator for free-space Fresnel diffraction is

$$g\left(\boldsymbol{k};\boldsymbol{\rho}_z,z,t\right) = \frac{-i\omega}{2\pi c}\frac{e^{i\frac{\omega}{c}z}}{z}\int d\boldsymbol{\rho}_0\tilde{A}\left(\boldsymbol{\rho}_0\right)G\left(\boldsymbol{\rho}_z-\boldsymbol{\rho}_0, \frac{\omega}{cz}\right) \tag{2.61}$$

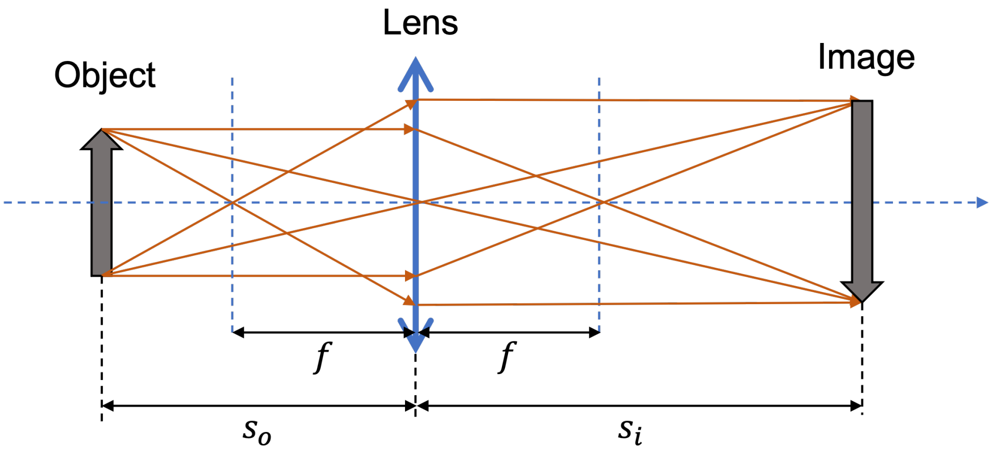

Figure 2.4: Schematic of a classical imaging system without scattering medium. Adapted from Page 54 of Ref. [100].

2.4 A classical optical imaging system without scattering medium

Now, we are ready to analyze a classical optical imaging system without scattering medium [100]. As illustrated in Fig. 2.4 , an object is either illuminated by an external light source or self-luminous. A thin lens is placed at a distance s_o from the object to produce an image of which the location is determined by the Gaussian thin lens equation

$$\frac{1}{s_o} + \frac{1}{s_i} = \frac{1}{f} \tag{2.62}$$

in which s_i is the distance between the lens and the image plane and f is the focal length. As discussed in Section 2.3, the field at the image plane can be expressed by

$$E\left(\boldsymbol{\rho}_i, z_i, t\right) = \int d^3k E\left(\boldsymbol{k}; \boldsymbol{\rho}_o, 0, 0\right) g\left(\boldsymbol{k}; \boldsymbol{\rho}_i, z_i, t\right) \tag{2.63}$$

where $E\left(\boldsymbol{k}; \boldsymbol{\rho}_o, 0, 0\right)$ is the complex amplitude of mode $\boldsymbol{k}$ in the object plane and $g\left(\boldsymbol{k}; \boldsymbol{\rho}_i, z_i, t\right)$ is the field propagator. For the sake of simplicity, we assume that the frequency of the field $\omega = ck$ is constant and only one polarization direction is considered. Based on the experimental setup, the field propagator is found to be

$$\begin{aligned} g\left(\boldsymbol{k};\boldsymbol{\rho}_i,z_i\right) &= g\left(\boldsymbol{k};\boldsymbol{\rho}_i,s_o+s_i\right) \\ &= \int d\boldsymbol{\rho}_o \int d\boldsymbol{\rho}_l \tilde{A}\left(\boldsymbol{\rho}_o\right)\left[\frac{-i\omega}{2\pi c}\frac{e^{i\frac{\omega}{c}s_o}}{s_o}G\left(\boldsymbol{\rho}_l-\boldsymbol{\rho}_o,\frac{\omega}{cs_o}\right)\right] \\ &\quad \times G\left(\boldsymbol{\rho}_l,-\frac{\omega}{cf}\right)\left[\frac{-i\omega}{2\pi c}\frac{e^{i\frac{\omega}{c}s_i}}{s_i}G\left(\boldsymbol{\rho}_i-\boldsymbol{\rho}_l,\frac{\omega}{cs_i}\right)\right] \end{aligned} \tag{2.64}$$

in which $\tilde{A}\left(\boldsymbol{\rho}_o\right)$ is the complex amplitude of the field distribution in the object plane, and $\boldsymbol{\rho}_o$, $\boldsymbol{\rho}_l$ and $\boldsymbol{\rho}_i$ are position vectors in the planes of object, lens, and image, respectively. Using Eq. (2.48) and (2.49), we can obtain

$$\begin{aligned} g\left(\boldsymbol{k};\boldsymbol{\rho}_i,s_o+s_i\right) &= \left(\frac{-i\omega}{2\pi c}\right)^2\frac{e^{i\frac{\omega}{c}(s_o+s_i)}}{s_os_i}G\left(\boldsymbol{\rho}_i,\frac{\omega}{cs_i}\right)\int d\boldsymbol{\rho}_o\tilde{A}\left(\boldsymbol{\rho}_o\right)G\left(\boldsymbol{\rho}_o,\frac{\omega}{cs_o}\right) \\ &\quad \times\int d\boldsymbol{\rho}_l G\left[\boldsymbol{\rho}_l,\frac{\omega}{c}\left(\frac{1}{s_o}+\frac{1}{s_i}-\frac{1}{f}\right)\right]e^{-i\frac{\omega}{c}\left(\frac{\boldsymbol{\rho}_o}{s_o}+\frac{\boldsymbol{\rho}_i}{s_i}\right)\cdot\boldsymbol{\rho}_l} \\ &= \frac{-\omega^2e^{i\frac{\omega}{c}(s_o+s_i)}}{\left(2\pi c\right)^2s_os_i}G\left(\boldsymbol{\rho}_i,\frac{\omega}{cs_i}\right)\int d\boldsymbol{\rho}_o\tilde{A}\left(\boldsymbol{\rho}_o\right)G\left(\boldsymbol{\rho}_o,\frac{\omega}{cs_o}\right)\int d\boldsymbol{\rho}_l e^{-i\frac{\omega}{c}\left(\frac{\boldsymbol{\rho}_o}{s_o}+\frac{\boldsymbol{\rho}_i}{s_i}\right)\cdot\boldsymbol{\rho}_l} \end{aligned} \tag{2.65}$$

where we use Eq. (2.62) to reach the last step. If the radius of the imaging lens R is infinite ($R\to\infty$), it is straightforward to find the last integral to be

$$\int_{-\infty}^{\infty} d\boldsymbol{\rho}_l e^{i\frac{\omega}{c}\left(\frac{\boldsymbol{\rho}_o}{s_o}+\frac{\boldsymbol{\rho}_i}{s_i}\right)\cdot\boldsymbol{\rho}_l} = \delta\left[\frac{\omega}{s_oc}\left(\boldsymbol{\rho}_o+\frac{\boldsymbol{\rho}_i}{m}\right)\right] \tag{2.66}$$

where $m=s_i/s_o$ is the magnification of the imaging system. Eq. (2.66) implies that a perfect point-to-point mapping between the object and its image can be achieved when the size of the lens is infinite. In this case, an image of infinite high resolution is produced. In practice, however, a lens has a finite size, and one can never obtain a perfect point-to-point mapping. For lens with finite radius R, the last integral in Eq. (2.65) can be evaluated using the integral representation of

Bessel function (Appendix B):

$$\begin{aligned}\int d\boldsymbol{\rho}_l e^{i\frac{\omega}{c}\left(\frac{\boldsymbol{\rho}_o}{s_o}+\frac{\boldsymbol{\rho}_i}{s_i}\right)\cdot\boldsymbol{\rho}_l} &= \int_0^R \rho_l d\rho_l \int_0^{2\pi} e^{-i\frac{\omega}{cs_o}\left|\boldsymbol{\rho}_o+\frac{\boldsymbol{\rho}_i}{m}\right|\rho_l\cos\theta} d\theta \\ &= \frac{2\pi R^2 J_1\left(x\right)}{x} \end{aligned} \tag{2.67}$$

with

$$x = \frac{R\omega}{s_o c}\left|\boldsymbol{\rho}_o + \frac{\boldsymbol{\rho}_i}{m}\right|$$

where $J_1\left(x\right)$ is the first-order Bessel function of the first kind. In this case, the point-to-point relationship is degraded to a point-to-spot relationship, and the δ-function is replaced by the well-known point-spread function given by

$$\mathrm{somb}\left(x\right) = \frac{2J_1\left(x\right)}{x} \tag{2.68}$$

2.5 Optical imaging system with scattering medium: a general formulation

As discussed in Section 2.4, for a perfect optical imaging system, any radiation starting from a point on the object plane will impinge at a unique point on the image plane. The point-to-point relationship is a result of constructive-destructive interference and guarantees the formation of a clear image. For a practical imaging system, the point-to-point relationship becomes a point-to-spot relationship. The limitation of the finite size of the imaging lens leads to an incomplete constructive-destructive inference, but an image can still be produced since the relative phase of the fields emitted from any two points on the object is preserved. However, things become completely different when a scattering medium blocks the direct view of the object, as shown in Fig. 2.5. The field from any point source on the object is scattered before it reaches the image plane. The scattering changes the propagation direction of the field and introduces random phases, which randomizes the original point-to-point relationship. Therefore, the image turns to a random pattern.

Here we give a general formulation of imaging through scattering medium. Without the loss of generality, a scattering medium is inserted in between the object and the imaging lens with focal

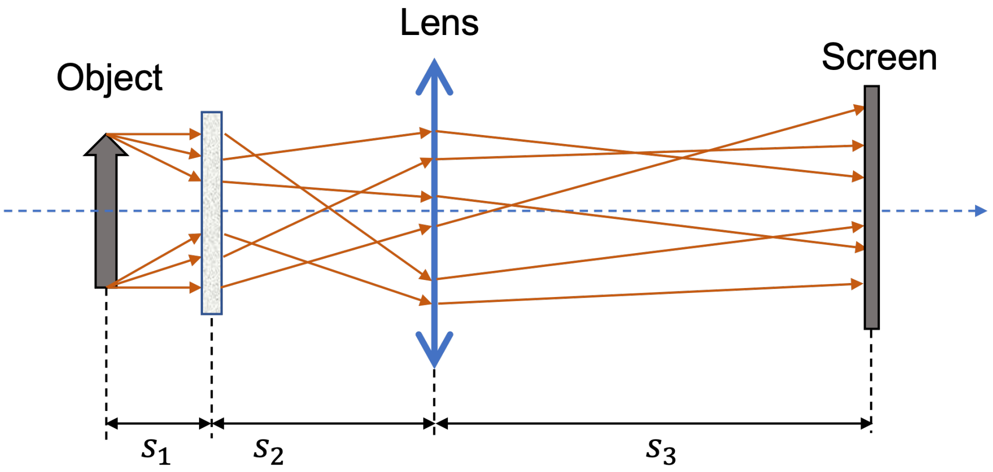

Figure 2.5: Schematic of a classical imaging system with scattering medium.

length f in the simple imaging system shown in Fig. 2.5. The distance s_2 and s_3 satisfies the relation $1/s_2 + 1/s_3 = 1/f$. According to the discussion in Section 2.4, the field propagator of the system can be written as

$$\begin{aligned}
g\left(\boldsymbol{k};\boldsymbol{\rho}_i,z_i\right) = & \left(\frac{-i\omega}{2\pi c}\right)^3 \frac{e^{i\frac{\omega}{c}(s_1+s_2+s_3)}}{s_1 s_2 s_3} \int d\boldsymbol{\rho}_o \int d\boldsymbol{\rho}_m \int d\boldsymbol{\rho}_l \tilde{A}\left(\boldsymbol{\rho}_o\right) G\left(\boldsymbol{\rho}_m - \boldsymbol{\rho}_o, \frac{\omega}{cs_1}\right) \tilde{R}\left(\boldsymbol{\rho}_m\right) \\
& \times G\left(\boldsymbol{\rho}_l - \boldsymbol{\rho}_m, \frac{\omega}{cs_2}\right) G\left(\boldsymbol{\rho}_l, -\frac{\omega}{cf}\right) G\left(\boldsymbol{\rho}_i - \boldsymbol{\rho}_l, \frac{\omega}{cs_3}\right) \\
= & \left(\frac{-i\omega}{2\pi c}\right)^3 \frac{e^{i\frac{\omega}{c}(s_1+s_2+s_3)}}{s_1 s_2 s_3} \int d\boldsymbol{\rho}_o G\left(\boldsymbol{\rho}_o, \frac{\omega}{cs_1}\right) \\
& \times \int d\boldsymbol{\rho}_m R\left(\boldsymbol{\rho}_m\right) G\left[\boldsymbol{\rho}_m, \frac{\omega}{c}\left(\frac{1}{s_1} + \frac{1}{s_2}\right)\right] e^{-i\frac{\omega}{cs_1}\boldsymbol{\rho}_m \cdot \boldsymbol{\rho}_o} \\
& \times \int d\boldsymbol{\rho}_l G\left[\boldsymbol{\rho}_l, \frac{\omega}{c}\left(\frac{1}{s_2} + \frac{1}{s_3} - \frac{1}{f}\right)\right] e^{-i\frac{\omega}{c}\left(\frac{\boldsymbol{\rho}_m}{s_2} + \frac{\boldsymbol{\rho}_i}{s_3}\right) \cdot \boldsymbol{\rho}_l} \\
= & \left(\frac{-i\omega}{2\pi c}\right)^3 \frac{e^{i\frac{\omega}{c}(s_1+s_2+s_3)}}{s_1 s_2 s_3} \int d\boldsymbol{\rho}_o G\left(\boldsymbol{\rho}_o, \frac{\omega}{cs_1}\right) \\
& \times \int d\boldsymbol{\rho}_m R\left(\boldsymbol{\rho}_m\right) G\left[\boldsymbol{\rho}_m, \frac{\omega}{c}\left(\frac{1}{s_1} + \frac{1}{s_2}\right)\right] e^{-i\frac{\omega}{cs_1}\boldsymbol{\rho}_m \cdot \boldsymbol{\rho}_o} \\
& \times \int d\boldsymbol{\rho}_l e^{-i\frac{\omega}{c}\left(\frac{\boldsymbol{\rho}_m}{s_2} + \frac{\boldsymbol{\rho}_i}{s_3}\right) \cdot \boldsymbol{\rho}_l}
\end{aligned} \tag{2.69}$$

where we introduce a complex function

$$\tilde{R}\left(\boldsymbol{\rho}_m\right) = R\left(\boldsymbol{\rho}_m\right) e^{i\varphi\left(\boldsymbol{\rho}_m\right)} \tag{2.70}$$

to describe the amplitude and phase of the scattered field due to the scattering center at position $\boldsymbol{\rho}_m$. In general, $\tilde{R}\left(\boldsymbol{\rho}_m\right)$ does not have a analytical expression and is related to the statistical properties of the scattering centers in the medium, so the integral over $\boldsymbol{\rho}_m$ in Eq. (2.69) cannot be carried out analytically. The random phase factor $e^{i\varphi\left(\boldsymbol{\rho}_m\right)}$ scrambles the relative phase information between any two points in the object plane, resulting in a random pattern in the image plane.

The above example, although being simple, has provided a good illustration of the key idea why it is impossible to obtain an image of the object directly with an optical imaging system: it is the randomization of phase information that prevents the fields from producing a constructive-destructive inference that "reproduces" the object in the image plane.

2.6 Macroscopic characterization of a scattering medium

In practice, scattering media mainly fall into two categories: scattering volume and scattering surface. Biological tissues, fog, and turbid liquid are common scattering volumes. They can usually be modeled as 3D "containers" filled with matters that can absorb and scatter light. Although absorption may add another dimension of challenge for imaging through scattering media, it is beyond our scope, and we will not discuss absorption throughout the rest of this dissertation.

To elucidate the challenges associated with imaging through scattering media, it is essential to understand the way that light propagates in the media. Light traveling through scattering volume mainly falls into three components: ballistic (unscattered) photon, snake photon, and diffuse (scattered) photon [1, 2]. Ballistic photon is not scattered but continues to propagate along its original direction. It preserves all the information of the object as if there is no scattering medium, and thus can produce images of the object with diffraction-limited resolution. The intensity of the ballistic component of incident light is given by

$$I = I_0 e^{-\mu_s l} \tag{2.71}$$

where I_0 is the intensity of the incident light, μ_s is the scattering coefficient of the medium, and l is the propagation distance of the light in the medium. Another quantity directly related to the scattering coefficient μ_s is the mean free path (MFP), which is defined by

$$l_s = \frac{1}{\mu_s} \tag{2.72}$$

It is interpreted as the average distance that a photon can propagate between two successive scattering events. As we can see from Eq. (2.71), the ballistic component is attenuated exponentially as the propagation distance l increases. For many practical media, their thicknesses are much larger than their MFPs, so the transmitted light will be scattered multiple times, and the ballistic signals will be swamped by the scattered component for any significant propagation depth. The domination of scattered light will obscure the camera image of a conventional imaging system.

However, the fact that most scattering media are highly forward-scattering makes it possible for photons to propagate a longer distance without being randomized in their propagation directions. For a scattering distance where no ballistic light can reach, there may be some photons that are only slightly deflected about the ballistic direction. These photons are called “snake photons”, and they carry the information about a relatively well-defined path through the scattering medium. The intensity of snake photon is attenuated according to

$$I = I_0 e^{-\mu_s' l} \tag{2.73}$$

where $\mu_s' = \mu_s (1 - g)$ is the transport scattering coefficient, g is a parameter that defines the degree of forward scattering, and l is the propagation distance. The higher the value of g is, the more forward the scattering is, and the longer the photon can propagate without being randomized in direction. Similar to MFP, the transport mean free path (TMFP) is defined to be

$$l'_s = \frac{1}{\mu'_s} \tag{2.74}$$

which gives the average distance beyond which the propagation direction of photons will be randomized.

The story is different when light reflects off or transmits through a scattering surface [104, 105, 106, 107]. In this case, the scattering surface is modeled as a collection of independent scattering centers located in a section of the light path. The interference between the diffraction lobes originated from different scattering centers will form a far-field pattern consisting of randomly distributed bright and dark areas with irregular sizes and shapes, which is known as "speckle pattern". According to the field propagation theory discussed in Section 2.3, the optical field in the observation plane can be expressed as

$$E(\boldsymbol{R}) = \int E(\boldsymbol{r}) \exp\{i\phi(\boldsymbol{r})\} G(\boldsymbol{R}-\boldsymbol{r})\, d\boldsymbol{r} \tag{2.75}$$

where $\boldsymbol{R}$ and $\boldsymbol{r}$ are the position vectors that define the observation plane and incident plane, respectively. $\phi(\boldsymbol{r})$ describes the random phase modulation introduced by the scattering surface, and $G(\boldsymbol{R}-\boldsymbol{r})$ is the field propagator. In the Fresnel diffraction approximation, the field propagator is given by

$$G(\boldsymbol{R}-\boldsymbol{r}) = \frac{ke^{ikz}}{2\pi iz} \exp\left\{\frac{ik}{2z}|\boldsymbol{R}-\boldsymbol{r}|^2\right\} \tag{2.76}$$

where $k = 2\pi/\lambda$ is the wave number of the field and z is the distance between the observation plane and incident plane. Eq. (2.75) implies that the spatial information conveyed by $E(\boldsymbol{r})$ will be degraded due to the random phase $\phi(\boldsymbol{r})$ introduced by the scattering surface. For rough surface scattering media, such as ground glass diffusers, the phase modulation function $\phi(\boldsymbol{r})$ is further related to the height distribution of the rough surface $h(\boldsymbol{r})$ [108]. For transmitting surfaces, the relation is given by

$$\phi\left(\boldsymbol{r}\right)=k\left(n-1\right)h\left(\boldsymbol{r}\right) \tag{2.77}$$

where n is the refractive index. For reflecting surfaces, the relation is given by

$$\phi\left(\boldsymbol{r}\right)=-2kh\left(\boldsymbol{r}\right)\cos\theta_i \tag{2.78}$$

where θ_i is the incident angle. It follows that the variation of phases $d\phi\left(\boldsymbol{r}\right)/d\boldsymbol{r}$ is proportional to the variation of height $dh\left(\boldsymbol{r}\right)/d\boldsymbol{r}$, so the rougher the surface is, the sharper the variation of phases is.

3. HIGH ORDER COHERENCE FUNCTIONS AND SPECTRAL DISTRIBUTIONS AS GIVEN BY THE SCULLY-LAMB QUANTUM THEORY OF THE LASER*

3.1 Introduction

In this chapter, we present an experiment on the time evolution of the off-diagonal elements of laser density matrix given by the Scully-Lamb quantum theory of laser [109]. This experiment inspires the idea of imaging through scattering media by extracting the beat frequency of two lasers, which we will mainly discuss in Chapter 4 and 5.

Quantum coherence effects in molecular physics are largely based on the existence of the laser [110]. Indeed, in most of our experiments and calculations, we take the laser to be an ideal monochromatic light source. If the laser linewidth is important then we usually just include a "phase diffusion" linewidth into the logic. But what if we are thinking about higher-order correlation effects in an ensemble of coherently driven molecules. For example, photon correlation and light beating spectroscopy involving Glauber second-order correlation functions [111, 112]. Furthermore, third- and higher-order photon correlations of the laser used to drive our molecular system can be important. The investigation of higher-order quantum laser noise is the focus of this chapter [109].

Fifty years ago the Scully-Lamb (SL) quantum theory of the laser (QTL) was developed using a density matrix formalism [113]. In the interesting threshold region [114, 115] the steady-state laser photon statistics is given by the diagonal elements of the laser density matrix $\rho_{nn}\left(t\right) \equiv p\left(n\right)$ as

$$p\left(n\right) = p\left(0\right)\prod_{k=1}^{n}\frac{\left(\mathscr{A}/\mathscr{L}\right)}{1+\frac{\mathscr{B}}{\mathscr{A}}k} \tag{3.1}$$

where $\mathscr{A}$ is the linear gain, $\mathscr{B}$ is the nonlinear saturation coefficient, $\mathscr{L}$ is the cavity loss rate, and $p\left(0\right)$ is the normalization constant determined by $\sum_{n=0}^{\infty} p\left(n\right) = 1$, which can be expressed by

---

*Reprinted with permission from "High order Coherence Functions and Spectral Distributions as given by the Scully-Lamb Quantum Theory of the Laser" by Tao Peng, Xingchen Zhao, Yanhua Shih, and Marlan O. Scully, 2021. ***Frontiers in Physics***, 9, 657333, Copyright 2021 by Creative Commons Attribution License (CC BY).

confluent hypergeometric function [116]

$$p\left(0\right)=\left[\sum_{n=0}^{\infty}\frac{\left(\frac{\mathscr{A}}{\mathscr{B}}\right)!\left(\frac{\mathscr{A}^2}{\mathscr{B}\mathscr{L}}\right)^n}{\left(n+\frac{\mathscr{A}}{\mathscr{B}}\right)!}\right]^{-1}=\left[F\left(1,\frac{\mathscr{A}}{\mathscr{B}}+1,\frac{\mathscr{A}^2}{\mathscr{B}\mathscr{L}}\right)\right]^{-1} \tag{3.2}$$

Eq. (3.1) is plotted in Fig. 3.1 where it is compared with the photon distribution of a coherent state:

$$p\left(n\right)=\frac{\langle n\rangle^n e^{-\langle n\rangle}}{n!} \tag{3.3}$$

The parameters are determined by two conditions: 1. the laser is 20 percent above the threshold

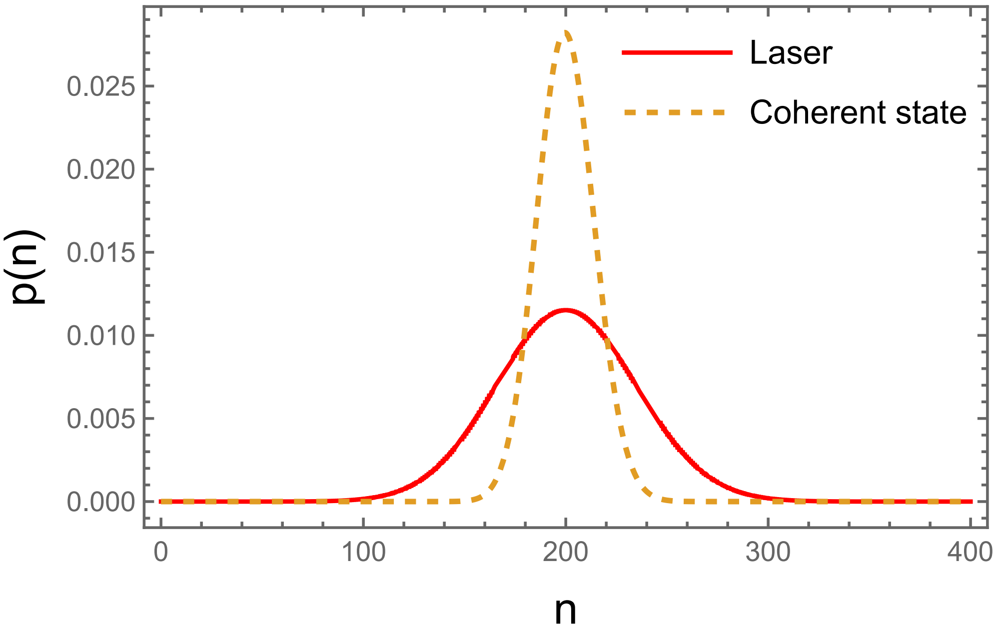

Figure 3.1: Steady state photon distribution function for coherent and laser radiation. The laser is taken to be 20 percent above threshold, and $\langle n\rangle=200$.

$(\mathscr{A}/\mathscr{L}=1.2)$; 2. the average photon number

$$\langle n\rangle=\frac{\mathscr{A}}{\mathscr{L}}\frac{\mathscr{A}-\mathscr{L}}{\mathscr{B}} \tag{3.4}$$

is equal to 200.

The formalism developed in the QTL density matrix analysis has since been successfully applied to many other physical systems such as the single-atom maser [117], the Bose-Einstein condensate (BEC, see Table 3.1) [118], pion physics [119], etc. Other applications of the formalism have been developed recently and more will likely emerge. Thus we are motivated to deeper our understanding of the QTL by further analyzing and experimentally verifying the time dependence of off-diagonal elements $\rho_{n,n+k}(t) \equiv \rho_n^{(k)}(t)$. The diagonal elements of the laser density matrix for which $k = 0$, have been well studied. Not as for the off-diagonal elements. In particular $\rho_n^{(1)}(t)$ yields the Schawlow-Townes laser linewidth. But what about the higher-order correlations $k = 2, 3 \cdots$?

	Laser	BEC
$\mathscr{A}$	Linear stimulated emission gain	Rate of cooling due to interaction with walls times the number of atom N
$\mathscr{B}$	Nonlinear saturation due to the reabsorption of photons generated by stimulated emission	Nonlinearity parameter due to the constraint that there are N atoms in the BEC: numerically equal to $\mathscr{A}/N$.
$\mathscr{L}$	Loss rate due to photons absorbed in cavity mirrors etc.	Loss rate due to photon absorption from the thermal bath (walls) equal to $\mathscr{A}(T/T_c)^3$.

Table 3.1: Correspondence of parameters between laser and BEC systems.

3.2 Theory and Experiments

The time evolution of the off-diagonal elements of laser density matrix has been obtained in Schrödinger picture as [120]

$$\rho_n^{(k)}(t) = \rho_n^{(k)}(0)\, e^{-i\nu t} e^{-k^2 D t} \tag{3.5}$$

where ν is the center frequency of the laser, $D = \gamma/\bar{n}$ is the Schawlow-Townes phase diffusion linewidth, and $\bar{n} = (\alpha - \gamma)/\beta$. For the sake of simplicity, we assume that the electric field of the laser is single-mode and linearly polarized. The field operator can be expressed as the sum of its positive and negative frequency parts

$$\hat{E}\left(z\right) = \hat{E}^{(+)}\left(z\right) + \hat{E}^{(-)}\left(z\right) \tag{3.6}$$

where

$$\hat{E}^{(+)}\left(z\right) = \mathscr{E}_0 \hat{a} e^{i\kappa z} \tag{3.7}$$

$$\hat{E}^{(-)}\left(z\right) = \mathscr{E}_0 \hat{a}^{\dagger} e^{-i\kappa z} \tag{3.8}$$

in which κ are the center frequency and the wavenumber of the laser field, respectively. $\hat{a}$ and $\hat{a}^{\dagger}$ are the annihilation and creation operator in the Schrödinger picture and obey $\left[\hat{a}, \hat{a}^{\dagger}\right] = 1$. The electric field per photon is given by $\mathscr{E}_0 = \sqrt{\hbar\nu/\epsilon_0 V}$, where ϵ_0 is the permittivity of free space and V is the laser cavity volume. One way to calculate the spectrum of the laser is based on Wiener-Khinchin theorem, which implies that the first order correlation function of the laser field $G^{(1)}\left(\tau\right)$ forms a Fourier transform pair with the power spectrum of the field $S\left(\omega\right)$:

$$S\left(\omega\right) = \frac{1}{\pi}\Re \int_0^{\infty} d\tau G^{(1)}\left(\tau\right) e^{i\omega\tau} \tag{3.9}$$

in which $\Re$ stands for taking the real part, and the first order correlation function of the field is given by

$$\begin{aligned} G^{(1)}\left(\tau\right) &= \left\langle \hat{E}^{(-)}\left(t\right) \hat{E}^{(+)}\left(t+\tau\right) \right\rangle \\ &= \mathrm{Tr}_{FR}\left\{ \hat{E}^{(-)}\left(t\right) \hat{E}^{(+)}\left(t+\tau\right) \hat{\rho}_{FR}\left(0\right) \right\} \end{aligned} \tag{3.10}$$

where $\hat{E}^{(+)}\left(t\right)$ is the electric field operator at time t, and $\hat{\rho}_{FR}\left(0\right)$ is the density operator of the field-reservoir system at $t = 0$. However, there are two difficulties with this approach [121]. First, calculating spectrum from correlation function is a procedure in classical signal processing theory, which must be properly transferred to quantum-mechanical form before solving problems of a quantized field. Second, the time dependence of the electric field have not been defined. A remedy of this approach is given by the quantum regression theorem [121] (See Appendix C for more details), which allows to calculate the two-time correlation function $\left\langle \hat{E}^{(-)}(t)\,\hat{E}^{(+)}(t+\tau)\right\rangle$ from the single-time expectation value $\left\langle \hat{E}^{(-)}(t)\right\rangle$.

The spectrum of the laser can also be deduced from the beat signal of two independent lasers, which also avoids the difficulty of calculating the two-time correlation function. Here we first list the relation between the expectation values of the electric field and the off-diagonal elements of the laser density matrix $\rho_n^{(k)}(0)$. Later, we will use these relations to calculate the high-order coherence functions associated with our experiments . The expectation value of the electric field amplitude operator is given by

$$
\begin{aligned}
\left\langle \hat{E}^{(-)}(z,t)\right\rangle &= \mathrm{Tr}\left\{\hat{\rho}(t)\,\mathscr{E}_0\hat{a}^{\dagger}e^{i\kappa z}\right\} \\
&= \mathscr{E}_0 e^{i\kappa z}\sum_n \left\langle n\left|\hat{\rho}(t)\,\hat{a}^{\dagger}\right|n\right\rangle \\
&= \mathscr{E}_0 e^{i\kappa z}\sum_n \sqrt{n+1}\left\langle n\left|\hat{\rho}(t)\right|n+1\right\rangle \\
&= \mathscr{E}_0 e^{i\kappa z}\sum_n \sqrt{n+1}\rho_n^{(1)}(0)\,e^{-Dt}e^{-i\nu t}
\end{aligned}
\tag{3.11}
$$

which is related to the first order off-diagonal elements $\rho_n^{(1)}(0)$. It follows As is discussed in the following, the second-order off-diagonal elements are given by the field operator averages

$$
\begin{aligned}
\left\langle \hat{E}^{(-)}(z,t)\,\hat{E}^{(-)}(z,t)\right\rangle &= \mathrm{Tr}\left\{\hat{\rho}(t)\,\mathscr{E}_0^2\left(\hat{a}^{\dagger}\right)^2 e^{i2\kappa z}\right\} \\
&= \mathscr{E}_0^2 e^{i2\kappa z}\sum_n \left\langle n\left|\hat{\rho}(t)\left(\hat{a}^{\dagger}\right)^2\right|n\right\rangle \\
&= \mathscr{E}_0^2 e^{i2\kappa z}\sum_n \sqrt{(n+2)(n+1)}\rho_n^{(2)}(0)\,e^{-4Dt}e^{-i2\nu t}
\end{aligned}
\tag{3.12}
$$

and the third-order off-diagonal elements are given by

$$\begin{aligned}\left\langle \hat{E}^{(-)}(z,t)\,\hat{E}^{(-)}(z,t)\,\hat{E}^{(-)}(z,t)\right\rangle &= \mathrm{Tr}\left\{\hat{\rho}(t)\,\mathscr{E}_0^3\left(\hat{a}^{\dagger}\right)^3 e^{i3\kappa z}\right\}\\ &= \mathscr{E}_0^3 e^{i3\kappa z}\sum_n \left\langle n\left|\hat{\rho}(t)\left(\hat{a}^{\dagger}\right)^3\right|n\right\rangle\\ &= \mathscr{E}_0^3 e^{i3\kappa z}\sum_n \sqrt{(n+3)(n+2)(n+1)}\rho_n^{(3)}(0)\,e^{-9Dt}e^{-i3\nu t}\end{aligned} \tag{3.13}$$

Eq. (3.11) gives the time evolution associated with the first order off-diagonal elements $\rho_n^{(1)}$, yielding the spectral profile of the laser. Eq. (3.12) and Eq. (3.13) will give the second- and third-order spectral profile that is determined by the off-diagonal elements $\rho_n^{(2)}$ and $\rho_n^{(3)}$.

The heterodyne method is usually adapted to measure the linewidth of the laser [122, 123], in which case the center frequency is shifted from optical frequency to the radio frequency range. A natural way to measure the laser linewidth is to beat two almost identical but uncorrelated lasers [124] such that the beat frequency between the lasers is in the MHz range. The result, as seen from Eq. (3.17), is twice the laser linewidth when the two independent lasers are nearly identical. Many experiments have been carried out to determine the linewidth [122] and photon statistics [125] of the laser. Other experiments have measured the intensity correlation of the laser at threshold [126], revealing the influence of the intensity fluctuation on the laser spectrum. However, to the best of our knowledge, no measurements have been made of the higher-order phase correlations ($k \geq 2$). Here we measure the second and third correlation of the heterodyne signals from two independent lasers, which yields the second and third-order time evolution of a laser above threshold. Specifically, we performed the following experiments: the first set of experiments is to measure the spectral profile of the laser beat note, i.e., allows us to measure the decay rate as shown in Eq. (3.11). The other two sets of experiments determine the spectral profile of the second and third-order correlated beat notes, this allows us to measure the decay rate as shown in Eq. (3.12) and Eq. (3.13).

Fig. 3.2 illustrates the setup of the first set of experiments. This is a typical heterodyne detection setup, the center frequency between the two He-Ne lasers is in the MHz range. This difference

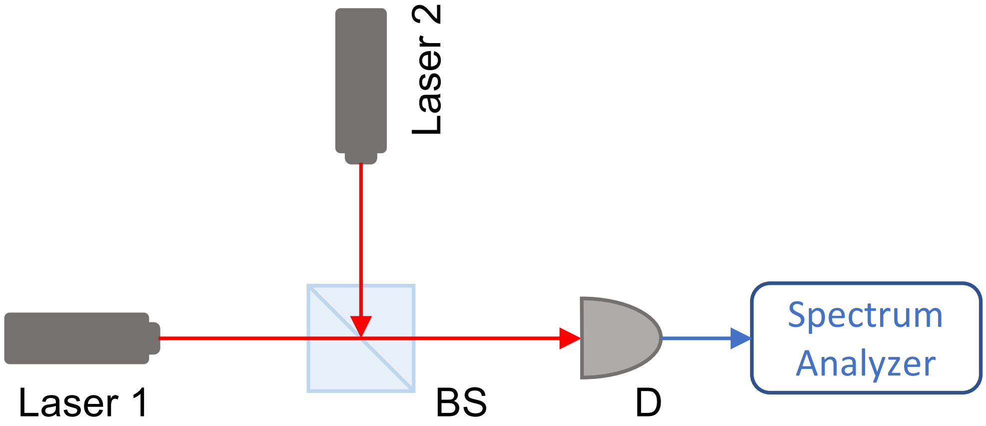

Figure 3.2: Experimental setup for measuring the spectrum of the beat note between lasers 1 and 2. The beat note signal is measured by the detector (D) and analyzed by the spectrum analyzer. BS: non-polarizing beamsplitter.

allows us to analyze the beat signal around a non-zero value hence the full shape of the linewidth is obtained unambiguously. A non-polarizing beamsplitter (BS) is used to mix the two laser beams. The beat signal is then directed to the photodiode (D) after the BS. A fast Fourier transform (FFT) of the signal is performed by the spectrum analyzer (SA), giving the spectrum of the beat note.

For the first set of experiments, the first-order coherence function [112, 113] is

$$\begin{aligned} G^{(1)}(t) &= \mathrm{Tr}\left\{\hat{\rho}(t)\left[\hat{E}_1^{(-)}(t)+\hat{E}_2^{(-)}(t)\right]\left[\hat{E}_1^{(+)}(t)+\hat{E}_2^{(+)}(t)\right]\right\} \\ &= \mathrm{Tr}\left\{\left(\hat{\rho}_1(t)\otimes\hat{\rho}_2(t)\right)\left(\left|\hat{E}_1(0)\right|^2+\left|\hat{E}_2(0)\right|^2+\hat{E}_1^{(-)}(0)\,\hat{E}_1^{(+)}(0)+\text{c.c.}\right)\right\} \\ &= \mathscr{E}_1^2\mathrm{Tr}\left\{\hat{\rho}_1(t)\,\hat{a}_1^\dagger\hat{a}_1\right\}+\mathscr{E}_2^2\mathrm{Tr}\left\{\hat{\rho}_2(t)\,\hat{a}_2^\dagger\hat{a}_2\right\}+\mathscr{E}_1\mathscr{E}_2\mathrm{Tr}\left[\left(\hat{\rho}_1(t)\otimes\hat{\rho}_2(t)\right)\hat{a}_1^\dagger\hat{a}_2+\text{c.c.}\right] \end{aligned} \tag{3.14}$$

where $\hat{\rho}(t)=\hat{\rho}_1(t)\otimes\hat{\rho}_2(t)$ is the density operator of the system, $\hat{\rho}_1(t)$ and $\hat{\rho}_2(t)$ represent the density operators of laser 1 and 2, ν_1 and ν_2 represent the center frequencies of the lasers 1 and 2, respectively. From the above equation, we can see the only terms that carry the beat note frequency is

$$\Gamma^{(1)}(t)=\mathscr{E}_1\mathscr{E}_2\mathrm{Tr}\left[\left(\hat{\rho}_1(t)\otimes\hat{\rho}_2(t)\right)\hat{a}_1^\dagger\hat{a}_2\right] \tag{3.15}$$

and its complex conjugate which contributes to the negative frequency component. Under the condition that the two lasers are independent, Eq.(3.15) can be further calculated using Eq. (3.11)

$$\begin{aligned}
\Gamma^{(1)}(t) &= \mathscr{E}_1\mathscr{E}_2 \mathrm{Tr}\left[\left(\hat{\rho}_1(t)\otimes\hat{\rho}_2(t)\right)\hat{a}_1^\dagger\hat{a}_2\right] \\
&= \mathscr{E}_1\mathscr{E}_2 \mathrm{Tr}\left[\hat{\rho}_1(t)\hat{a}_1^\dagger\right]\mathrm{Tr}\left[\hat{\rho}_2(t)\hat{a}_2\right] \\
&= \mathscr{E}_1\mathscr{E}_2 \sum_{n_1}\sqrt{n_1+1}\rho_{n_1}^{(1)}(0)\,e^{-D_1t-i\nu_1 t}\sum_{n_2}\sqrt{n_2}\rho_{n_2}^{(-1)}(0)\,e^{-D_2t}e^{i\nu_2 t} \\
&= \mathscr{E}_1\mathscr{E}_2 \sum_{n_1}\sqrt{n_1+1}\rho_{n_1}^{(1)}(0)\sum_{n_2}\sqrt{n_2}\rho_{n_2}^{(-1)}(0)\,e^{-D't}e^{i\nu_0 t} \qquad (3.16)
\end{aligned}$$

where $\nu_0 = \nu_2 - \nu_1$ is the beat frequency of the two lasers and $D' = D_1 + D_2$. Using Eq. (3.9), we can find the power spectrum of the laser

$$\begin{aligned}
S^{(1)}(\omega) &= \Re\left\{\int_0^\infty \Gamma^{(1)}(t)\,e^{-i\omega t}dt\right\} \\
&\propto \frac{D'}{D'^2 + (\omega-\nu_0)^2} \qquad (3.17)
\end{aligned}$$

which is a Lorentzian spectrum centered at the beat frequency ν_0 with a linewidth D' that is essentially twice the width of one laser.

The second and third experiments measure the spectral profile of the second- and third-order correlation of beat notes, the setup is shown in Fig. 3.3. We used the same two lasers to create the beat signal, where three detectors PD$_i$ ($i = 1, 2, 3$) are used. The outputs from the photodiodes are used as inputs for a frequency mixer. The output from the mixer is then sent to the spectrum analyzer and the frequency spectrum of the correlated signal is obtained after the FFT. As shown in Fig. 3.3, this set of experiments measures the laser field correlation that is governed by the time evolution of the second and third-order off-diagonal elements $\rho_n^{(2)}(t)$ and $\rho_n^{(3)}(t)$, respectively. The quantity we now measure is determined by the correlation of the heterodyne signals from detectors as in Fig. 3.3. The correlated heterodyne signal at frequency $2\nu_0$ from the second-order coherence

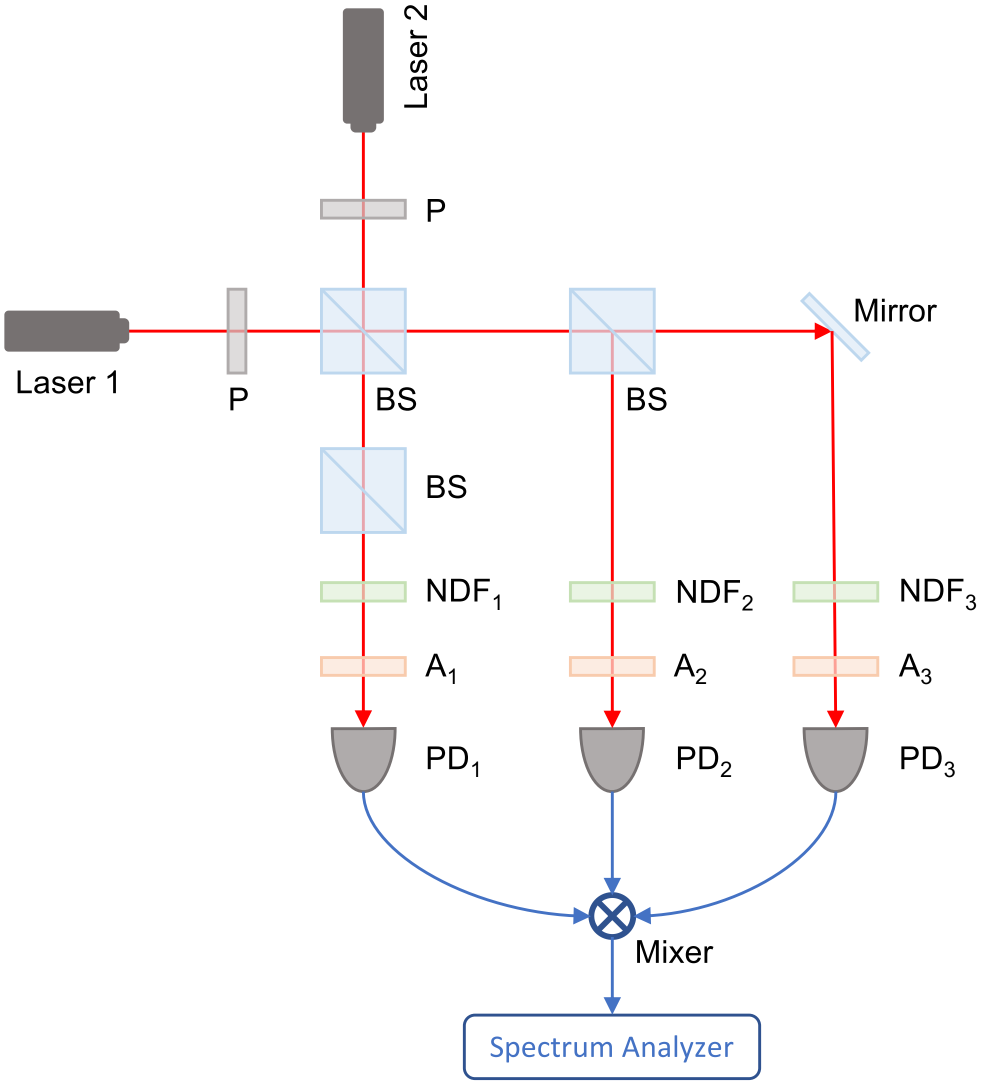

Figure 3.3: Experimental setup for measuring spectral line distribution up to the third order. Laser 1 and 2 : He-Ne lasers; P: polarizer; NDF: neutral-density filter; A: analyzer; BS: non-polarizing beam splitter; Mixer: frequency mixer; PD: photodiode detectors. The bandwidths of the detectors are 50 MHz, the resolution bandwidth of the spectrum analyzer is 10 kHz.

function is given by

$$
\begin{align}
\Gamma^{(2)}(t) &= \mathscr{E}_1\mathscr{E}_2 \mathrm{Tr}\left[\left(\hat{\rho}_1(t)\otimes\hat{\rho}_2(t)\right)\hat{a}_1^\dagger\hat{a}_1^\dagger\hat{a}_2\hat{a}_2\right] \notag\\
&= \mathscr{E}_1\mathscr{E}_2 \mathrm{Tr}\left[\hat{\rho}_1(t)\,\hat{a}_1^\dagger\hat{a}_1^\dagger\right]\mathrm{Tr}\left[\hat{\rho}_2(t)\,\hat{a}_2\hat{a}_2\right] \notag\\
&= \mathscr{E}_1\mathscr{E}_2\sum_{n_1}\sqrt{(n_1+2)(n_1+1)}\rho_{n_1}^{(2)}(0)\,e^{-4D_1t-i2\nu_1t} \notag\\
&\times\sum_{n_2}\sqrt{(n_2-1)\,n_2}\rho_{n_2}^{(-2)}(0)\,e^{-4D_2t}e^{i2\nu_2t} \notag\\
&= \mathscr{E}_1\mathscr{E}_2\sum_{n_1}\sqrt{(n_1+2)(n_1+1)}\rho_{n_1}^{(2)}(0) \notag\\
&\times\sum_{n_2}\sqrt{(n_2-1)\,n_2}\rho_{n_2}^{(-2)}(0)\,e^{-4D't}e^{i2\nu_0t} \tag{3.18}
\end{align}
$$

Taking the Fourier transform as defined by Eq. (3.9), we get a Lorentzian spectral profile centered at $2\nu_0$ with a width of $4D'$

$$
S^{(2)}(\omega)\propto\frac{4D'}{(4D')^2+(\omega-2\nu_0)^2} \tag{3.19}
$$

Similarly, The correlated heterodyne signal at frequency $3\nu_0$ from the third-order coherence function is found to be

$$
\begin{align}
\Gamma^{(3)}(t) &= \mathscr{E}_1^3\mathscr{E}_2^3 \mathrm{Tr}\left[\left(\hat{\rho}_1(t)\otimes\hat{\rho}_2(t)\right)\hat{a}_1^\dagger\hat{a}_1^\dagger\hat{a}_1^\dagger\hat{a}_2\hat{a}_2\hat{a}_2\right] \notag\\
&= \mathscr{E}_1\mathscr{E}_2 \mathrm{Tr}\left[\hat{\rho}_1(t)\,\hat{a}_1^\dagger\hat{a}_1^\dagger\hat{a}_1^\dagger\right]\mathrm{Tr}\left[\hat{\rho}_2(t)\,\hat{a}_2\hat{a}_2\hat{a}_2\right] \tag{3.20}\\
&= \mathscr{E}_1^3\mathscr{E}_2^3\sum_{n_1}\sqrt{(n_1+3)(n_1+2)(n_1+1)}\rho_{n_1}^{(3)}(0) \notag\\
&\times\sum_{n_2}\sqrt{(n_2-2)(n_2-1)\,n_2}\rho_{n_2}^{(-3)}(0)\,e^{-9D't}e^{i3\nu_0t} \tag{3.21}
\end{align}
$$

Therefore, we get a Lorentzian spectral profile centered at $3\nu_0$ with a width of $9D'$

$$
S^{(3)}(\omega)\propto\frac{9D'}{(9D')^2+(\omega-3\nu_0)^2} \tag{3.22}
$$

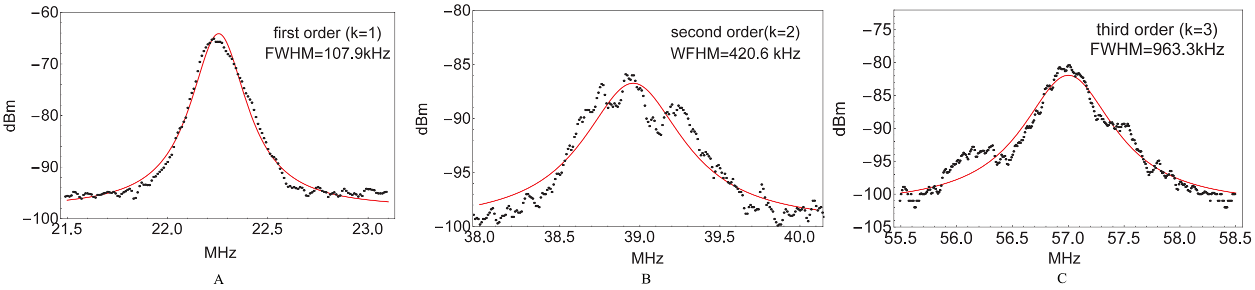

Figure 3.4: Spectral line profiles for up to the third order. The black dots are experimental data, and the red curves are theory. (A) The beat signals from PD1, where the FWHM is 107.9 kHz with average 50 times; (B) Correlated signal from PD2 and PD3, where the FWHM bandwidth is 420.6 kHz with average 50 times; (C) Correlated signal from PD1, PD2, and PD3, where the FWHM is 963.3 kHz with average 50 times.

The main experimental results are shown in Fig. 3.4. All measurements were taken with the laser operating at the same average output power level. The resolution bandwidth (RBW) of the SA is 10 kHz, video bandwidth (VBW) is 30 kHz in all the measurements. For the sake of simplicity, the Full width at half maximum (FWHM) linewidth is taken at the -3 dB width of the measured spectrum by considering only the Lorentzian fitting [124]. Fig. 3.4(A) represents the data of the first set of experiments with an average of 50 measurements of beat note signal from PD_1. The theoretical fitting in the red solid line is based on Eq. (3.17), and the FWHM is 107.9 kHz. Fig. 3.4(B) represents the data of the second set of experiments with 50 measurements of correlated beat note signals from PD_1 and PD_2. The theoretical fitting in the red solid line is based on Eq. (3.19), and the FWHM is estimated to be 420.6 kHz. Fig. 3.4(C) represents the data of the third-order experiments with 50 measurements from all three detectors. The theoretical fitting in the red solid line is based on Eq. (3.22), and the FWHM is estimated to be 963.3 kHz,. First of all, we see that the obtained linewidth from the second-order correlation spectrum is essentially 4 times wider than that of the single beat note linewidth, as well as the third-order spectrum is 9 times wider than that of the single beat note linewidth, validating our theoretical expectation. Secondly, we see that the theoretical curves fit the data well in the center peak, but not well at the tails. This is mainly due to the influences from other noises that also contribute to the spectral profile. For the same reason, we see that the single beat note signal can be better fitted than the second- and third-order correlation signals. There are some small peaks in the higher-order measurements, due to our remeasured higher-order spectral signal is close to the noise level of the detection system. Ideally, more averaging ($\gg 50$) should be able to smooth out these peaks. However, we note here that, there is a trade-off between time averaging and the accurate measurement of the center beat note frequency, due to the drifting of center frequencies of the two lasers. Further using an intense local oscillator and sensitive detection system (detector and spectral analyzer) should be able to solve this issue. Nevertheless, our data confirms the Lorentzian spectral profile of the signal and the time evolution described by Eq. (3.5), in the case of $k = 1$, $k = 2$, and $k = 3$.

3.3 Conclusion

In conclusion, we have studied the time evolution of the higher degrees of off-diagonality obtained by the Scully-Lamb theory of the laser. We particularly measured the bandwidth of the laser beat note and the bandwidth of the correlated laser beat note, which reveal the evolution of the first, second, and third-order off-diagonal elements of the laser density operator. The higher-order spectra reveal the influence of the randomness in the phase of the laser field due to quantum fluctuation. Experimental results agreed with the SL QTL showing that the bandwidth of the third-order and second-order spectral profile are 9 times and 4 times wider than that of the first-order spectral profile, respectively.

4. NON-INVASIVE IMAGING OF OBJECT BEHIND SCATTERING MEDIA VIA CROSS-SPECTRUM

4.1 Introduction

As mentioned in Section 3.2, heterodyne detection of the beat signal of two independent lasers allows the direct measurement of optical information by an electronic device, since the frequency of interest is shifted from optical frequency to radiofrequency. The beat note of two lasers thus can be used as a "feature" to label the optical signal, and the detection of this feature may provide a new method to image an object through scattering media.

Enlightened by the light beating measurement performed in Section 3.2, we propose an experiment to image the structure inside a piece of tissue, as illustrated in Fig. 4.1. In biological tissue, if there are some semi-transparent structures of which the orientation happens to make the output laser beams overlap with each other, the setup may be able to determine the position of these structures. By scanning the whole tissue pixel by pixel and measure the amplitude of the beat frequency for each pixel, one can generate a heat map of the amplitudes, which will show an image of the semi-transparent structures. To verify if this method works, we must first answer two questions: Can we retrieve the beat note of two lasers in the presence of scattering media? If the beat note can be retrieved, can we use it to image an object through scattering media?

4.2 Imaging through scattering media with the beat signal of two lasers

To answer the first question, we performed an experiment as shown in Fig. 4.2. Two He-Ne lasers (633 nm) of nearly identical frequencies are split into two arms to produce a beat signal. The beamsplitter (BS) is surrounded by four cuvettes containing scattering media (mixture of silica power and water) to mimic the scattering condition in tissues. The transmitted light are measured by two photodetectors, and the data is sent to a computer for calculating the normalized correlation

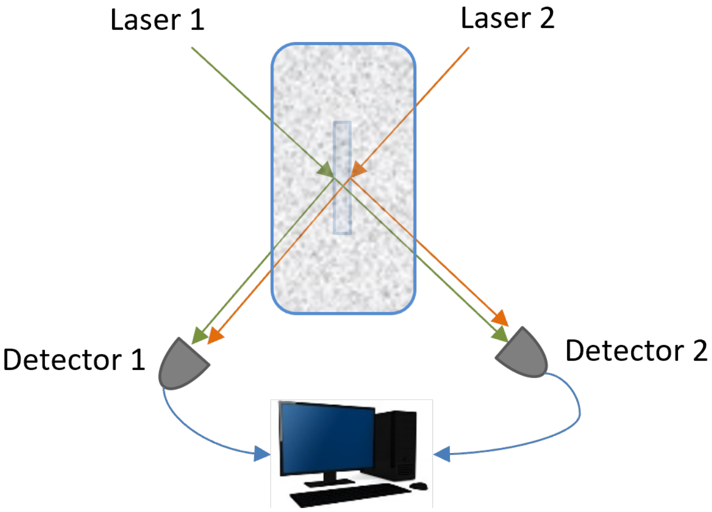

Figure 4.1: An illustration for the idea of locating a semi-transparent object embedded in scattering media by measuring the beat note of two lasers. The two lasers are almost identical but uncorrelated. The data collected by the two detectors are sent to a computer for calculating the two-time correlation function of the two signals.

of the intensity fluctuations defined by

$$C_{\text{norm}}\left(\tau\right)=\frac{\left\langle \Delta I_A\left(t\right)\Delta I_B\left(t+\tau\right)\right\rangle_t}{\sqrt{\left\langle\left(\Delta I_A\left(t\right)\right)^2\right\rangle_t\left\langle\left(\Delta I_B\left(t\right)\right)^2\right\rangle_t}} \tag{4.1}$$

in which $\Delta I\left(t\right)=I\left(t\right)-\left\langle\Delta I\left(t\right)\right\rangle_t$, τ is the time delay, and the average $\left\langle\right\rangle_t$ is taken over time. As shown in Fig. 4.3 (a), two well-defined beat signal are measured directly by the photodetectors without scattering media. The beat signal is overwhelmed by random noise once the BS is hidden behind the scattering media (Fig. 4.3(b)). However, the beat signal can be retrieved in the correlation defined by Eq. (4.1). This indicates that time-domain correlation is immune to the scattering events, and the input optical information can be retrieved by calculating the correlation.

Now, we have confirmed that the beat signal of two lasers can be retrieved through scattering media. To answer the second question, we developed another experimental setup as shown in Fig. 4.4. We first overlap two independent laser beams to generate a beam containing the beat signal. Then, the beam is shined on an object hidden in between two cuvettes with the same

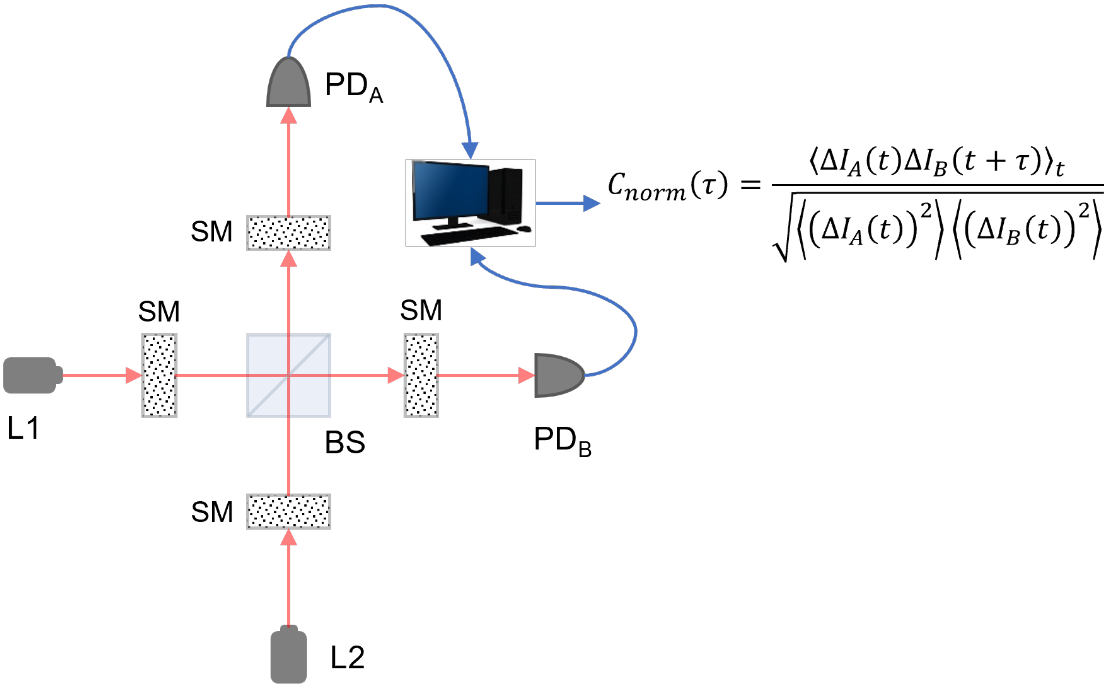

Figure 4.2: Schematic of the experimental setup for retrieving light beating signal via cross-correlation. Two He-Ne lasers (633 nm) of nearly identical frequencies are split into two arms to produce a beat signal. The BS is surrounded by scattering media (mixture of silica power and water) to mimic the scattering condition in tissues. The transmitted light intensities are measured and sent to a computer for processing. L: laser; SM: scattering media; BS: beam splitter; PD: photodetector.

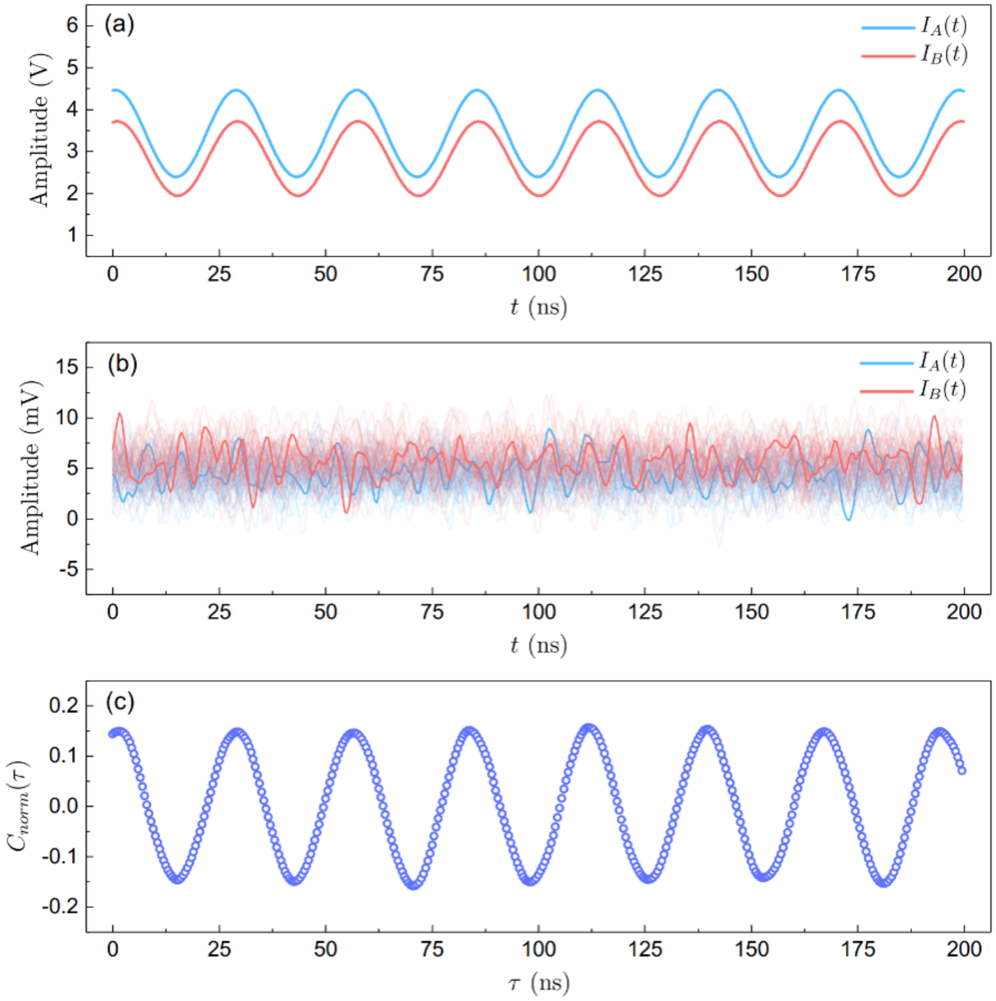

Figure 4.3: Experimental demonstration of retrieving light beating signal via cross-correlation. (a) Clear beat signal can be observed for both arms without scattering media. (b) Beat signal is overwhelmed by random noise in the presence of scattering media. A single measurement of laser intensity (solid colors) is shown for each arm together with other 49 measurements (semi-transparent colors) as a guide of eye to show the randomness of the signals. (c) Normalized temporal cross-correlation of intensity fluctuations which indicates beat signal can be retrieved from signals with random noise.

scattering media as in the previous experiment. The object is a home-made opaque plate with two transparent slits, and its position can be scanned by a motorized translational stage. The transmitted light is split by a BS and measured by two photodetectors for each position of scan x. The data is sent to a computer for processing. Since calculating the time-domain correlation defined by Eq. (4.1) is computationally expensive, we switch to the frequency domain to perform the computation. Analogous to the convolution theorem, the cross-correlation of the two arms of transmitted signal satisfies

$$\mathcal{F}_\tau \left\{ C\left(x;\tau\right) \right\} = \mathcal{F}_t \left\{ I_A\left(x;t\right) \right\} \mathcal{F}_t \left\{ I_A\left(x;t\right) \right\} \tag{4.2}$$

where $\mathcal{F}_v$ denotes Fourier transform with respect to variable v. Note that

$$\Gamma\left(x;\omega\right) \equiv \mathcal{F}_\tau \left\{ C\left(x;\tau\right) \right\} = \int_{-\infty}^{\infty} d\tau C\left(x;\tau\right) e^{-i\omega\tau}, \tag{4.3}$$

we are essentially calculating the cross-spectrum of the two signals [127]. Finally, we plot the cross-spectral amplitude at the beat frequency f_B for every position x, i.e., $\Gamma\left(x;\omega = 2\pi f_B\right)$, and expect an image of the two slits. The results are shown in Fig. 4.5. The Fourier transform of the measured signals give no information of the beat frequency (Fig. 4.5(a)), and no image of the object can be reconstructed from a single spectrum of the signal in arm A (Fig. 4.5(c)). In contrast, the cross-spectrum of the two signals shows a peak at the beat frequency, and an image of the two slits can be reconstructed by plotting the function $\Gamma\left(x;\omega = 2\pi f_B\right)$.

Although the beat signal of two lasers has been demonstrated successful in imaging an object through scattering media, there are some drawbacks that will restrict its application in practice. First, it requires the precise alignment of two lasers for a given orientation of the BS. Second, any small displacement or rotation of the BS will destroy the beat signal. Third, the beat frequency is not stable due to the drift of the laser frequencies, making it difficult to target a single frequency value for the image reconstruction. One may note that the key point of this imaging technique is to embed a "characteristic frequency" in the input optical signal and extract this "feature" in the transmitted signal. A laser of which the intensity is modulated by a sinusoidal driving signal at a certain frequency can meet this requirement. Furthermore, using an intensity-modulated laser removes the requirement of precise alignment of two laser sources, and the modulation frequency can be very stable with modern optical modulators (months under laboratory conditions).

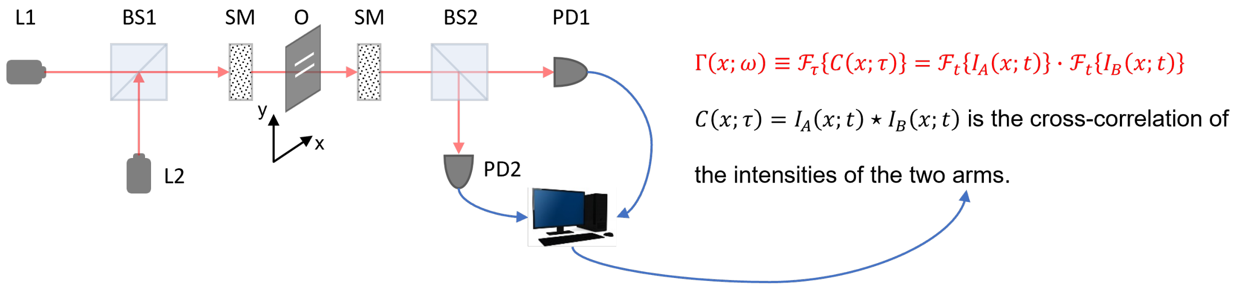

$\Gamma(x;\omega) \equiv \mathcal{F}_\tau\{C(x;\tau)\} = \mathcal{F}_t\{I_A(x;t)\} \cdot \mathcal{F}_t\{I_B(x;t)\}$

$C(x;\tau) = I_A(x;t) \star I_B(x;t)$ is the cross-correlation of the intensities of the two arms.

Figure 4.4: Schematic of the experimental setup for imaging a double slit through scattering media. Two He-Ne lasers (633 nm) are first combined to one beam that carries the beat frequency, and then shined on a transparent object (double slits) hidden in between two cuvettes containing a mixture of silica power and water. The transmitted light are split into two arms and measured by two photodetectors, respectively. The data are processed by a computer to generate an image of the object. L: laser; BS: beam splitter; SM: scattering media; O: object; PD: photodetector.

4.3 Imaging through scattering media with the beat signal of two lasers

In this section, we show a method based on the cross-spectrum measurement from two single-pixel detectors with an intensity-modulated CW laser. The cross-spectrum technique has been mainly used to analyze the cross-correlation between two time series in the frequency domain, and detect weak signal in noisy environment [128, 129, 130]. A CW laser with intensity modulation is commonly used in diffuse optical imaging to study the optical properties of living tissue [131, 132, 132]. We adopt these techniques to demonstrate a non-invasive and easy-to-implement scheme, by which the image of an object can be reconstructed not only through both static and dynamic diffusers but also under an extremely noisy environment, i.e., the light intensity is much lower than detector noise. Besides, the use of CW laser makes the method more favorable in applications involving living tissues.

The experimental setup is shown in Fig. 4.6. A CW laser (633 nm, QPhotonics, QFBGLD-

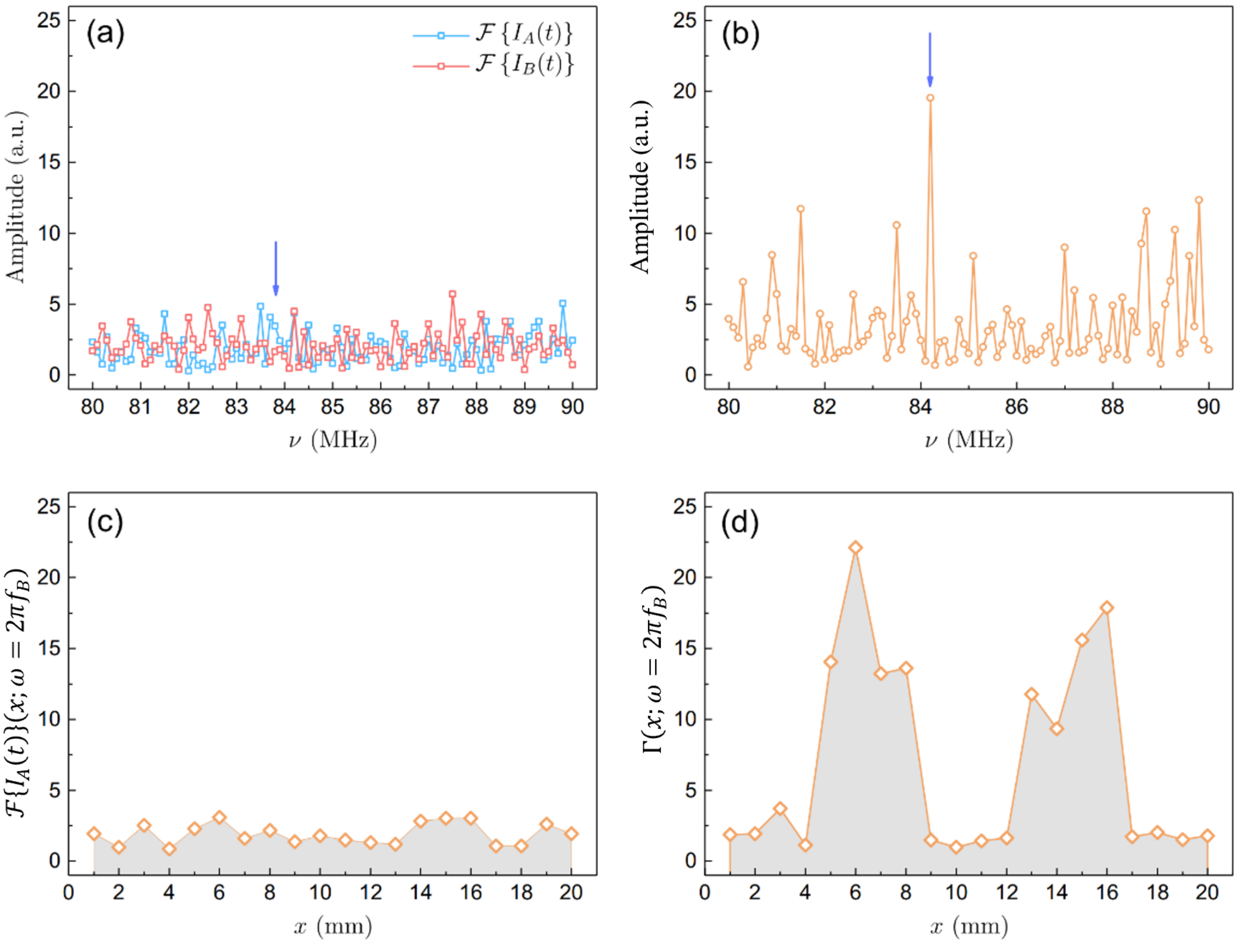

Figure 4.5: Experimental demonstration of imaging a double slit through scattering media. (a) Beat frequency cannot be distinguished in the Fourier spectrum of both arms in the presence of scattering media when the scanning spot is on one of the slits. (b) Beat frequency can be observed in the cross-spectrum under the same condition as in (a). (c) The average intensity is not able to produce an image of the object. (d) The cross-spectrum can show the position of the double slits.

633-30PM) is intensity-modulated by an electro-optic modulator (EOM: Thorlabs, EO-AM-NR-C1) at frequency $f_{mod} = 1$ MHz. The modulation frequency serves as a "feature" that can be extracted later from the output light to accomplish the goal of image reconstruction. The narrow bandwidth associated with the modulated center frequency also allows circumventing the G-R noise in the detection. An objective lens (L1: Nikon, plan fluor, 10X/0.30, ∞/0, WD 17.5) is used to focus the modulated light onto the object plate (O: Thorlabs, R3L1S4N resolution test target) where the letter "1X" is transparent (height: ~ 2.3 mm; width: ~ 3.3 mm; width of transparent region: ~ 0.36 mm). The object plate is sandwiched in situ between a pair of ground glass diffusers (GGDs: Thorlabs, DG10-220) of 220 grit (average grit diameter $\bar{d}_{grit} = 53$ μm). The GGD serves as the scattering medium in our experiment, as widely used in a variety of imaging scenarios [133, 134, 135, 62]. The focal spot is ~ 2.7 μm in size without the GGD and is estimated to be ~ 25 μm when GGD1 is present. A second lens (L2: $f = 150$ mm) is placed behind GDD2 to collect the scattered light. The distance between the object and each diffuser is ~ 5 mm (we note here that the distance cannot be too small due to the shower-curtain effect [136]). The GGDs can be either kept static or moved back and forth together by a motorized stage. The output light is split into two arms by a beam splitter (BS), which are then measured by two photodetectors (PDs: Thorlabs, PDA 10A) respectively, where the two PDs are put at the focal plane of the lens. The data is then sent to a computer to generate images of the object. The object is scanned pixel-by-pixel with an appropriate step size to resolve the region of interest. We note here that, due to the low incident laser power (~ 2 μW) and scattering from the two GGDs (~ 75 nW at the detector plane), the laser power measured at each PD is buried in the electronic and environmental noise.

We first outline a brief theoretical description of the cross-spectrum method [105, 106, 104, 137]. The incident optical field is assumed to be represented by a plane wave with a Gaussian cross-section profile. The ground glass diffuser is modeled as a collection of independent scattering centers which will modify the phase of the incident field locally. Paraxial approximation and scalar field theory are used to simplify the description such that the principle of image reconstruction is highlighted and the overall logic is not overwhelmed by irrelevant details.

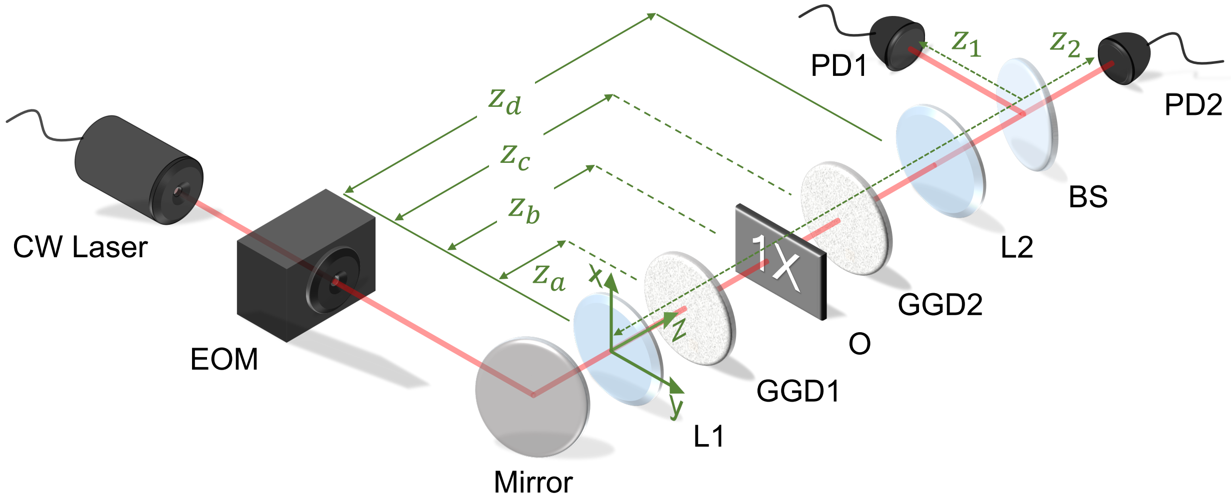

Figure 4.6: Schematic of the experimental setup. We use a modulated CW laser for illumination. The object is sandwiched between two GGDs. Signal at each detector is made to be much lower than the noise level. EOM: electro-optic modulator; L: lens; GGD: ground glass diffuser; O: object; BS: beam splitter; PD: photodetector. The Cartesian coordinate is located in the center of L1 with z-axis pointing along the propagation direction of the light.

As shown in Fig. 4.6, a Cartesian coordinate system is placed in the center of L1, with the z-axis pointing along the propagation direction of the light. A collimated incident beam of radius σ is focused by L1 with focal length f_1. The scattering centers on GGD1 will produce an electric field at distance z with the form

$$\begin{aligned} E\left(\boldsymbol{\rho}, z, t\right) = \frac{-ik}{2\pi} A\left(z - z_a\right) \times \\ \int \mathrm{d}^2\boldsymbol{\rho}_a E\left(\boldsymbol{\rho}_a, z_a, t\right) R\left(\boldsymbol{\rho}_a\right) G\left(\boldsymbol{\rho} - \boldsymbol{\rho}_a, z - z_a\right), \end{aligned} \tag{4.4}$$

where $\boldsymbol{\rho} = (x, y)$ is the position vector in the transversal plane at distance z from L1, k is the wave vector, $R\left(\boldsymbol{\rho}_a\right)$ describes GGD1 as a phase plate due to the scattering centers at position $\boldsymbol{\rho}_a$ in the plane at distance z_a, which imprint the random phase profile on the propagating field. $E\left(\boldsymbol{\rho_a}, z_a, t\right)$

is the profile of the field at the left surface of GGD1, which is given by

$$E\left(\boldsymbol{\rho}_a, z_a, t\right) = E_0\left(t\right) E_a e^{-i\left(\nu_0 t - k z_a\right)} \times \exp\left\{-\frac{E_a}{2}\left(\frac{ik}{f_1} + \frac{1}{2\sigma^2}\right)\boldsymbol{\rho}_a^2\right\}, \tag{4.5}$$

where $E_a = -\frac{ik}{2z_a}\frac{1}{1/4\sigma^2 + (ik/2)(1/f - 1/z_a)}$, $E_0\left(t\right) = \sqrt{I_0 \cos 2\pi f_{mod} t}$ expresses a sinusoidal-modulation of light intensity I_0 at frequency f_{mod}, and ν_0 is the frequency of the laser. We also define $A\left(z\right) = e^{ikz}/z$ and $G\left(\boldsymbol{\alpha}; \beta\right) = e^{ik|\boldsymbol{\alpha}|^2/2\beta}$. The integration in Eq. (4.4) is performed over the illumination area on GGD1.

When the step size is made roughly about the same size as the focal spot after GGD1, and much smaller as compared to the object size, the object is considered as scanned point by point, *i.e.*, the sample transparency can be considered constant for each scanning point. We can model the object as a transmission function $T\left(\boldsymbol{\rho}_b\right)$ where $\boldsymbol{\rho}_b$ is the position vector in the object plane. Upon passing through the object, being scattered by GGD2, and being collected by L2, the field at the two detectors is found to be

$$\begin{aligned} E\left(\boldsymbol{\rho}_b, z_j, t\right) = \frac{-ik}{2\pi}\tilde{A} \iiiint & \mathrm{d}^2\boldsymbol{\rho}_j \mathrm{d}^2\boldsymbol{\rho}_d \mathrm{d}^2\boldsymbol{\rho}_c \mathrm{d}^2\boldsymbol{\rho}_a \\ & \times E\left(\boldsymbol{\rho}_a, z_a, t\right) R\left(\boldsymbol{\rho}_a\right) R\left(\boldsymbol{\rho}_c\right) T\left(\boldsymbol{\rho}_b\right) \\ & \times G\left(\boldsymbol{\rho}_c - \boldsymbol{\rho}_a, z_c - z_a\right) G\left(\boldsymbol{\rho}_d - \boldsymbol{\rho}_c, z_d - z_c\right) \\ & \times G\left(\boldsymbol{\rho}_j - \boldsymbol{\rho}_d, z_j - z_d\right) G\left(-\boldsymbol{\rho}_d, f_2\right), \end{aligned} \tag{4.6}$$

where $\tilde{A} = A\left(z_c - z_a\right) A\left(z_d - z_c\right) A\left(z_j - z_d\right)$, z_j $(j = 1, 2)$ denote the path length between the detector j and L1, f_2 is the focal length of L2, $R\left(\boldsymbol{\rho}_c\right)$ describes the random phase profile due to scattering on GGD2. $G\left(-\boldsymbol{\rho}_d; f_2\right)$ is the propagation factor of L2.

The total signals measured by the two photodetectors for each scanning position centered at $\boldsymbol{\rho}_b$ can be expressed as

$$S\left(\boldsymbol{\rho}_b, z_j, t\right) = I\left(\boldsymbol{\rho}_b, z_j, t\right) + N_j\left(t\right), \tag{4.7}$$

where $I(\boldsymbol{\rho}_b, z_j, t) \equiv E(\boldsymbol{\rho}_b, z_j, t) E^*(\boldsymbol{\rho}_b, z_j, t)$ is the intensity at detector j, $N_j(t)$ is a white noise distribution that models all the noise due to detectors and environment at detector j. It follows that the time-domain cross-correlation is given by

$$C(\boldsymbol{\rho}_b, \tau) = \int_0^{\mathcal{T}} \mathrm{d}t S^*(\boldsymbol{\rho}_b, z_1, t) S(\boldsymbol{\rho}_b, z_2, t+\tau), \tag{4.8}$$

where $\mathcal{T}$ is the measurement time. We further assumed that the correlations between intensity and noise vanish since they are uncorrelated. On substituting from Eq. (4.7) into Eq. (4.8), we obtain

$$\begin{aligned} C(\boldsymbol{\rho}_b, \tau) &= \int_0^{\mathcal{T}} \mathrm{d}t I(\boldsymbol{\rho}_b, z_1, t) I(\boldsymbol{\rho}_b, z_2, t+\tau) \\ &+ \int_0^{\mathcal{T}} \mathrm{d}t N_1(t) N_2(t+\tau) \\ &= \int_0^{\mathcal{T}} \mathrm{d}t E(\boldsymbol{\rho}_b, z_1, t) E^*(\boldsymbol{\rho}_b, z_1, t) \\ &\qquad E(\boldsymbol{\rho}_b, z_2, t+\tau) E^*(\boldsymbol{\rho}_b, z_2, t+\tau) \\ &+ \int_0^{\mathcal{T}} \mathrm{d}t N_1(t) N_2(t+\tau). \end{aligned} \tag{4.9}$$

where $E(\boldsymbol{\rho}_b, z_j, t)$ $(j = 1, 2)$ is given by Eq. (4.6). The scattering centers are independent of each other and satisfy Gaussian statistics. Taken over all possible realizations, the random phase term $R(\boldsymbol{\rho}_i)$ obeys

$$\langle R(\boldsymbol{\rho}_i) R^*(\boldsymbol{\rho}'_i) \rangle = \delta(\boldsymbol{\rho}_i - \boldsymbol{\rho}'_i) \tag{4.10}$$

and

$$\begin{aligned} &\langle R(\boldsymbol{\rho}_i) R^*(\boldsymbol{\rho}'_i) R(\boldsymbol{\rho}''_i) R^*(\boldsymbol{\rho}'''_i) \rangle \\ &= \delta(\boldsymbol{\rho}_i - \boldsymbol{\rho}'_i) \delta(\boldsymbol{\rho}''_i - \boldsymbol{\rho}'''_i) + \delta(\boldsymbol{\rho}_i - \boldsymbol{\rho}'''_i) \delta(\boldsymbol{\rho}'_i - \boldsymbol{\rho}''_i) \end{aligned} \tag{4.11}$$

where $i = a, c$ and $\delta(\boldsymbol{\rho}_i - \boldsymbol{\rho}'_i)$ is the delta function. Using Eq. (4.6) and (4.10), Eq. (4.9) can be calculated without difficulty. Since the measured noise intensities from the two detectors are independent, their cross-correlation is a constant. The second term in Eq. (4.9) can be expressed as

$$\int_0^{\mathcal{T}} \mathrm{d}t N_1(t)\, N_2(t+\tau) = \mathcal{T}\bar{N}_1\bar{N}_2. \tag{4.12}$$

where $\bar{N}_1$ and $\bar{N}_2$ represent the average noise levels at PD1 and PD2, respectively. Upon substituting Eq. (4.5), (4.6), (4.10), and (4.12) into Eq. (4.9), we obtain after carrying out the integrals

$$C(\boldsymbol{\rho}_b, \tau) \propto \mathcal{T}\left|T(\boldsymbol{\rho}_b)\right|^4 \cos\left(2\pi f_{mod}\tau\right) + \mathcal{T}\bar{N}_1\bar{N}_2. \tag{4.13}$$

It follows from Eq. (4.13) that the cross-spectrum is

$$\begin{aligned}\Gamma(\boldsymbol{\rho}_b, \omega) &= \int_{-\infty}^{\infty} C(\boldsymbol{\rho}_b, \tau)\, e^{-i\omega\tau}\mathrm{d}\tau \\ &= \Gamma_0\mathcal{T}\left|T(\boldsymbol{\rho}_b)\right|^4 \delta\left(\omega - 2\pi f_{mod}\right) + \mathcal{T}\delta(0)\,,\end{aligned} \tag{4.14}$$

where $\Gamma_0 = \left(\frac{4\pi^2}{k^2}\right)^2 \frac{(\pi\sigma^2)^2\left|\tilde{A}\right|^4 I_0^2}{f_{mod}}$. The cross-spectrum is a sum of frequency peak signal multiplied by the transmission function $\left|T(\boldsymbol{\rho}_b)\right|^4$ and uniform noise background. Scanning the object and recording $S_1(t)$ and $S_2(t)$ at every position $\boldsymbol{\rho}_b$, we can calculate the cross-spectrum as a function of the position. A heat map of $\Gamma(\boldsymbol{\rho}_b, \omega = 2\pi f_{mod})$ will produce an image of the object, because $\left|T(\boldsymbol{\rho}_b)\right|^4$ serves as a "mask" that modulates the amplitudes of the cross-spectrum from position to position as indicated in Eq. (4.14), and the shape of the object is finally encoded in $\Gamma(\boldsymbol{\rho}_b, \omega = 2\pi f_{mod})$. Also, the longer the integration time $\mathcal{T}$ is, the greater the amplitude of the frequency peak will be; while the cross spectrum of the noise does not contribute to the image reconstruction process. This suggests that the signal-to-noise ratio can be improved by increasing $\mathcal{T}$. Therefore, even if the output signal undergoes scattering and is below the noise level of the detectors, this method can still reconstruct the image of the target.

To demonstrate that our method works experimentally for both static and dynamic scattering media, we perform the measurements under three situations: 1. imaging without diffuser (no diffuser, ND); 2. the object is sandwiched between two static diffusers (SDs); and 3. the two diffusers are moved back and forth together by a motorized stage (dynamic diffusers, DDs). The stage moves at a random speed with upper limits of the speed and acceleration set to be 500 mm/s and 1500 mm/s^2, respectively. The full range is 1.5 cm. The object has the letter "1X" being transparent and other regions being opaque. For all three cases, data are collected by an oscilloscope with a fixed sample rate at 2 GHz. At each position, 1 million data points are taken to calculate the cross-spectrum, corresponding to 500 μs integration time which ensures a strong cross-correlation signal. The whole image contains 100×140 pixels (number of steps scanned) with the pixel size (scanning step size) of 25 μm.

The main experimental result is shown in Fig. 4.7, of which the pixel values v are normalized by $\tilde{v} = (v - v_{min})/(v_{max} - v_{min})$. In the first column, we directly plot the intensity measured by the detectors; while, in the second column, we plot $\Gamma\left(\boldsymbol{\rho}_b, 2\pi f_{mod}\right)$. The first row shows ND images. The second and third row list images obtained with SD and DD, respectively. We summarize the visibility of images in Table 4.1, which is calculated by $V = (\bar{\tilde{v}}_s - \bar{\tilde{v}}_b)/(\bar{\tilde{v}}_s + \bar{\tilde{v}}_b)$, where $\bar{\tilde{v}}_s$ and $\bar{\tilde{v}}_b$ are the average pixel values of signal ("1X" region) and background, respectively. As shown in Fig. 4.7, in both SD and DD cases, when the scattering media is present, the recorded intensity does not show any image in either case, the extremely low visibility is a sign that our signal is truly at the noise level of the detectors. On the other hand, in both cases, the images are still retrieved using the cross-spectrum technique with high visibility. The results suggest that the cross-spectrum method can image an object hidden behind both static and dynamic scattering media. We also notice that the visibility of the cross-spectrum image is higher than the intensity image even though there is no diffuser (ND), which suggests cross-spectrum is also an effective way to enhance signal-to-noise ratio when the scattering media is absent.

To further test our method, we also compare the measured images from different acquisition time (50 $\mu s, 100$ μs, and 500 μs) with the same sample rate. The incident intensity of light is fixed for the static and dynamic diffusers. Simulation is also performed for the intensity and cross-spectrum based on Eq. (4.7) and Eq. (4.14), respectively, as a comparison with the experimental

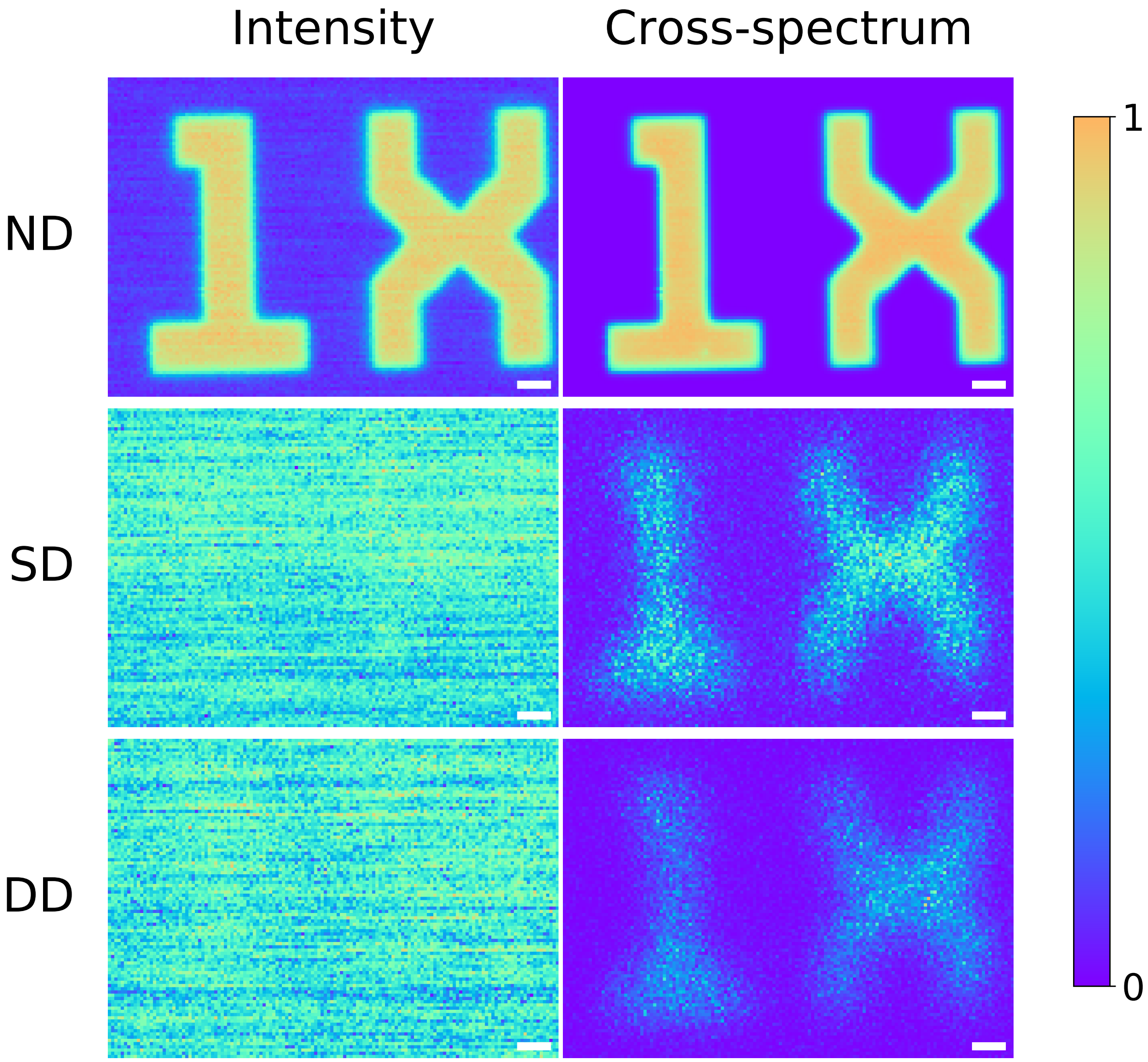

Figure 4.7: Raster-scan images for an object with the letter "1X" being transparent and other regions being opaque. Cross-spectrum images are generated by plotting $\Gamma\left(\boldsymbol{\rho}_b, \omega = 2\pi f_{mod}\right)$ (see Eq. (4.14)). Scale bar, 40 pixels. ND: no diffuser. SD: static diffuser. DD: dynamic diffuser. Scale bar: 10 pixels (0.25 mm).

Diffuser State	Intensity	Cross-spectrum
No diffuser (ND)	0.725	0.967
Static diffuser (SD)	0.032	0.451
Dynamic diffuser (DD)	0.031	0.558

Table 4.1: Visibility for different diffuser states

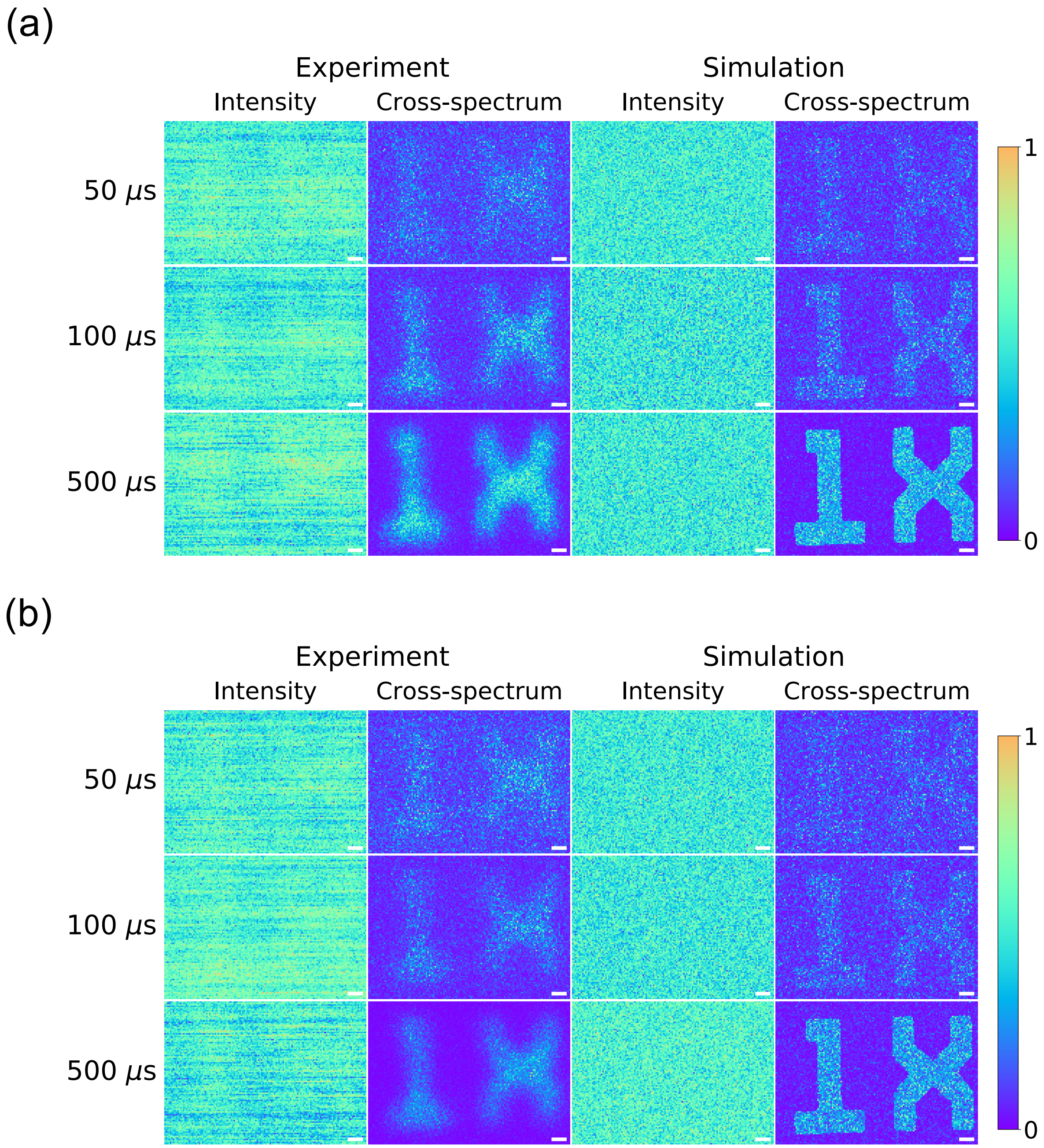

Figure 4.8: Raster-scan images and simulations for different acquisition time with (a) static diffusers and (b) dynamic diffusers. Scale bar: 10 pixels (0.25 mm).

Acquisition time	Static diffuser (SD)		Dynamic diffuser (DD)	
	Intensity	Cross-spectrum	Intensity	Cross-spectrum
50 μs	0.027 ± 0.004	0.135 ± 0.009	0.035 ± 0.005	0.190 ± 0.004
100 μs	0.033 ± 0.004	0.332 ± 0.001	0.030 ± 0.002	0.305 ± 0.004
500 μs	0.034 ± 0.003	0.466 ± 0.008	0.048 ± 0.004	0.560 ± 0.002

Table 4.2: Visibility of different acquisition time for static and dynamic diffuser states

results. Specifically, the simulated signal is given by

$$S_j\left(x,y,t\right)=\frac{\alpha T\left(x,y\right)I\left(t\right)+\beta N_j\left(t\right)}{\sqrt{\alpha^2+\beta^2}} \tag{4.15}$$

where $j=1,2$ is the index of detectors, and $t=0,1,2,\cdots,t_N$ is the discrete time in which $t_N=\mathcal{T}r_s$ is determined by the acquisition time $\mathcal{T}$ and the sample rate r_s. α and β are coefficients that control the relative magnitude of the optical signal $I\left(t\right)$ and the noise $N_j\left(t\right)$. The function

$$T\left(x,y\right)=\begin{cases}0.95, & \left(x,y\right)\in\text{object}\\ 0.05, & \left(x,y\right)\in\text{background}\end{cases} \tag{4.16}$$

gives the transmission coefficient of the object (transparent region) and the background (opaque region), respectively. The incident sinusoidal optical intensity is defined by

$$I\left(t\right)=\sin\left(2\pi f_{mod}\frac{t}{r_s}\right)+1 \tag{4.17}$$

and the additive white noise due to environment and detectors is simulated with independent Gaussian noise

$$N_j\sim\mathcal{N}\left(0,\sigma\right) \tag{4.18}$$

at every time stamp t, where σ is the standard deviation. The simulation was done with $\alpha=0.02$

and $\beta = 1.0$ for all cases, and σ is set to be 5 and 6 for static and dynamic diffusers, respectively. The results are shown in Fig. 4.8, the corresponding visibility of the experimental results are listed in Table 4.2. It can be seen that, in general, the longer the integration time is, the higher visibility one can achieve for both static and dynamic diffusers. This means we can obtain a clear image at the expense of a long acquisition time. We note that the visibility of the recorded intensity image is kept extremely low even when one increases the acquisition time up to 10 times. Nevertheless, the cross-spectrum image becomes more and more clear. The visibility also increases much faster than that of the intensity measurement when increasing the acquisition time. We point out that the fundamental limit of imaging speed is the acquisition length, which is on the order of 100 μs for the current setup but can be, in principle, orders faster with higher modulation frequency and higher sample rate (GHz range laser modulation speed and detection). The raster scan speed can also be much improved if, for instance, a 2D galvo-resonant scanner is integrated into the system.

4.4 Conclusion

In conclusion, we have developed a cross-spectrum method to extract a weak optical signal from the extremely noisy background and image objects hidden behind scattering media. The major advantage of this scheme is that it uses a CW laser in a non-invasive manner which would be easy to implement and bio-tissue friendly. It is effective for both static and dynamic media, making it adaptive in most application situations with various scattering levels, as long as the power of the incident light and the integration time is sufficient so that the cross-spectrum signal overcomes the noise level. With the fast acquisition time with current technology, our scheme paves the way for efficient imaging in previously inaccessible scenarios.

5. SINGLE-PIXEL IMAGING THROUGH SCATTERING MEDIA VIA SPACE-TIME ENCODED ILLUMINATION

5.1 Introduction

In Chapter 4, we have successfully developed an imaging technique based on cross-spectral extraction of the modulation frequency of the source. However, the raster-scan nature of this technique leads to a long acquisition time of the image. Typically, it takes about 1 s to complete the measurement and computation for one pixel, and an image of 100×100, which is fairly small, will take 3 hours to complete. Therefore, developing a full-field counterpart of this imaging technique is highly desired. A simple way to accelerate the imaging process is to parallelize the raster scan, i.e., generate a bundle of intensity-modulated laser beams. Each beam in the bundle must have a unique modulation frequency, otherwise, there is no way to identify which frequency corresponds to which pixel. This one-to-one relationship between the modulation frequency and the spatial location of the beam is where the spatial resolution comes from.

This parallelism can be implemented with the spatial light modulator (SLM). One type of SLM technology is based on the digital micromirror device (DMD), which consists of an array of individually controllable micromirrors [138, 139]. This device can provide fast spatial light modulation for a wide range of wavelengths. Each micromirror has two orientations with respect to the array plane ($\pm 12^{\circ}$), and light incident normally on the array plane is reflected into two paths $\pm 24^{\circ}$, respectively. The orientation of the micromirrors is programmable with customized binary patterns in which the pixel values "1" and "0" correspond to the two tiled states of the mirrors. Therefore, DMD can spatially modulate the profile of incident light beam and project intensity patterns onto a screen.

In this chapter, we report a computational imaging technique, termed space-time encoded pattern (STEP) illumination, which is a parallel version of the technique developed in Chapter 4 and allows non-invasive imaging of an object through scattering media and around corners. We show that the images of objects can be reconstructed from a 1D time series of light intensity measured by a single-pixel photodetector. Specifically, inspired by the concepts of space-time duality, intensity modulation [94], and Fourier-transform-based discrimination [91, 140, 141, 142, 143, 144], we design a sequence of patterns that consists of a bundle of sinusoidal time series with different frequencies, such that every spatial location in each pattern is encoded by a unique frequency which is also a unique feature of the periodic oscillation of pixel values along "time" axis (*i.e.*, looking at one spatial location through different patterns). We illuminate the diffuser-object system with this sequence of patterns and collect the transmitted light by a single-pixel detector. With the help of an image reconstruction algorithm based on fast Fourier transform (FFT), the images of the objects can be retrieved without prior knowledge of the objects and the scattering media. As a proof of concept, we experimentally demonstrate our technique with ground glass diffusers and slices of chicken breast (1.2-mm thick) as the scattering media. The design of STEP avoids the use of a high-resolution camera and allows an elegant frequency-domain image reconstruction algorithm that is more computationally efficient than previous single-pixel imaging methods, which may be more favorable in many application fields.

5.2 The principle of STEP

The mechanism of STEP is sketched in Fig. 5.1. We generate a sequence of grayscale (8-bit, 256 pixel values) patterns of height H and width W ($H \times W$ matrix). For a spatial location (i, j) (ith row, jth column), the time series is given by

$$a_{ijt} = 127.5 \sin\left(2\pi f_{ij} \frac{t}{r_s}\right) + 127.5, t = 0, 1, 2, \cdots M_{\text{patt}} - 1, \tag{5.1}$$

in which r_s is the sample rate, t is the discrete time variable (index of the patterns), M_{patt} is the total number of patterns, and the frequency f_{ij} is defined by

$$f_{ij} = f_0 + (j + iW)\,\Delta f \tag{5.2}$$

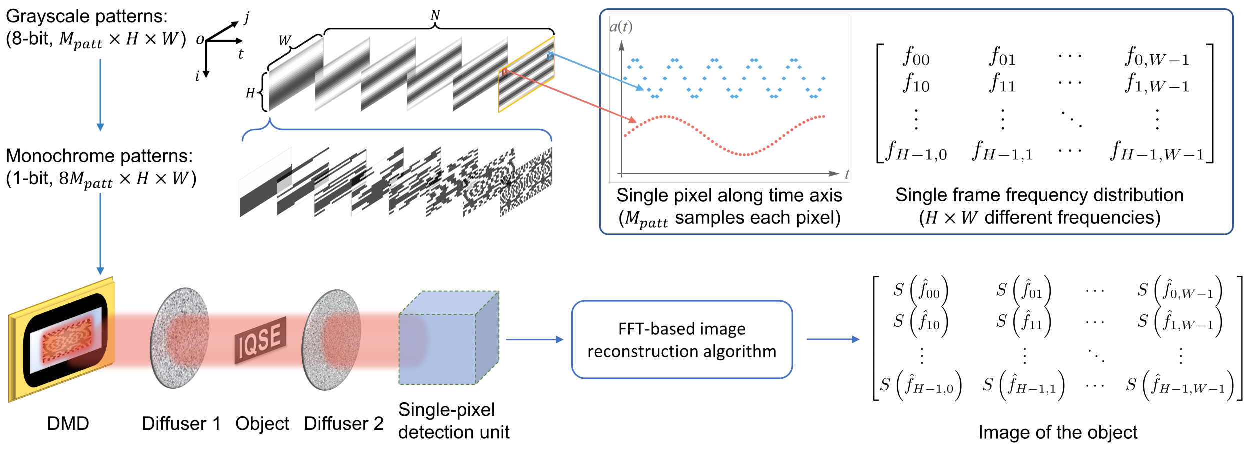

Figure 5.1: The principle of STEP. The sequence of patterns consists of a bundle of sinusoidal time series with unique frequency at each spatial location. For location (i, j), the frequency is f_{ij}, which is also a unique feature of the periodic oscillation of pixel values along the "time" axis (i.e., looking at one spatial location through different patterns). The grayscale patterns are first decomposed into monochrome patterns, and then projected onto the object-diffuser system. The transmitted light is collected by a single-pixel detection unit, and the image is reconstructed by a FFT-based algorithm.

where $i = 0, 1, \cdots, H-1, j = 0, 1, \cdots, W-1$, are the row and column index of the pixels, respectively, f_0 is the starting frequency, and Δf is the increment of the frequency. To avoid signal aliasing, we set $r_s = 8f_{\max}$, where $f_{\max} = f_0 + (HW-1)\Delta f$. The grayscale patterns are then decomposed to $8M_{\text{patt}}$ monochrome (1-bit, 2 pixel values) patterns in order to be compatible with the input format of the DMD. The monochrome patterns are successively projected to the diffuser-object system and synchronically collected by the single-pixel detection unit. The 1D time series intensity can be expressed by

$$I_t = \sum_{i,j} a_{ijt} I_{ij} + N_t, \tag{5.3}$$

where I_{ij} is the illumination intensity at location (i, j) of the pattern displayed on DMD and N_t is a white noise term describing the noise of detector and environment. To reconstruct an image, I_t is transformed to the spectral domain

$$S(\omega) = \mathcal{F}_t\{I_t\} \propto M_{\text{patt}} \sum_{i,j} I_{ij} \delta(f - f_{ij}) + \bar{N} \tag{5.4}$$

where $\mathcal{F}_v$ denotes Fourier transform with respect to the variable v, M_{patt} happens to be the number of data points in the discrete 1D time series (integration length) since the measurement is synchronized with the projection, and $\bar{N}$ is the average noise level. For each f_{ij} in the patterns, we find the closest frequency $\hat{f}_{ij}$ in the spectrum and save its magnitude $S(\hat{f}_{ij})$. Finally, a $H \times W$ matrix is filled with all the $S(\hat{f}_{ij})$ in their locations (i, j), and a heat map of this matrix will yield an image of the object. It is the one-to-one correspondence between the frequency f_{ij} and the spatial location (i, j) that allows us to retrieve the spatial information computationally, and therefore we only need to measure the transmitted light with a single-pixel detector. We note here that the noise only contributes a constant term in the spectrum given by Eq. (5.4).

5.3 Experimental demonstration of STEP

The experimental setups for imaging with line-of-sight and around-corner detection are illustrated in Fig. 5.2a and 5.2b, respectively. A solid-state laser (633 nm) is used to illuminate the DMD, which spatially modulated the incident laser beam and generate a set of illumination projections with a spatial structure that is similar to the input monochrome patterns. Each projection has 20×60 pixels, and each pixel is maintained by a 10×10 array of DMD micromirrors (each mirror has size $10.8\ \mu m \times 10.8\ \mu m$). We define such an array of mirrors as a single "DMD pixel". The patterns are then imaged by a lens (L3) with magnification equals to 2. High-order images due to diffraction are filtered out by an iris (I) such that only the zeroth-order image with the strongest intensity is formed in the image plane. A high-contrast object (O) with letters "IQSE" (3 mm $\times$ 10 mm) being transparent is placed at the image plane of L3, where the zeroth-order images of the patterns are directly projected on the region of "IQSE" without scattering media. Then, two ground glass diffusers (D1 and D2, 220 grit) are inserted to block the view of the object. The distances between the object and D1 and D2 are about 1 mm and 7 mm, respectively. The diffusers can be kept stationary or moved back and forth by a motorized stage. For line-of-sight detection (Fig. 5.2a), a lens (L4) followed by a photodetector (PD) is placed behind D2 to collect the transmitted light; while, for around-corner detection (Fig. 5.2b), the light collected by L4 is diffusely reflected by a piece of letter paper (white) and then recollected by L5 and measured by a

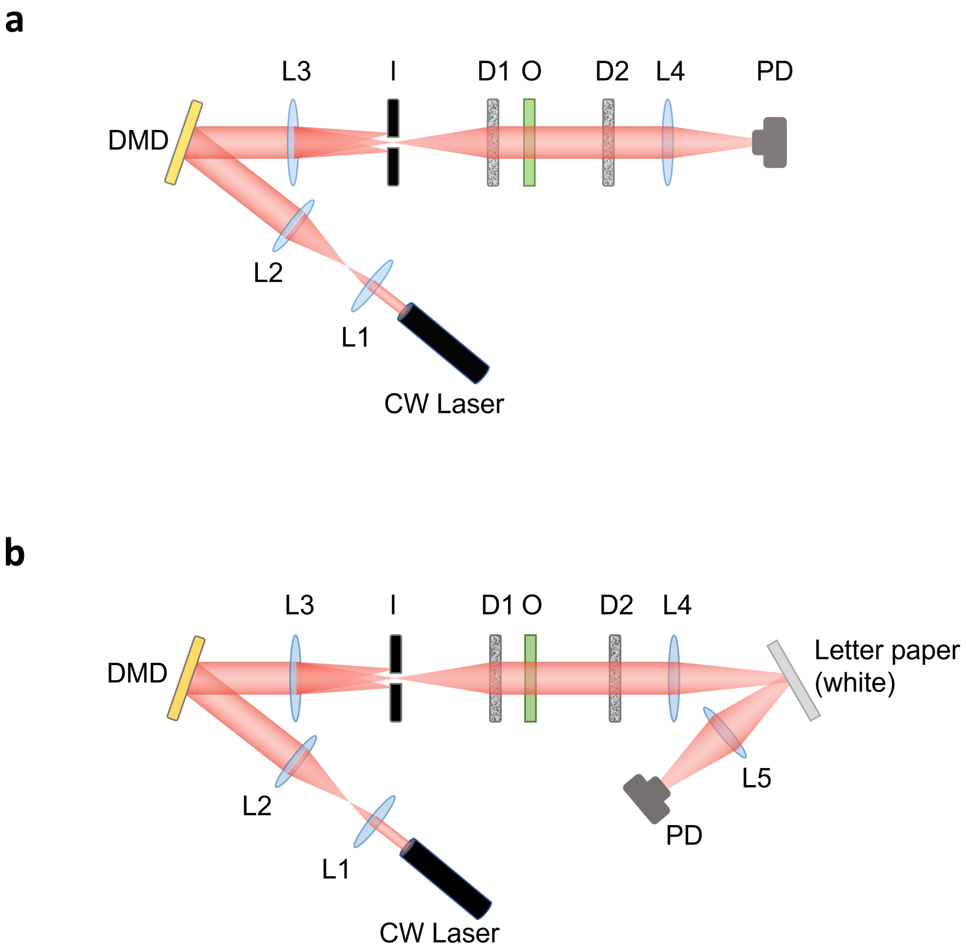

Figure 5.2: Experimental setup for demonstrating STEP. **a**. line-of-sight detection. **b**. around-corner detection. L: lens; DMD: digital micromirror device; I: iris; D: diffuser; O: object; PD: photodetector.

PD.

The image of the object is first captured by a CMOS camera under three conditions (a): 1. without scattering media (ND), 2. with stationary ground glass diffusers (SDs), and 3. with dynamic ground glass diffusers (DDs). As shown in Fig. 5.3a, the object is invisible with the present of SDs and DDs in the camera images; while our STEP imaging scheme can retrieve the images through SDs and DDs for both line-of-sight (Fig. 5.3b) and around-corner detection (Fig. 5.3c). We define

$$\beta = \frac{M_{\text{patt}}}{M_{\text{pixel}}} \tag{5.5}$$

as a rescaled "number of patterns" used in the experiment, in which M_{patt} is the number of grayscale patterns and $M_{\text{pixel}} = 120$ is the number of pixels in one pattern. The measurements in Fig. 5.2 are performed with $\beta = 100$, *i.e.*, 120000 gray-scale patterns (8×120000 monochrome patterns). To reconstruct an image, the frequency resolution of the Fourier transform

$$\delta f = \frac{r_s}{M_{\text{patt}}} = \frac{8\left[f_0 + (HW-1)\,\Delta f\right]}{\beta M_{\text{pixel}}} \tag{5.6}$$

must satisfy the condition $\delta f \geq \Delta f$, which determines the minimum value of β that is required to reconstruct an image computationally. Our experimental parameters ($f_0 = \Delta f = 0.1$, $H = 20$, $W = 60$) give $\beta \geq 8$. Fig. 5.3b and 5.3c are obtained with $\beta = 8$ and $\beta = 32$, respectively. We define the visibility of the reconstructed image to be

$$v = \frac{\bar{p}_s - \bar{p}_b}{\bar{p}_s + \bar{p}_b} \tag{5.7}$$

in which $\bar{p}_s$ and $\bar{p}_b$ are the average pixel values of the signal ("IQSE" regions) and background (other regions), respectively. The larger β is, the more capable the spectrum can distinguish target frequencies from the noisy background, resulting in a higher visibility of the reconstructed images. This is the reason why we use a larger β to process the data of around-corner detection (Fig. 5.3c), as a higher noise level is encountered in this case due to the extra scattering by the white paper. The number of raw pixels (20×60) in the reconstructed image is always the same as that of the patterns. Such a small number of pixels leads to pixelated images. Nevertheless, the pixelation effect can be eliminated computationally by applying bilinear interpolation on the raw pixels without increasing the density of pixels in the original patterns, and interpolated images of size 400×1200 are given in Fig. 5.3b and 5.3c.

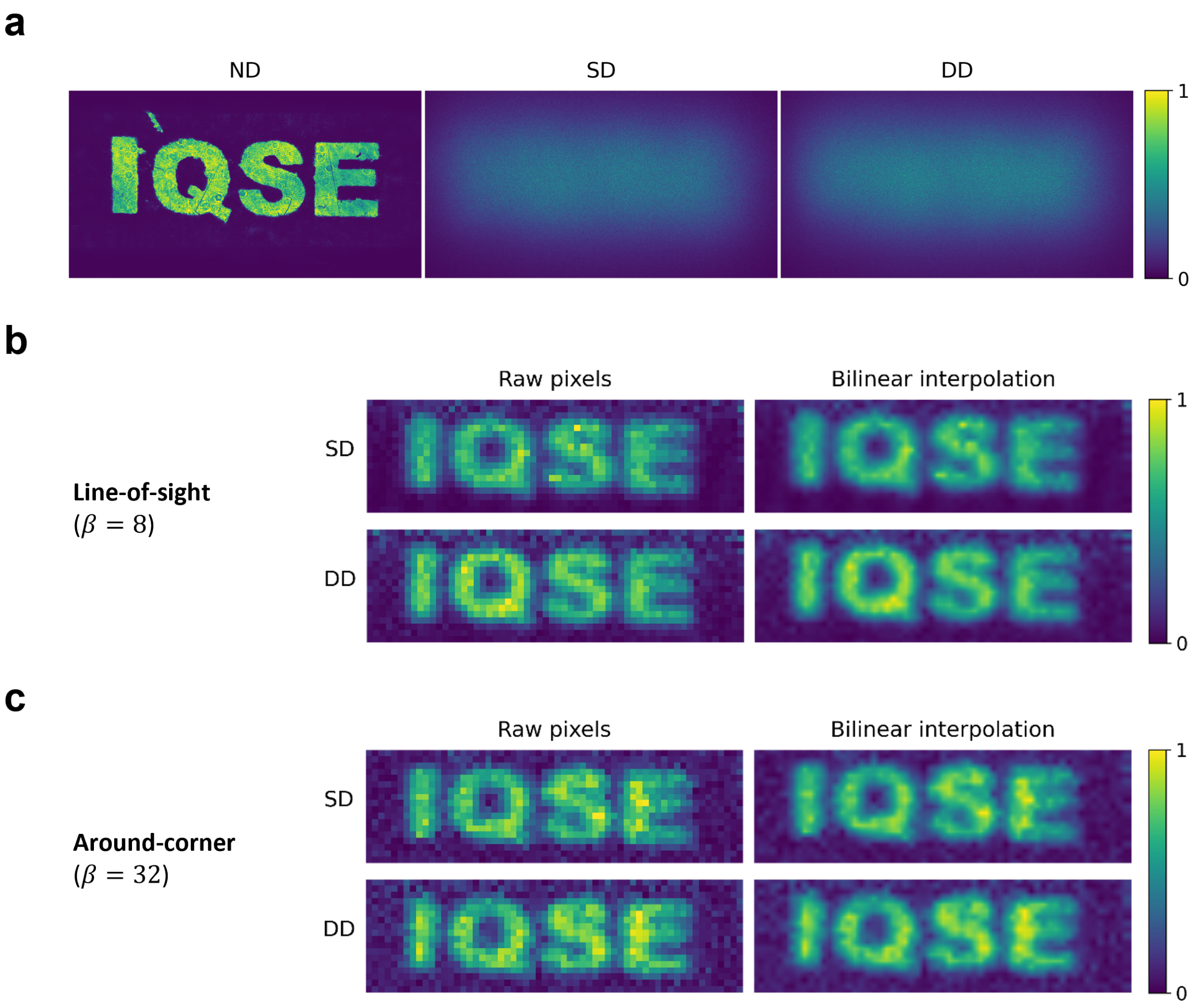

Figure 5.3: Imaging through ground glass diffusers with STEP. **a**. Images captured by a CMOS camera with no diffuser (ND), stationary diffusers (SDs), and dynamic diffusers (DDs), respectively. **b**. line-of-sight detection. Images are generated with $\beta = 8$. Bilinear interpolation is applied to remove the pixelation effect. **c**. around-corner detection. Images are generated with $\beta = 32$.

The imaging depth is determined by how well the structure of the patterns can be preserved after transmitting through the scattering media and before illuminating the object. This is related to the so-called shower-curtain effect: an object placed at a distance behind a scattering layer looks blurred, but if the object is attached to the layer, it can be clearly seen. Within a short distance after D1 in Fig. 5.2, the relative positions between the pixels on the patterns may be unchanged even after scattering, and the one-to-one correspondence between the spatial location and the frequency of the sinusoidal intensity is retained. Since the measured signal is a convolution of the patterns and the object, the spatial information can be retrieved by extracting the frequencies f_{ij}, and an image of the object can be produced by $S\left(f_{ij}\right)$. The shower-curtain effect indicates the major shortcoming of STEP: the imaging depth is shallow ($\lesssim 1$ mm for current setup). Despite this, STEP is inherently insensitive to the scattering properties of D2 and its distance from the object, because any scattering event cannot destroy the spatial information carried by the convoluted signal.

The imaging resolution is determined by the size of an individual pixel in the patterns projected onto the object: the smaller the pixel is, the more details of the object can be resolved. Imagining that the scattering media are absent in Fig. 5.2. The pixel size at the image plane of L3 is determined by the size of the DMD pixel and the magnification of the imaging system defined by L3. For a given magnification, decreasing the DMD pixel size will increase the resolution. However, the optical power reflected by each DMD pixel will be reduced due to the shrinkage of the reflective area (fewer micromirrors), resulting in a decreased signal-to-noise ratio (SNR) of the measured light. Conversely, increasing the DMD pixel will provide better SNR, which is, however, at the expense of a lower resolution. If the scattering layers are inserted, the degradation of pattern quality and the attenuation of optical power due to scattering must also be considered. Therefore, the trade-off between resolution and SNR should be decided according to the configuration of a specific setup. For our experiment, the resolution is ~ 0.2 mm, which is adequate for resolving the object of size 3 mm $\times$ 10 mm, and the transmitted light intensity is far above the shot noise level of the detector.

The imaging speed of STEP is only limited by the frame rate of the DMD, as modern computers

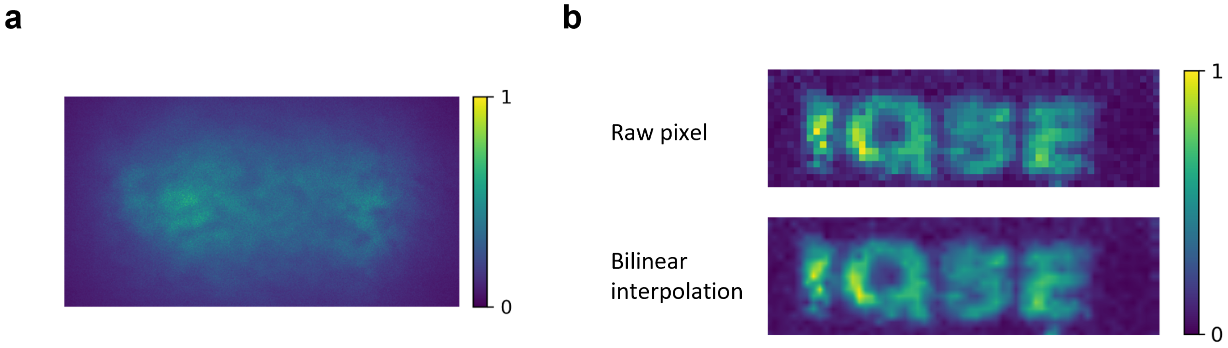

Figure 5.4: Imaging through two slices of chicken breast ($\sim$ 1.2 mm each slice) with STEP. **a**. A camera image of the object hidden in between the two slices of chicken breast. **b**. Image reconstructed by STEP with $\beta = 96$. Bilinear interpolation is applied to remove the pixelation effect.

can complete the computation in negligible time. The frame rate of our DMD is about 40 Hz, resulting in a measurement time of 7 hours for $\beta = 100$ $(8 \times 12000$ patterns), while the computation can be done within 1 s. The highest frame rate of current commercial DMD is 22.7 kHz, which will reduce our measurement time to 45 s. We expect that the speed will be further increased as the frame rate of DMD becomes faster in the future.

To further demonstrate that STEP is also insensitive to the motion of the scattering centers in the media, we replaced the D1 and D2 in Fig. 5.2 with two slices of chicken breast ($\sim$ 1.2 mm) and perform similar line-of-sight measurements with $\beta = 100$. As shown in Fig. 5.4a, the object cannot be resolved in the camera image, whereas the image can be reconstructed by STEP with $\beta = 96$ (Fig. 5.4b). An even larger β to perform the computation implies a stronger scattering in the tissues than that of ground glass diffusers (GGDs). Due to the nonuniform texture of the tissue, the transmitted light intensity is not as evenly distributed as that for the GGDs, resulting in some bright spots in the reconstructed image. The results support the argument that STEP is capable of imaging through dynamic scattering media.

5.4 Discussion

Different from other structured illumination techniques in which the information required for image reconstruction is only encoded in the spatial structure of the patterns, the STEP illumination also encodes the information (frequencies) in time. One advantage of introducing the time-domain encoding is that it allows a further improvement of the visibility on top of increasing β via halving a successive segment of the data and calculating the cross-spectrum of the two halves. The cross-correlation technique has been demonstrated very effective in weak signal detection. Cross-spectrum is the frequency-domain representation of the cross-correlation of two time series signals, which is defined by

$$S_{12}\left(f\right) \equiv \mathcal{F}_{\tau}\left\{g_1 \star g_2\right\} = \mathcal{F}_t\left\{g_1\right\} \cdot \mathcal{F}_t\left\{g_2\right\} \tag{5.8}$$

where $\mathcal{F}_v$ denotes Fourier transform with respect to variable v, τ is the delay in time, and

$$g_1 \star g_2 = \sum_{t=0}^{M} g_{1,t} g_{2,t+\tau} \tag{5.9}$$

is the cross-correlation of two discrete signals g_1 and g_2 with M data points. For images recon-

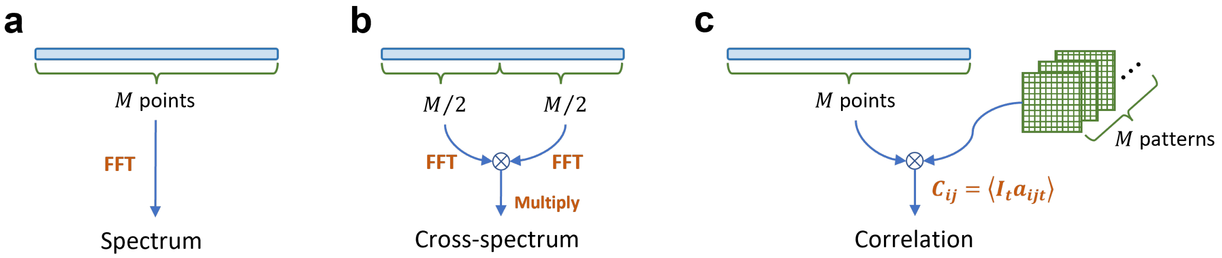

Figure 5.5: A schematic of the image reconstruction algorithms based on fast Fourier transform (FFT), cross-spectrum, and correlation. **a**. A segment of M data points in time domain is transformed by FFT to frequency domain (spectrum). **b**. A segment of M data points are divided into two halves, and their cross-spectrum is calculated by Eq. (5.8). **c**. The correlation between a segment of M data points and the time series in the original pattern sequence is calculate by Eq. (5.12).

structed with a specific β, higher visibility is obtained if the searching of target frequencies is performed in the cross-spectrum of the two halves of the data rather than in the Fourier spectrum of all the data. As shown in Fig. 5.5b, we divide the whole data set into two segments of the same length, and their cross-correlation is found to be

$$\begin{aligned} I_1 \star I_2 &= \sum_{t=0}^{M/2-1} \left[\sum_{ij} I_{ij} \sin\left(2\pi f_{ij} \frac{t}{r_s}\right) + N_1 \right] \left[\sum_{ij} I'_{ij} \sin\left(2\pi f_{ij} \frac{t+\tau}{r_s}\right) + N_2 \right] \\ &= \frac{M}{2} I_{ij} I'_{ij} \sin\left(2\pi f_{ij} \frac{\tau}{r_s}\right) + \frac{M}{2} \bar{N}_1 \bar{N}_2 \end{aligned} \tag{5.10}$$

where M is the total length of the two signal segments, and $\bar{N}_1$ and $\bar{N}_2$ are the average noise levels for the two segments, respectively. It follows that the cross-spectrum is

$$S_{12}\left(f\right) = \mathcal{F}_\tau \left\{I_1 \star I_2\right\} \propto \frac{M}{2} \sum_{ij} I_{ij} I'_{ij} \delta\left(f - f_{ij}\right) + \frac{M}{2} \delta\left(0\right) \tag{5.11}$$

As we have seen in Eq. (5.4), the noise contributes a constant background equally at every frequency in the spectrum. However, in the cross-spectrum (Eq. (5.11)), the noise is concentrated to zero frequency ($\delta\left(0\right)$) and never contributes to the cross-spectral magnitude at any other frequencies. Therefore, the SNR is enhanced, leading to sharper peaks of the target frequencies and less noisy reconstructed images.

The image reconstruction can also be implemented by calculating the correlations between the measured intensity data I_t and the time series a_{ijt} in the original patterns

$$C_{ij} = \sum_{t=0}^{M-1} I_t a_{ijt} \tag{5.12}$$

Filling an $H \times W$ matrix with all the C_{ij} at their locations (i, j) will yield an image of the object. However, the visibility of the image reconstructed by correlation is lower than that of the image produced by FFT-based methods, because in this case the correlation is done without a shift in time, leading to a non-trivial contribution of the white noise. Fig. 5.6a compares the images recon-

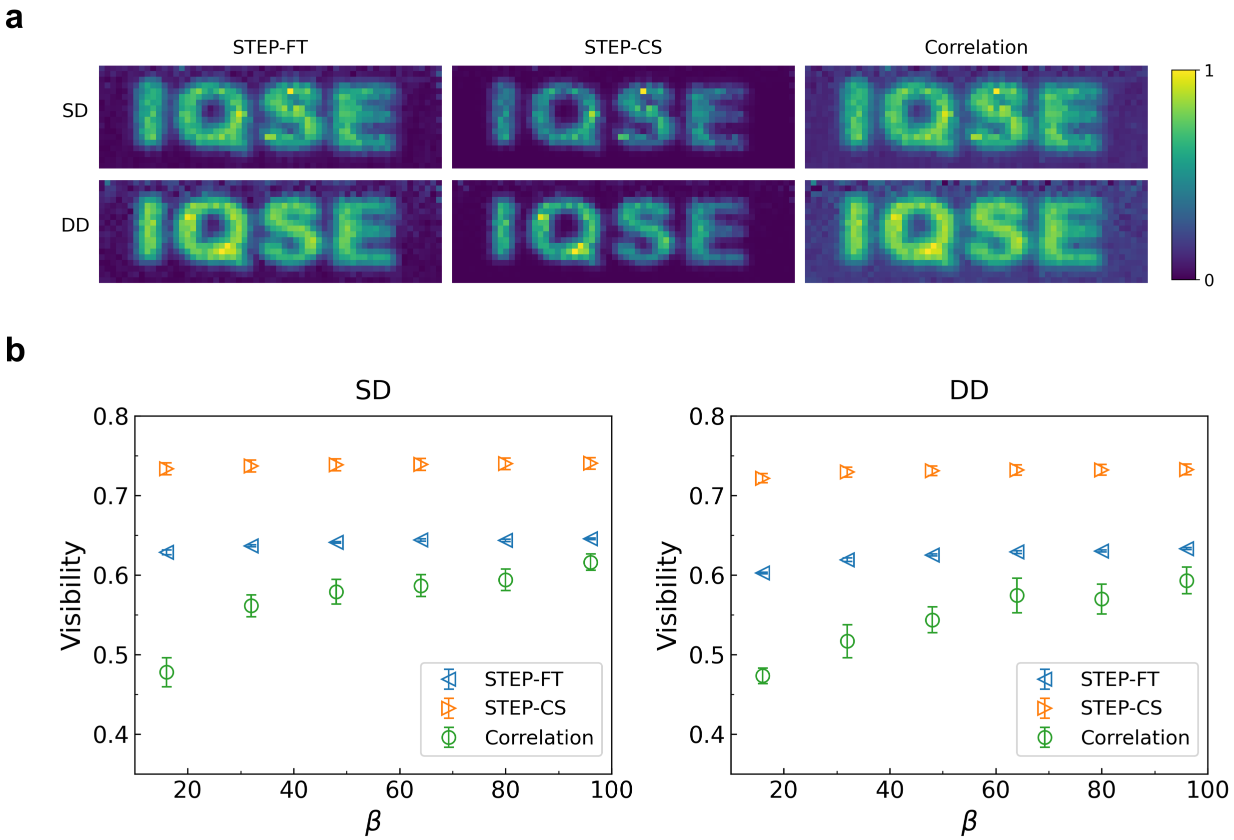

Figure 5.6: Comparison of images reconstructed by different algorithms for line-of-sight detection. **a**. Images reconstructed by Fourier transform (STEP-FT), cross-spectrum (STEP-CS), and correlation, respectively, with $\beta = 16$; **b**. Visibility of the reconstructed images using the three algorithms with different values of β.

structed by Fourier transform (STEP-FT), cross-spectrum (STEP-CS), and correlation for line-of-sight detection with ground glass diffusers and $\beta = 16$. STEP-FT is the standard algorithm used previously. As can be seen, the image generated by STEP-CS appears to be less noisy than that by STEP-FT, which supports our argument that cross-spectrum can eliminate noise. Meanwhile, the image produced by correlation is the noisiest among the three, indicating a significant contribution of the noise in the computation. Fig. 5.6b compares the visibility of the images generated by the three algorithms for different β. It is worth mentioning that the performances of STEP-FT and STEP-CS are almost independent of β: they have similar visibility over the investigated range of β and show saturation behaviors. This means high-quality images may be obtained with small data sets, and thus consume less time on computation. On the other hand, the correlation has the worst overall performance and is sensitive to the value of β. Therefore, high-quality images may only be acquired with a large number of data points, and the computation will be slow. Fig. 5.7 shows similar comparisons for around-corner detection with ground glass diffusers and $\beta = 32$, and the results agree with those in Fig. 5.6.

The correlation method also suffers from a low computational efficiency. For N patterns of size $H \times W$, both the time and space complexity of the image reconstruction via correlation are $O(H \times W \times N)$; whereas, the time complexity of FFT-based reconstruction (FT and CS) is $O\left(N \log_2 N\right)$ since the FFT algorithm is used to compute the spectrum, and the space complexity is $O\left(N\right)$ as there is no need to store the original patterns. A benchmark of the computing time for FFT-based and correlation algorithms are given in Fig. 5.8, where the rapid increase in the computing time for correlation algorithm provides a sharp contrast with those of the FFT-based methods. The high computational efficiency of the FFT-based algorithm may enable fast image processing with devices having limited computing resources.

To end the discussion, we would like to explain the reason why β is always chosen to be a multiple of 8 in our computation. We will compare $\beta = 8$ and $\beta = 9$ to show some insights. As discussed previously, any value of $\beta \geq 8$ can provide enough frequency resolution in the spectrum under our experimental conditions. Recall that our target frequencies are $[0.1, 0.2, 0.3, \cdots, 120]$

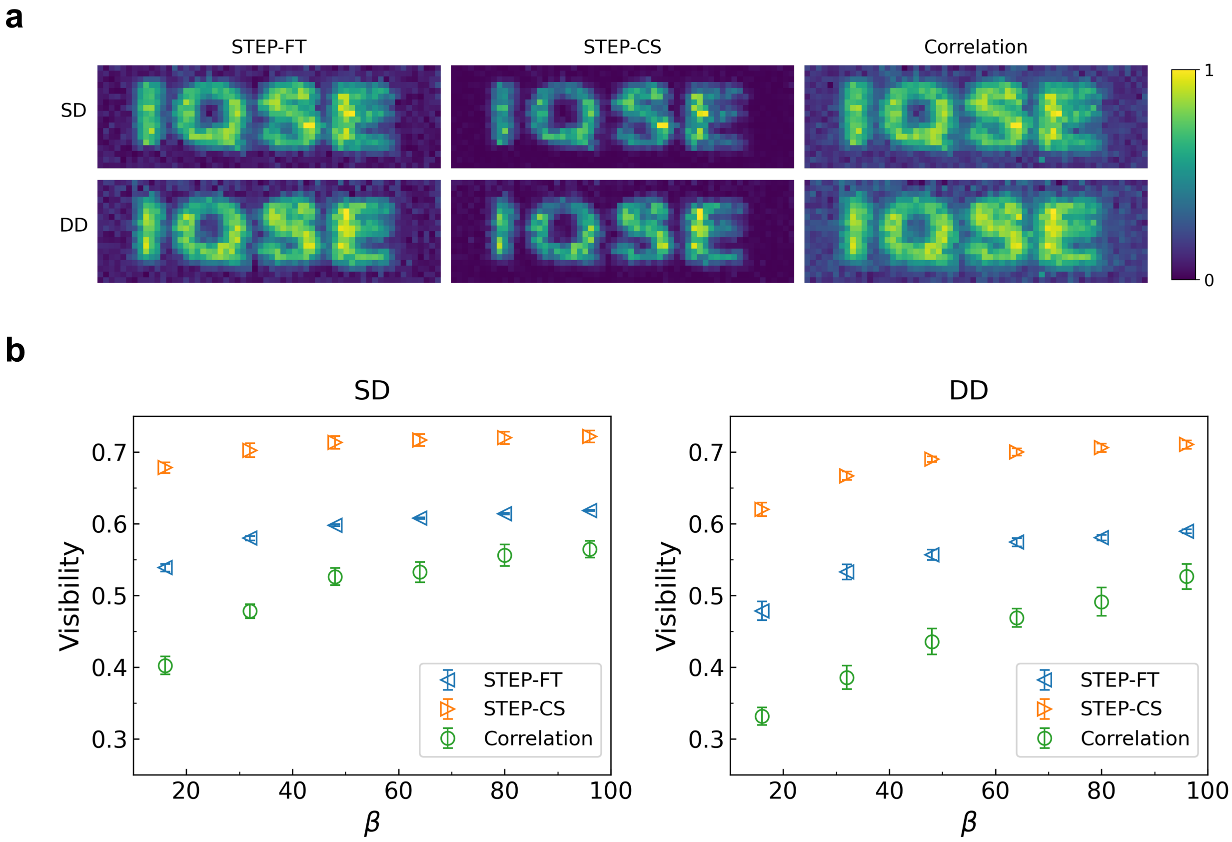

Figure 5.7: Comparison of images reconstructed by different algorithms for around-corner detection. **a**. Images reconstructed by Fourier transform (STEP-FT), cross-spectrum (STEP-CS), and correlation, respectively, with $\beta = 32$; **b**. Visibility of the reconstructed images using the three algorithms with different values of β.

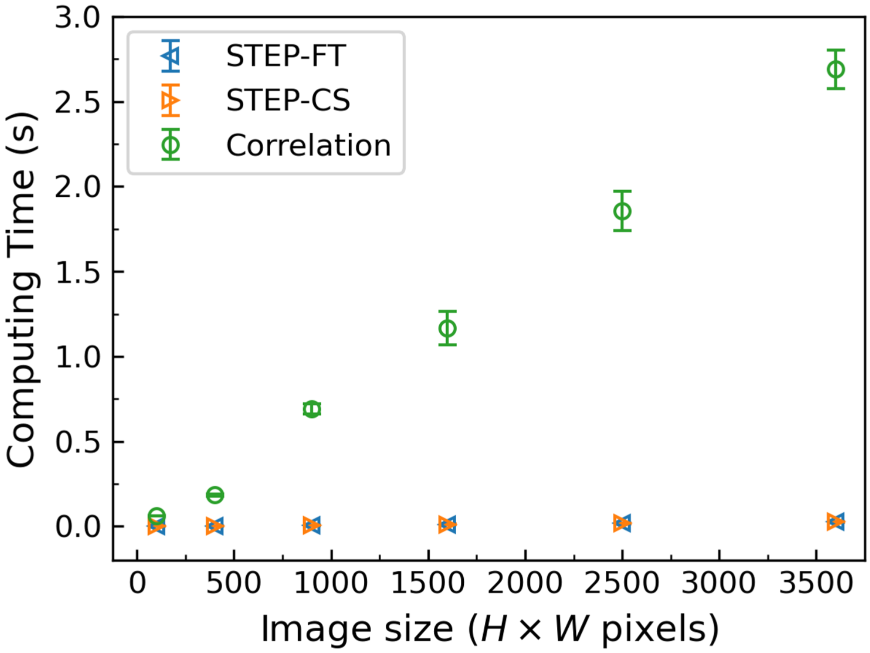

Figure 5.8: Comparison of time complexity of FFT- and correlation-based image reconstruction algorithms. Computing time are measured with different image sizes in total pixels. The computing time for correlation-based algorithm increases rapidly compared to that of the FFT-based algorithms.

(starting from 0.1 with an increment of 0.1), and the frequencies in the spectrum (discrete Fourier transform) given by $\beta = 8$ and $\beta = 9$ are listed as follows (only the leading 10 values):

$$\beta = 8: \ [0, 0.1, 0.2, 0.3, 0.4, 0.5, 0.6, 0.7, 0.8, 0.9] \tag{5.13}$$

$$\beta = 9: \ [0, 0.08889, 0.17778, 0.26667, 0.35556, 0.44444, 0.53333, 0.62222, 0.71111, 0.8] \tag{5.14}$$

We can see that, for $\beta = 8$, the closest frequencies $\hat{f}_{ij}$ we can find in the spectrum are exactly the target frequencies; while for $\beta = 9$, we can never find any $\hat{f}_{ij} = f_{ij}$, so the algorithm will select 0.0889 as the closest value to target 0.1 and 0.17778 for the target 0.2, and so on. These closest frequencies and their corresponding magnitudes are only approximations of the target frequencies and their magnitudes, so they may not produce an image as good as the exact matching frequencies. The images generated with $\beta = 8$ and $\beta = 9$ are shown in Fig. 5.9, which provide an intuitive understanding of the point we just discussed. Therefore, to get the best results, we prefer to choose a multiple of 8 as the value of β such that all the target frequencies appear in the spectrum.

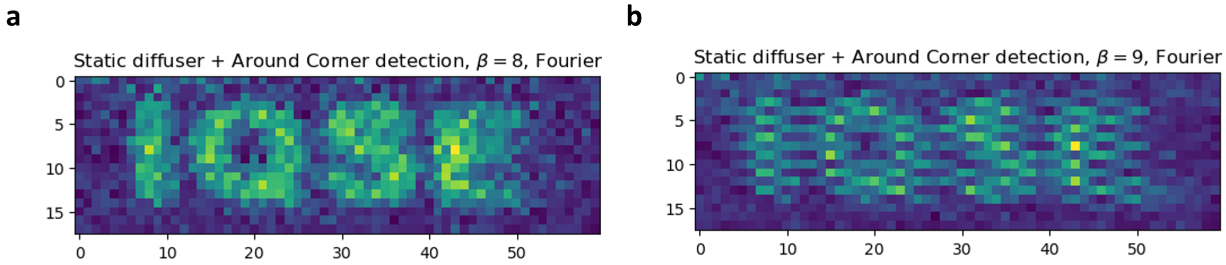

Figure 5.9: Images reconstructed with $\beta = 8$ and $\beta = 9$, respectively, with other conditions being the same.

5.5 Conclusion

In conclusion, we have developed a computational imaging method named "STEP" that can realize non-invasive imaging through scattering media and around corners with a single-pixel photodetector. This method is insensitive to the motion of the scattering centers in the media. The design of STEP removes the requirement of a high-resolution camera and allows an elegant FFT-based image reconstruction algorithm that is more computationally efficient than correlation-based methods, which may be more favorable in many application fields. Our technique provides a new perspective to realize the vision of peeking through turbid media and enables potential fast imaging for currently unreachable scenarios.

6. CONCLUSION

We have proposed a computational imaging mechanism based on time-domain information encoding and FFT-based information decoding that can realize non-invasive imaging through scattering media.

We first present an enlightening experiment on the time evolution of the off-diagonal elements of laser density matrix given by the Scully-Lamb quantum theory of laser. The spectral distribution of high order correlations of the beat note of two lasers are derived theoretically, showing that the linewidth of the second- and third-order spectral profile are 4 and 9 times wider than that of the first-order spectral profile, respectively. The theoretical expectation is verified experimentally by measuring the linewidth of the laser beat note and the correlated laser beat note of two independent He-Ne lasers. This experiment inspires the idea of imaging through scattering media by extracting the beat frequency of two lasers.

Next, the idea of detecting an object inside a scattering medium by the beat signal of two lasers is proposed, and its feasibility is confirmed by a preliminary experiment. To overcome some disadvantages of using two lasers, the method is further improved by replacing the beat signal of two lasers with an intensity-modulated laser. Using cross-spectrum detection of the modulation frequency and raster-scan measurement, we demonstrate a non-invasive and easy-to-implement scheme, by which the image of an object can be reconstructed not only through both static and dynamic diffusers but also under extremely noisy environments, i.e., the light intensity is much lower than detector noise. Besides, the use of low power CW laser ($\sim$ 20 mW) makes the method more favorable in applications involving living tissues.

To overcome the speed limit due to raster scan, the computational imaging mechanism is further improved to realize full-field imaging via space-time encoded illumination. We show that the images of objects can be reconstructed from a 1D time series of light intensity measured by a single-pixel photodetector. Specifically, we design a sequence of patterns that consists of a bundle of sinusoidal time series with different frequencies, such that every spatial location in each pattern is encoded by a unique frequency which is also a unique feature of the periodic oscillation of pixel values along “time” axis (*i.e.*, looking at one spatial location through different patterns). We illuminate the diffuser-object system with this sequence of patterns and collect the transmitted light by a single-pixel detector. With the help of a FFT-based image reconstruction algorithm, the images of the objects can be retrieved without prior knowledge of the objects and the scattering media. As a proof of concept, We experimentally demonstrate our technique with ground glass diffusers and slices of chicken breast (1.2-mm thick) as the scattering media. Various aspects of this technique, including resolution, penetration depth, imaging speed, and algorithm complexity, are discussed to provide more insights. This imaging scheme removes the requirement of a high-resolution camera and allows an elegant FFT-based image reconstruction algorithm that is more computationally efficient than correlation-based methods. Furthermore, this technique is inherently insensitive to the motion of the scattering centers in the media, and the imaging speed is only limited by the frame rate of the DMD. With the development of high-speed DMD technology, this technique may be applied to video-rate imaging through scattering media.

REFERENCES

[1] Dunsby, C. & French, P. M. W. Techniques for depth-resolved imaging through turbid media including coherence-gated imaging. *Journal of Physics D: Applied Physics* **36**, R207–R227 (2003).

[2] Ntziachristos, V. Going deeper than microscopy: The optical imaging frontier in biology. *Nature Methods* **7**, 603–614 (2010).

[3] Mosk, A. P., Lagendijk, A., Lerosey, G. & Fink, M. Controlling waves in space and time for imaging and focusing in complex media. *Nature Photonics* **6**, 283–292 (2012).

[4] Yu, H. *et al.* Recent advances in wavefront shaping techniques for biomedical applications. *Current Applied Physics* **15**, 632–641 (2015).

[5] Rotter, S. & Gigan, S. Light fields in complex media: Mesoscopic scattering meets wave control. *Reviews of Modern Physics* **89**, 015005 (2017).

[6] Yoon, S. *et al.* Deep optical imaging within complex scattering media. *Nature Reviews Physics* **2**, 141–158 (2020).

[7] Meyers, R. E., Deacon, K. S. & Shih, Y. Turbulence-free ghost imaging. *Applied Physics Letters* **98**, 111115 (2011).

[8] Shih, Y. The Physics of Turbulence-Free Ghost Imaging. *Technologies* **4**, 39 (2016).

[9] Indebetouw, G. Distortion-free imaging through inhomogeneities by selective spatial filtering. *Applied Optics* **29**, 5262–5267 (1990).

[10] Anderson, G. E., Liu, F. & Alfano, R. R. Microscope imaging through highly scattering media. *Optics Letters* **19**, 981–983 (1994).

[11] Sheppard, C. J. R. & Wilson, T. Depth of field in the scanning microscope. *Optics Letters* **3**, 115–117 (1978).

[12] Kempe, M. & Rudolph, W. Scanning microscopy through thick layers based on linear correlation. *Optics Letters* **19**, 1919–1921 (1994).

[13] Rajadhyaksha, M., Anderson, R. R. & Webb, R. H. Video-rate confocal scanning laser microscope for imaging human tissues in vivo. *Applied Optics* **38**, 2105–2115 (1999).

[14] Denk, W., Strickler, J. H. & Webb, W. W. Two-Photon Laser Scanning Fluorescence Microscopy. *Science* **248**, 73–76 (1990).

[15] So, P. T. C., Dong, C. Y., Masters, B. R. & Berland, K. M. Two-Photon Excitation Fluorescence Microscopy. *Annual Review of Biomedical Engineering* **2**, 399–429 (2000).

[16] Hell, S. W. *et al.* Three-photon excitation in fluorescence microscopy. *Journal of Biomedical Optics* **1**, 71–74 (1996).

[17] Zipfel, W. R. *et al.* Live tissue intrinsic emission microscopy using multiphoton-excited native fluorescence and second harmonic generation. *Proceedings of the National Academy of Sciences* **100**, 7075–7080 (2003).

[18] Yoo, K. M. & Alfano, R. R. Time-resolved coherent and incoherent components of forward light scattering in random media. *Optics Letters* **15**, 320–322 (1990).

[19] Papaioannou, D. G., ’t Hooft, G. W., Baselmans, J. J. M. & van Gemert, M. J. C. Image quality in time-resolved transillumination of highly scattering media. *Applied Optics* **34**, 6144–6157 (1995).

[20] Bruce, N. C. *et al.* Investigation of the temporal spread of an ultrashort light pulse on transmission through a highly scattering medium. *Applied Optics* **34**, 5823–5828 (1995).

[21] McLean, E. A., Burris, H. R. & Strand, M. P. Short-pulse range-gated optical imaging in turbid water. *Applied Optics* **34**, 4343–4351 (1995).

[22] Cai, W. *et al.* Optical tomographic image reconstruction from ultrafast time-sliced transmission measurements. *Applied Optics* **38**, 4237–4246 (1999).

[23] Fujimoto, J. G. *et al.* Femtosecond optical ranging in biological systems. *Optics Letters* **11**, 150–152 (1986).

[24] Yoo, K. M., Xing, Q. & Alfano, R. R. Imaging objects hidden in highly scattering media using femtosecond second-harmonic-generation cross-correlation time gating. *Optics Letters* **16**, 1019–1021 (1991).

[25] Bordenave, E., Abraham, E., Jonusauskas, G., Oberlé, J. & Rullière, C. Longitudinal imaging in biological tissues with a single laser shot correlation system. *Optics Express* **10**, 35–40 (2002).

[26] Duncan, M. D., Mahon, R., Tankersley, L. L. & Reintjes, J. Time-gated imaging through scattering media using stimulated Raman amplification. *Optics Letters* **16**, 1868–1870 (1991).

[27] Moon, J. A., Mahon, R., Duncan, M. D. & Reintjes, J. Three-dimensional reflective image reconstruction through a scattering medium based on time-gated Raman amplification. *Optics Letters* **19**, 1234–1236 (1994).

[28] Watson, J., Georges, P., Lépine, T., Alonzi, B. & Brun, A. Imaging in diffuse media with ultrafast degenerate optical parametric amplification. *Optics Letters* **20**, 231–233 (1995).

[29] Tolguenec, G. L., Lantz, E. & Devaux, F. Imaging through scattering media by parametric amplification of images: Study of the resolution and the signal-to-noise ratio. *Applied Optics* **36**, 8292–8297 (1997).

[30] Tolguenec, G. L., Devaux, F. & Lantz, E. Two-dimensional time-resolved direct imaging through thick biological tissues:?a new step toward noninvasive medical imaging. *Optics Letters* **24**, 1047–1049 (1999).

[31] Doulé, C., Lépine, T., Georges, P. & Brun, A. Video rate depth-resolved two-dimensional imaging through turbid media by femtosecond parametric amplification. *Optics Letters* **25**, 353–355 (2000).

[32] Duguay, M. A. & Hansen, J. W. An ultrafast light gate. *Applied Physics Letters* **15**, 192–194 (1969).

[33] Wang, L., Ho, P. P., Liang, X., Dai, H. & Alfano, R. R. Kerr–Fourier imaging of hidden objects in thick turbid media. *Optics Letters* **18**, 241–243 (1993).

[34] Wang, L., Ho, P. P., Liu, C., Zhang, G. & Alfano, R. R. Ballistic 2-D Imaging Through Scattering Walls Using an Ultrafast Optical Kerr Gate. *Science* **253**, 769–771 (1991).

[35] Wang, L. M., Ho, P. P. & Alfano, R. R. Double-stage picosecond Kerr gate for ballistic time-gated optical imaging in turbid media. *Applied Optics* **32**, 535–540 (1993).

[36] Xu, S. *et al.* Ultrafast optical Kerr gate of bismuth–plumbum oxide glass for time-gated ballistic imaging. *Journal of Modern Optics* **61**, 1452–1456 (2014).

[37] Huang, D. *et al.* Optical Coherence Tomography. *Science* **254**, 1178–1181 (1991).

[38] Drexler, W. & Fujimoto, J. G. *Optical Coherence Tomography - Technology and Applications* (Springer, 2015), second edn.

[39] Stetson, K. A. Holographic Fog Penetration. *JOSA* **57**, 1060–1061 (1967).

[40] Spears, K., Serafin, J., Abramson, N., Zhu, X. & Bjelkhagen, H. Chrono-coherent imaging for medicine. *IEEE Transactions on Biomedical Engineering* **36**, 1210–1221 (1989).

[41] Chen, H. *et al.* Two-dimensional imaging through diffusing media using 150-fs gated electronic holography techniques. *Optics Letters* **16**, 487–489 (1991).

[42] Naulleau, P., Leith, E., Chen, H., Hoover, B. & Lopez, J. Time-gated ensemble-averaged imaging through highly scattering media. *Applied Optics* **36**, 3889–3894 (1997).

[43] Arons, E. & Dilworth, D. Analysis of Fourier synthesis holography for imaging through scattering materials. *Applied Optics* **34**, 1841–1847 (1995).

[44] Cuche, E., Marquet, P. & Depeursinge, C. Simultaneous amplitude-contrast and quantitative phase-contrast microscopy by numerical reconstruction of Fresnel off-axis holograms. *Applied Optics* **38**, 6994–7001 (1999).

[45] Cuche, E., Marquet, P. & Depeursinge, C. Spatial filtering for zero-order and twin-image elimination in digital off-axis holography. *Applied Optics* **39**, 4070–4075 (2000).

[46] Gunter, P. & Huignard, J.-P. *Photorefractive Materials and Their Applications 1: Basic Effects*, vol. 1 (Springer, 2006).

[47] Hyde, S. C. W. *et al.* Depth-resolved holographic imaging through scattering media by photorefraction. *Optics Letters* **20**, 1331–1333 (1995).

[48] Hyde, S. C. W., Barry, N. P., Jones, R., Dainty, J. C. & French, P. M. W. Sub-100-Mm depth-resolved holographic imaging through scattering media in the near infrared. *Optics Letters* **20**, 2330–2332 (1995).

[49] Jones, R. *et al.* Direct-to-video holographic readout in quantum wells for three-dimensional imaging through turbid media. *Optics Letters* **23**, 103–105 (1998).

[50] Jones, R. *et al.* Direct-to-video holographic 3-D imaging using photorefractive multiple quantum well devices: Errata. *Optics Express* **2**, 552–552 (1998).

[51] Ansari, Z. *et al.* High frame-rate, 3-D photorefractive holography through turbid media with arbitrary sources, and photorefractive structured illumination. *IEEE Journal of Selected Topics in Quantum Electronics* **7**, 878–886 (2001).

[52] Tziraki, M., Jones, R., French, P. M. W., Nolte, D. D. & Melloch, M. R. Short-coherence photorefractive holography in multiple-quantum-well devices using light-emitting diodes. *Applied Physics Letters* **75**, 1363–1365 (1999).

[53] Leith, E. N. & Upatnieks, J. Holographic Imagery Through Diffusing Media. *JOSA* **56**, 523–523 (1966).

[54] Freund, I. Looking through walls and around corners. *Physica A: Statistical Mechanics and its Applications* **168**, 49–65 (1990).

[55] Vellekoop, I. M. & Mosk, A. P. Focusing coherent light through opaque strongly scattering media. *Optics Letters* **32**, 2309–2311 (2007).

[56] Katz, O., Small, E., Bromberg, Y. & Silberberg, Y. Focusing and compression of ultrashort pulses through scattering media. *Nature Photonics* **5**, 372–377 (2011).

[57] McCabe, D. J. *et al.* Spatio-temporal focusing of an ultrafast pulse through a multiply scattering medium. *Nature Communications* **2**, 447 (2011).

[58] Small, E., Katz, O., Guan, Y. & Silberberg, Y. Spectral control of broadband light through random media by wavefront shaping. *Optics Letters* **37**, 3429–3431 (2012).

[59] Park, J.-H., Park, C., Yu, H., Cho, Y.-H. & Park, Y. Active spectral filtering through turbid media. *Optics Letters* **37**, 3261–3263 (2012).

[60] Park, J.-H., Park, C., Yu, H., Cho, Y.-H. & Park, Y. Dynamic active wave plate using random nanoparticles. *Optics Express* **20**, 17010–17016 (2012).

[61] Guan, Y., Katz, O., Small, E., Zhou, J. & Silberberg, Y. Polarization control of multiply scattered light through random media by wavefront shaping. *Optics Letters* **37**, 4663–4665 (2012).

[62] Tzang, O. *et al.* Wavefront shaping in complex media with a 350 kHz modulator via a 1D-to-2D transform. *Nature Photonics* **13**, 788–793 (2019).

[63] Vellekoop, I. M. & Mosk, A. P. Phase control algorithms for focusing light through turbid media. *Optics Communications* **281**, 3071–3080 (2008).

[64] Nixon, M. *et al.* Real-time wavefront shaping through scattering media by all-optical feedback. *Nature Photonics* **7**, 919–924 (2013).

[65] He, G. S. Optical phase conjugation: Principles, techniques, and applications. *Progress in Quantum Electronics* **26**, 131–191 (2002).

[66] Yaqoob, Z., Psaltis, D., Feld, M. S. & Yang, C. Optical phase conjugation for turbidity suppression in biological samples. *Nature Photonics* **2**, 110–115 (2008).

[67] Cui, M. & Yang, C. Implementation of a digital optical phase conjugation system and its application to study the robustness of turbidity suppression by phase conjugation. *Optics Express* **18**, 3444–3455 (2010).

[68] Xu, X., Liu, H. & Wang, L. V. Time-reversed ultrasonically encoded optical focusing into scattering media. *Nature Photonics* **5**, 154–157 (2011).

[69] Wang, Y. M., Judkewitz, B., DiMarzio, C. A. & Yang, C. Deep-tissue focal fluorescence imaging with digitally time-reversed ultrasound-encoded light. *Nature Communications* **3**, 928 (2012).

[70] Si, K., Fiolka, R. & Cui, M. Fluorescence imaging beyond the ballistic regime by ultrasound-pulse-guided digital phase conjugation. *Nature Photonics* **6**, 657–661 (2012).

[71] Cui, M., McDowell, E. J. & Yang, C. An in vivo study of turbidity suppression by optical phase conjugation (TSOPC) on rabbit ear. *Optics Express* **18**, 25–30 (2010).

[72] Vellekoop, I. M., Cui, M. & Yang, C. Digital optical phase conjugation of fluorescence in turbid tissue. *Applied Physics Letters* **101**, 081108 (2012).

[73] Hsieh, C.-L., Pu, Y., Grange, R., Laporte, G. & Psaltis, D. Imaging through turbid layers by scanning the phase conjugated second harmonic radiation from a nanoparticle. *Optics Express* **18**, 20723–20731 (2010).

[74] Hillman, T. R. *et al.* Digital optical phase conjugation for delivering two-dimensional images through turbid media. *Scientific Reports* **3**, 1909 (2013).

[75] Wang, D. *et al.* Focusing through dynamic tissue with millisecond digital optical phase conjugation. *Optica* **2**, 728–735 (2015).

[76] Liu, Y., Ma, C., Shen, Y., Shi, J. & Wang, L. V. Focusing light inside dynamic scattering media with millisecond digital optical phase conjugation. *Optica* **4**, 280–288 (2017).

[77] Popoff, S. M. *et al.* Measuring the Transmission Matrix in Optics: An Approach to the Study and Control of Light Propagation in Disordered Media. *Physical Review Letters* **104**, 100601 (2010).

[78] Popoff, S., Lerosey, G., Fink, M., Boccara, A. C. & Gigan, S. Image transmission through an opaque material. *Nature Communications* **1**, 81 (2010).

[79] Choi, Y. *et al.* Overcoming the Diffraction Limit Using Multiple Light Scattering in a Highly Disordered Medium. *Physical Review Letters* **107**, 023902 (2011).

[80] Yoon, J., Lee, K., Park, J. & Park, Y. Measuring optical transmission matrices by wavefront shaping. *Optics Express* **23**, 10158–10167 (2015).

[81] de Aguiar, H. B., Gigan, S. & Brasselet, S. Enhanced nonlinear imaging through scattering media using transmission-matrix-based wave-front shaping. *Physical Review A* **94**, 043830 (2016).

[82] Freund, I., Rosenbluh, M. & Feng, S. Memory Effects in Propagation of Optical Waves through Disordered Media. *Physical Review Letters* **61**, 2328–2331 (1988).

[83] Bertolotti, J. *et al.* Non-invasive imaging through opaque scattering layers. *Nature* **491**, 232 (2012).

[84] Katz, O., Heidmann, P., Fink, M. & Gigan, S. Non-invasive single-shot imaging through scattering layers and around corners via speckle correlations. *Nature Photonics* **8**, 784–790 (2014).

[85] Li, X., Stevens, A., Greenberg, J. A. & Gehm, M. E. Single-shot memory-effect video. *Scientific Reports* **8**, 13402 (2018).

[86] Tang, D., Sahoo, S. K., Tran, V. & Dang, C. Single-shot large field of view imaging with scattering media by spatial demultiplexing. *Applied Optics* **57**, 7533–7538 (2018).

[87] Cua, M., Zhou, E. H. & Yang, C. Imaging moving targets through scattering media. *Optics Express* **25**, 3935–3945 (2017).

[88] Fienup, J. R. Phase retrieval algorithms: A comparison. *Applied Optics* **21**, 2758–2769 (1982).

[89] Fienup, J. R. Reconstruction of an object from the modulus of its Fourier transform. *Optics Letters* **3**, 27–29 (1978).

[90] Vellekoop, I. M. & Aegerter, C. M. Scattered light fluorescence microscopy: Imaging through turbid layers. *Optics Letters* **35**, 1245–1247 (2010).

[91] Ramachandran, H. & Narayanan, A. Two-dimensional imaging through turbid media using a continuous wave light source. *Optics Communications* **154**, 255–260 (1998).

[92] Emile, O., Bretenaker, F. & Floch, A. L. Rotating polarization imaging in turbid media. *Optics Letters* **21**, 1706–1708 (1996).

[93] Horinaka, H., Hashimoto, K., Wada, K., Cho, Y. & Osawa, M. Extraction of quasi-straightforward-propagating photons from diffused light transmitting through a scattering medium by polarization modulation. *Optics Letters* **20**, 1501–1503 (1995).

[94] Sudarsanam, S. *et al.* Real-time imaging through strongly scattering media: Seeing through turbid media, instantly. *Scientific Reports* **6**, 25033 (2016).

[95] Wei, X. *et al.* Real-time frequency-encoded spatiotemporal focusing through scattering media using a programmable 2D ultrafine optical frequency comb. *Science Advances* **6**, eaay1192 (2020).

[96] Wang, L. V. Ultrasound-Mediated Biophotonic Imaging: A Review of Acousto-Optical Tomography and Photo-Acoustic Tomography. *Disease Markers* **19**, 123–138 (2004).

[97] Elson, D. S., Li, R., Dunsby, C., Eckersley, R. & Tang, M.-X. Ultrasound-mediated optical tomography: A review of current methods. *Interface Focus* **1**, 632–648 (2011).

[98] Wang, L. V. Prospects of photoacoustic tomography. *Medical Physics* **35**, 5758–5767 (2008).

[99] Ruan, H., Liu, Y., Xu, J., Huang, Y. & Yang, C. Fluorescence imaging through dynamic scattering media with speckle-encoded ultrasound-modulated light correlation. *Nature Photonics* **14**, 511–516 (2020).

[100] Shih, Y. *An Introduction to Quantum Optics: Photon and Bophoton Physics* (CRC press, 2016).

[101] Erosy, O. K. *Diffraction, Fourier Optics and Imaging* (John Wiley & Sons, Inc., 2007), 1st edn.

[102] Goodman, J. W. *Fourier Optics* (W. H. Freeman and Company, 2017), fourth edn.

[103] Zangwill, A. *Modern Electrodynamics* (Cambridge University Press, 2012).

[104] Goodman, J. W. *Speckle Phenomena in Optics: Theory and Applications* (Roberts and Company Publishers, 2007).

[105] Estes, L. E., Narducci, L. M. & Tuft, R. A. Scattering of Light from a Rotating Ground Glass*. *JOSA* **61**, 1301–1306 (1971).

[106] Churnside, J. H. Speckle from a rotating diffuse object. *JOSA* **72**, 1464–1469 (1982).

[107] Di Porto, P., Crosignani, B. & Bertolotti, M. Statistical Properties of Light Scattered by Particles Suspended in a Turbulent Fluid. *Journal of Applied Physics* **40**, 5083–5087 (1969).

[108] Lehmann, P. Surface-roughness measurement based on the intensity correlation function of scattered light under speckle-pattern illumination. *Applied Optics* **38**, 1144–1152 (1999).

[109] Peng, T., Zhao, X., Shih, Y. & Scully, M. O. High Order Coherence Functions and Spectral Distributions as Given by the Scully-Lamb Quantum Theory of the Laser. *Frontiers in Physics* **9**, 185 (2021).

[110] Pestov, D. *et al.* Optimizing the Laser-Pulse Configuration for Coherent Raman Spectroscopy. *Science* **316**, 265–268 (2007).

[111] Cummins, H. Z. & Pike, E. R. *Photon Correlation and Light Beating Spectroscopy* (Springer Science+Business Media, 1974).

[112] Glauber, R. J. The Quantum Theory of Optical Coherence. *Physical Review* **130**, 2529–2539 (1963).

[113] Scully, M. & Lamb, W. E. Quantum Theory of an Optical Maser. *Physical Review Letters* **16**, 853–855 (1966).

[114] Haken, H. Theory of intensity and phase fluctuations of a homogeneously broadened laser. *Zeitschrift für Physik* **190**, 327–356 (1966).

[115] DeGiorgio, V. & Scully, M. O. Analogy between the Laser Threshold Region and a Second-Order Phase Transition. *Physical Review A* **2**, 1170–1177 (1970).

[116] Scully, M. O. & Zubairy, M. S. *Quantum Optics* (Cambridge University Press, 1997).

[117] Meschede, D., Walther, H. & Müller, G. One-Atom Maser. *Physical Review Letters* **54**, 551–554 (1985).

[118] Scully, M. O. Condensation of N Bosons and the Laser Phase Transition Analogy. *Physical Review Letters* **82**, 3927–3931 (1999).

[119] Hoang, T. F. Remarks on the charged multiplicity of hadronic Z0(91) decays. *Zeitschrift für Physik C Particles and Fields* **73**, 149–152 (1997).

[120] Scully, M. O. & Lamb, W. E. Quantum Theory of an Optical Maser. I. General Theory. *Physical Review* **159**, 208–226 (1967).

[121] Scully, M. O. & Lamb, W. E. Quantum Theory of an Optical Maser. II. Spectral Profile. *Physical Review* **166**, 246–249 (1968).

[122] Okoshi, T., Kikuchi, K. & Nakayama, A. Novel method for high resolution measurement of laser output spectrum. *Electronics Letters* **16**, 630–631 (1980).

[123] Richter, L., Mandelberg, H., Kruger, M. & McGrath, P. Linewidth determination from self-heterodyne measurements with subcoherence delay times. *IEEE Journal of Quantum Electronics* **22**, 2070–2074 (1986).

[124] Muanzuala, L., Ravi, H., Sylvan, K. & Natarajan, V. Measuring the linewidth of a stabilized diode laser. *arXiv:1510.03683 [physics]* (2015). `1510.03683`.

[125] Arecchi, F. T. Measurement of the Statistical Distribution of Gaussian and Laser Sources. *Physical Review Letters* **15**, 912–916 (1965).

[126] Corti, M., Degiorgio, V. & Arecchi, F. T. Measurements of the fine structure of laser intensity correlations near threshold. *Optics Communications* **8**, 329–332 (1973).

[127] von Storch, H. & Zwiers, F. W. *Statistical Analysis in Climate Research* (Cambridge University Press, 2003).

[128] Rudnick, P. The Detection of Weak Signals by Correlation Methods. *Journal of Applied Physics* **24**, 128–131 (1953).

[129] Mohideen Abdul Razak, M. Detection and extraction of weak signals buried in noise. *American Journal of Physics* **77**, 1061–1065 (2009).

[130] Allakhverdiyeva, N. Application of Correlation Analysis in Weak Signal Detection. *IFAC-PapersOnLine* **51**, 473–476 (2018).

[131] Fishkin, J. B., Gratton, E., vandeVen, M. J. & Mantulin, W. W. Diffusion of intensity modulated near-infrared light in turbid media. In *Time-Resolved Spectroscopy and Imaging of Tissues*, vol. 1431, 122–135 (International Society for Optics and Photonics, 1991).

[132] Tromberg, B. J., Svaasand, L. O., Tsay, T.-T., Haskell, R. C. & Berns, M. W. Optical property measurements in turbid media using frequency-domain photon migration. In *Future Trends in Biomedical Applications of Lasers*, vol. 1525, 52–58 (International Society for Optics and Photonics, 1991).

[133] Wu, T., Katz, O., Shao, X. & Gigan, S. Single-shot diffraction-limited imaging through scattering layers via bispectrum analysis. *Optics Letters* **41**, 5003–5006 (2016).

[134] Suzuki, Y. & Wang, L. V. Frequency-swept time-reversed ultrasonically encoded optical focusing. *Applied Physics Letters* **105**, 191108 (2014).

[135] Roy, A., Singh, R. K. & Brundavanam, M. M. Analysis of polarization speckle for imaging through random birefringent scatterer. *Applied Physics Letters* **109**, 201108 (2016).

[136] Edrei, E. & Scarcelli, G. Optical imaging through dynamic turbid media using the Fourier-domain shower-curtain effect. *Optica* **3**, 71–74 (2016).

[137] Foley, J. T. & Zubairy, M. S. The directionality of gaussian Schell-model beams. *Optics Communications* **26**, 297–300 (1978).

[138] Gibson, G. M. *et al.* Single-pixel imaging 12 years on: A review. *Optics Express* **28**, 28190–28208 (2020).

[139] Edgar, M. P., Gibson, G. M. & Padgett, M. J. Principles and prospects for single-pixel imaging. *Nature Photonics* **13**, 13–20 (2019).

[140] Bousi, E. & Pitris, C. Axial resolution improvement by modulated deconvolution in Fourier domain optical coherence tomography. *Journal of Biomedical Optics* **17**, 071307 (2012).

[141] Lukic, V., Markel, V. A. & Schotland, J. C. Optical tomography with structured illumination. *Optics Letters* **34**, 983–985 (2009).

[142] Baleine, E., Dogariu, A. & Agarwal, G. S. Correlated imaging with shaped spatially partially coherent light. *Optics Letters* **31**, 2124–2126 (2006).

[143] Vervandier, J. & Gioux, S. Single snapshot imaging of optical properties. *Biomedical Optics Express* **4**, 2938–2944 (2013).

[144] Cuccia, D. J., Bevilacqua, F., Durkin, A. J. & Tromberg, B. J. Modulated imaging: Quantitative analysis and tomography of turbid media in the spatial-frequency domain. *Optics Letters* **30**, 1354–1356 (2005).

[145] Arfken, G. B., Weber, H. J. & Harris, F. E. *Mathematical Methods for Physicists: A Comprehensive Guide* (Elsevier Inc., 2013), seventh edn.

[146] Swain, S. Master equation derivation of quantum regression theorem. *Journal of Physics A: Mathematical and General* **14**, 2577–2580 (1981).

[147] Mollow, B. R. Power Spectrum of Light Scattered by Two-Level Systems. *Physical Review* **188**, 1969–1975 (1969).

[148] Meystre, P. & Sargent III, M. *Elements of Quantum Optics* (Springer-Verlag Berlin Heidelberg, 2007), fourth edn.

APPENDIX A

A PROPERTY OF THE FIELD PROPAGATOR

We give a proof of Eq. (2.50) as follows:

$$\begin{aligned}
\int d\boldsymbol{\alpha} G\left(\boldsymbol{\alpha}, \beta\right) e^{i\boldsymbol{\gamma}\cdot\boldsymbol{\alpha}} &= \int d\boldsymbol{\alpha} e^{i\frac{\beta}{2}|\boldsymbol{\alpha}|^2 + i\boldsymbol{\gamma}\cdot\boldsymbol{\alpha}} \\
&= \int d\boldsymbol{\alpha} e^{i\frac{\beta}{2}\left[\left|\boldsymbol{\alpha}+\frac{\boldsymbol{\gamma}}{\beta}\right|^2 - \frac{|\boldsymbol{\gamma}|^2}{\beta^2}\right]} \\
&= e^{i\left(-\frac{1}{2\beta}\right)|\boldsymbol{\gamma}|^2} \int d\boldsymbol{\alpha} e^{i\frac{\beta}{2}\left|\boldsymbol{\alpha}+\frac{\boldsymbol{\gamma}}{\beta}\right|^2} \\
&= e^{i\left(-\frac{1}{2\beta}\right)|\boldsymbol{\gamma}|^2} \iint_{-\infty}^{\infty} d\alpha_x d\alpha_y e^{i\frac{\beta}{2}\left[(\alpha_x+\gamma_x)^2 + (\alpha_y+\gamma_y)^2\right]} \\
&= e^{i\left(-\frac{1}{2\beta}\right)|\boldsymbol{\gamma}|^2} \left(\sqrt{\frac{2\pi}{-i\beta}}\right)^2 \\
&= \frac{2\pi i}{\beta} G\left(\boldsymbol{\gamma}, -\frac{1}{\beta}\right) \qquad \text{(A.1)}
\end{aligned}$$

APPENDIX B

INTEGRAL REPRESENTATION OF BESSEL FUNCTION

The Bessel function of the first kind can be defined by an integral representation [145]

$$J_n\left(x\right) = \frac{1}{2\pi}\int_0^{2\pi} e^{i(x\sin\theta - n\theta)}d\theta = \frac{1}{\pi}\int_0^{\pi}\cos\left(x\sin\theta - n\theta\right)d\theta \tag{B.1}$$

where n is an integer. A special case of Eq. (B.1) is

$$J_0\left(x\right) = \frac{1}{2\pi}\int_0^{2\pi} e^{ix\cos\theta}d\theta = \frac{1}{\pi}\int_0^{\pi}\cos\left(x\sin\theta\right)d\theta \tag{B.2}$$

which is very useful in calculating the integral of form

$$E \sim \int_0^a \rho d\rho \int_0^{2\pi} e^{ib\rho\cos\theta}d\theta \tag{B.3}$$

where E is the amplitude of the diffracted field and (ρ, θ) defines points in the aperture. According to Eq. (B.2), we can reduce Eq. (B.3) to

$$E \sim 2\pi\int_0^a J_0\left(b\rho\right)\rho d\rho \tag{B.4}$$

Recall the recurrence relation

$$\frac{d}{dx}\left[x^n J_n\left(x\right)\right] = x^n J_{n-1}\left(x\right), \tag{B.5}$$

Eq. (B.3) is found to be

$$\begin{aligned} E &\sim 2\pi \int_0^a \frac{1}{b^2}\frac{d}{d\rho}\left[\left(b\rho\right) J_1\left(b\rho\right)\right] d\rho \\ &= \frac{2\pi}{b^2}\left[b\rho J_1\left(b\rho\right)\right]_0^a \\ &= \frac{2\pi a}{b} J_1\left(ab\right) \end{aligned} \tag{B.6}$$

where the last line is reached using the fact that $J_1\left(0\right) = 0$.

APPENDIX C

QUANTUM REGRESSION THEOREM AND THE CALCULATION OF TWO-TIME CORRELATION FUNCTION

The power spectrum of the laser can be deduced from two-time correlation function of the field operator $\left\langle \hat{E}^{(-)}(t)\,\hat{E}^{(+)}(t+\tau)\right\rangle$. In general, a solution of the laser density matrix is not adequate to calculate the correlation function [116]. However, in Markovian approximation,the quantum regression theorem allows us to calculate the two-time correlation from a single-time expectation value [121, 146, 147, 148].

To see this, we first define the time evolution operator of the atom-reservoir system:

$$\hat{U}(t) = \exp\left\{-i\hat{H}t/\hbar\right\} \tag{C.1}$$

where $\hat{H}$ is the total Hamiltonian of the system. Then, the total density operator of the system at time $t > 0$ can be given in terms of the density operator at time $t = 0$ by

$$\hat{\rho}_s(t) = \hat{U}(t)\,\hat{\rho}_s(0)\,\hat{U}^{\dagger}(t) \tag{C.2}$$

We also define the reduced density operator for the atom and the reservoir at time t as

$$\hat{\rho}_a(t) = \mathrm{Tr}_r\left\{\hat{\rho}_s(t)\right\} \tag{C.3}$$

$$\hat{\rho}_r(t) = \mathrm{Tr}_a\left\{\hat{\rho}_s(t)\right\} \tag{C.4}$$

where Tr_r and Tr_a stand for tracing over the reservoir and the atom, respectively. We further assume that the atom density operator is uncoupled from the reservoir density operator at time $t = 0$, so $\hat{\rho}_s(0)$ can be factorized as

$$\hat{\rho}_s(0) = \hat{\rho}_a(0) \otimes \hat{\rho}_r(0) \tag{C.5}$$

The expectation value of the field operator $\hat{E}^{(-)}(t)$ is given by

$$\begin{aligned}
\left\langle \hat{E}^{(-)}(t) \right\rangle &= \mathrm{Tr}_s \left\{ \hat{E}^{(-)}(0)\, \hat{\rho}_s(t) \right\} \\
&= \mathrm{Tr}_s \left\{ \hat{E}^{(-)}(0)\, \hat{U}(t)\, \hat{\rho}_s(0)\, \hat{U}^\dagger(t) \right\} \\
&= \mathrm{Tr}_a \left\{ \hat{E}^{(-)}(0)\, \hat{U}(t)\, \mathrm{Tr}_r \left\{ \hat{\rho}_a(0) \otimes \hat{\rho}_r(0) \right\} \hat{U}^\dagger(t) \right\} \\
&= \mathrm{Tr}_a \left\{ \hat{E}^{(-)}(0)\, \hat{U}(t)\, \hat{U}^\dagger(t+\tau)\, \hat{U}(t+\tau)\, \hat{\rho}_a(0)\, \hat{U}^\dagger(t+\tau)\, \hat{U}(t+\tau)\, \hat{U}^\dagger(t) \right\} \\
&= \mathrm{Tr}_a \left\{ \hat{E}^{(-)}(0)\, \hat{U}^\dagger(\tau)\, \hat{\rho}_a(t+\tau)\, \hat{U}(\tau) \right\} \qquad \text{(C.6)}
\end{aligned}$$

The two-time correlation function is given by

$$\begin{aligned}
&\left\langle \hat{E}^{(-)}(t)\, \hat{E}^{(+)}(t+\tau) \right\rangle \\
&= \mathrm{Tr}_s \left\{ \hat{E}^{(-)}(t)\, \hat{E}^{(+)}(t+\tau)\, \hat{\rho}_s(0) \right\} \\
&= \mathrm{Tr}_s \left\{ \hat{U}^\dagger(t)\, \hat{E}^{(-)}(0)\, \hat{U}(t)\, \hat{U}^\dagger(t+\tau)\, \hat{E}^{(+)}(0)\, \hat{U}(t+\tau)\, \hat{\rho}_s(0) \right\} \\
&= \mathrm{Tr}_s \left\{ \hat{E}^{(-)}(0)\, \hat{U}^\dagger(\tau)\, \hat{E}^{(+)}(0)\, \hat{U}(t+\tau)\, \hat{\rho}_s(0)\, \hat{U}^\dagger(t) \right\} \\
&= \mathrm{Tr}_s \left\{ \hat{E}^{(-)}(0)\, \hat{U}^\dagger(\tau)\, \hat{E}^{(+)}(0)\, \hat{U}(t+\tau)\, \hat{\rho}_s(0)\, \hat{U}^\dagger(t+\tau)\, \hat{U}(t+\tau)\, \hat{U}^\dagger(t) \right\} \\
&= \mathrm{Tr}_s \left\{ \hat{E}^{(-)}(0)\, \hat{U}^\dagger(\tau)\, \hat{E}^{(+)}(0)\, \hat{\rho}_s(t+\tau)\, \hat{U}(\tau) \right\} \qquad \text{(C.7)}
\end{aligned}$$

If $\hat{\rho}_a(t+\tau)$ is uncoupled from the reservoir for all times, i.e., $\hat{\rho}_s(t+\tau)$ can be factorized by

$$\hat{\rho}_s(t+\tau) = \hat{\rho}_a(t+\tau) \otimes \hat{\rho}_r(0) \qquad \text{(C.8)}$$

we obtain from Eq.

$$\begin{aligned}
\left\langle \hat{E}^{(-)}(t)\, \hat{E}^{(+)}(t+\tau) \right\rangle &= \mathrm{Tr}_s \left\{ \hat{E}^{(-)}(0)\, \hat{U}^\dagger(\tau)\, \hat{E}^{(+)}(0)\, \hat{\rho}_s(t+\tau)\, \hat{U}(\tau) \right\} \\
&= \mathrm{Tr}_a \left\{ \hat{E}^{(-)}(0)\, \hat{U}^\dagger(\tau)\, \hat{E}^{(+)}(0)\, \mathrm{Tr}_r \left\{ \hat{\rho}_a(t+\tau) \otimes \hat{\rho}_r(0) \right\} \hat{U}(\tau) \right\} \\
&= \mathrm{Tr}_a \left\{ \hat{E}^{(-)}(0)\, \hat{U}^\dagger(\tau)\, \hat{E}^{(+)}(0)\, \hat{\rho}_a(t+\tau)\, \hat{U}(\tau) \right\} \qquad \text{(C.9)}
\end{aligned}$$

Comparing Eq. (C.6) and Eq. (C.9), we see that $\hat{\rho}_a\left(t+\tau\right)$ and $\hat{E}^{(+)}\left(0\right)\hat{\rho}_a\left(t+\tau\right)$ appear to have the same time evolution under $\hat{U}\left(\tau\right)$. Therefore, replacing $\hat{\rho}_a\left(t+\tau\right)$ with $\hat{E}^{(+)}\left(0\right)\hat{\rho}_a\left(t+\tau\right)$ in Eq. (C.6), we can calculate the two-time correlation function with the knowledge of single-time expectation value. In reaching Eq. (C.9) we used a crucial assumption Eq. (C.8), which is referred as the Markovian approximation.